SHADOWS (Search for Hidden And Dark Objects With the SPS)

Alviggi, M; Bachmann, S; Baldini, W; Balla, A; Biglietti, M; Büscher, V; Calcaterra, A; Cafaro, V; Charitonidis, N; Ceccucci, A

SHADOWS

Search for Hidden And Dark Objects With the SPS

Letter of Intent

M. Alviggi[1], S. Bachmann[2], W. Baldini[3], A. Balla[4], M. Biglietti[8], V. Büscher[11], A. Calcaterra[4], V. Cafaro[5], N. Charitonidis[6], A. Ceccucci[6], V. Cicero[5], P. Ciambrone[4], H. Danielsson[6], M. Dellapietra[1], A. De Roeck[6], F. Duval[6], G. Felici[4], T. Ferber[7], L. Foggetta[4], M. Gatta[4], A. Gerbershagen[13], V. Giordano[5], S. Hansmann-Menzemer[2], P. Iengo[1], M. Iodice[8], K. Jakobs[9] M. Klute[7], K. Köneke[9], M. Koval[10], G. Lanfranchi[4], A. Laudrain[11], I. Lax[5], B. Leverington[2], P. Lichard[6], K. Massri[6], A. Montanari[5], R. Murphy[6,12], T. Napolitano[4], F. Neuhaus[11], L. J. Nevay[6] A. Paoloni[4], G. Papalino[4], U. Parzefall[9], S. Ritter[11], T. Rovelli[5,14], A. Saputi[3], B. Schmidt[6], M. Schott[11], H.C. Schultz-Coulon[2], G. Sekhniaidze[1], F. Stummer[6,12], G. Torromeo[5], N. Tosi[5], U. Uwer[2], M. van Dijk[6], A. Vannozzi[4], R. Wanke[11], C. Weiser[9], P. Wertelaers[6], T. Zickler[6]

[1] *INFN, Sezione di Napoli, Napoli, Italy*
[2] *Heidelberg University, Heidelberg, Germany*
[3] *INFN, Sezione di Ferrara, Ferrara, Italy*
[4] *INFN, Laboratori Nazionali di Frascati, Frascati (Rome), Italy,*
[5] *INFN, Sezione di Bologna, Bologna, Italy*
[6] *CERN*
[7] *Karlsruhe Institute of Technology, KIT, Germany*
[8] *INFN, Sezione di Roma III, INFN, Italy*
[9] *University of Freiburg, Freiburg, Germany*
[10] *Charles University, Prague, Czech Republic*
[11] *University of Mainz, Germany*
[12] *Royal Holloway, University of London, UK*
[13] *PARTREC and University of Groningen, Groningen, The Netherland*
[14] *University of Bologna, Bologna, Italy*

CERN-SPSC-2022-030 / SPSC-I-256
04/11/2022

Executive Summary

We propose a new proton beam-dump experiment, SHADOWS, to search for a large variety of feebly-interacting particles possibly produced in the interactions of a 400 GeV proton beam with a high-Z material dump. SHADOWS will use the 400 GeV primary proton beam extracted from the CERN SPS currently serving the NA62 experiment in the CERN North area. SHADOWS will take data off-axis concurrently to the HIKE experiment when the P42 beam line is operated in beam-dump mode to accumulate up to $5 \cdot 10^{19}$ protons on target in 4 years of operation. This document describes the main achievements with respect to the Expression of Interest and represents an intermediate step towards the Proposal.

Contents

1 Introduction

Feebly-interacting particles (FIPs) with masses below the electro-weak (EW) scale and possibly belonging to a rich dark sector represent a complementary approach with respect to the traditional Beyond the Standard Model (SM) physics explored at the LHC. They can be the answer to many open questions in modern particle physics: the baryon asymmetry of the Universe, the nature of dark matter (DM), the origin of the neutrino masses and oscillations, the cosmological inflation, the strong CP problem, and the hierarchy of scales [1].

The interest for FIPs in the broader particle and astroparticle communities is continuously growing, and a multitude of initiatives has emerged in the recent years. The profound interest in this emerging field is reported in many important reports and documents from the community at large: the Cosmic [2] and Intensity [3] Frontier Reports of the 2013 Snowmass Process, the Dark Sector community report [4], the Cosmic Vision report [5], the LHC Long-Lived Particle community white paper [6], the Physics Beyond Colliders (PBC) BSM report [7], the White Paper on new opportunities for next generation neutrino experiments [8], the Briefing Book of the European Strategy for Particle Physics [9], and the Report from the FIPs2020 workshop [10].

The recent recommendations of the European Strategy for Particle Physics (ESPP) Update [11] include the physics of feebly-interacting particles among the essential scientific activities for particle physics to be pursued in the next decade.

SHADOWS aims to be a main player in the searches for FIPs in the range of the familiar matter, from the MeV to a few GeV. It aims at exploiting the existing infrastructure and accelerator complex of the CERN North Area, namely the ECN3/TCC8 experimental complex currently hosting the NA62 experiment, and the 400 GeV proton beam line P42, slowly extracted from the SPS, running concurrently with the proposed HIKE experiment. SHADOWS with the NaNu detector aims also to perform neutrino cross-section measurements (in particular tau neutrino) in a phase space complementary to the one explored at SND and FASER experiments, currently running at the LHC.

This Letter of Intent (LoI) represents the natural evolution of the Expression of Interest [12] presented to the PS and SPS Committee (SPSC) in January 2022 and aims to be an intermediate step towards the Proposal, expected to be ready in the fall of 2023. It is meant to support the case for a high-intensity operation of the P42 proton beam line in the CERN North Area, whose decision is expected to be taken by the CERN Research Board in March 2023. To this aim, the SPSC has set up a dedicated task force (ECN3 Task Force) to assess the future use of ECN3. This task force will prepare recommendations to the Committee concerning the physics justification of a high-intensity upgrade of the beam line to ECN3 and ultimately concerning the choice of the future physics programme in ECN3. The ECN3 Task Force will analyse the projects aiming to be installed in ECN3 in a 2-phase process, as explained in the following.

1. The first phase assesses if there is a valid physics case for a significant(experiment-

independent) intensity upgrade for ECN3. This assessment will be based on the reports from the PBC Beam Delivery Task Force, input from the PBC and projects' Letters of Intent. The funding of this intensity upgrade must be part of the CERN Medium Term Plan next year, which will be discussed by the Research Board in March 2023.

2. In a second phase the SPSC will prepare recommendations for the Research Board on the proposals for experiments in ECN3 after LS3. For this step the experiments are requested to submit a proposal or equivalent information by mid-late 2023.

The main novelties of the SHADOWS LoI with respect to the SHADOWS EoI are listed here below.

- *A coincise description of the current limitations of the P42 beam line and the path towards an increase of intensity* up to 2×10^{13} pot/spill, corresponding to an increase of a factor of ~ 6 with respect to the current intensity (Section 3).

- *The description of the Magnetized Iron Block (MIB) system* necessary to sweep out beam induced muon background from the SHADOWS acceptance and its preliminary (excellent) performance (Section 3.4).

- *A description of the technological options for the SHADOWS sub-detectors* currently under scrutiny including an in-depth description of the dipole magnet of the tracking system, with its competitive power consumption (10 times less than the current NA62 warm dipole magnet) (Section 5).

- *A first implementation of a* GEANT4*-based Monte Carlo framework for SHADOWS and production of simulated data samples for signal and backgrounds* (Section 6). These samples allow us to perform:

  i) a preliminary estimate of the muon induced background (either combinatorial and due to muon inelastic interactions) in the SHADOWS acceptance based on the particle flux in the GEANT4-based detector simulation after the requirements imposed for its reduction. The simulated muon flux has been also compared against the data collected by NA62 in 2021 when the experiment was operated in beam dump mode both in terms of shape of distributions and absolute rates.

  ii) a preliminary estimate of the neutrino flux in SHADOWS acceptance that allows an evaluation of the vacuum level required in the decay vessel in order to bring this background below the threshold of one event in the whole SHADOWS lifetime;

  iii) a preliminary validation with the full Monte Carlo simulation of the signal kinematic distributions used in the toys for assessing the physics potential of the experiment.

- *An update of the physics potential of the experiment for feebly-interacting particles*, that includes now the sensitivity curves for ALPs with W and gluon couplings in addition to the sensitivity curves already shown in the EoI (Section 7).

- *An extension of SHADOWS physics reach with the inclusion of the measurement of ν_τ and $\overline{\nu}_\tau$ CC and NC interactions* by installing a neutrino detector behind the SHADOWS spectrometer (see Section 8.)

What is not contained in this document (and will be ready for the Proposal) is listed in the following.

- *The reconstruction part of the simulation.* At the moment only the information at the GEANT4 hit level is considered in analysing the MC output.

- *An in-depth analysis of the inelastic interactions* due to the neutrino flux in the SHADOWS and beam line material.

- *A final decision on the sub-detector technologies.* While the Upstream Veto and the Muon system are already defined, several options are listed for the tracker, timing detector and ECAL. We will scrutinise them in depth in the coming months, also relying on several ongoing detector R&D.

- *An evaluation of the final physics sensitivity* including reconstruction and selection efficiencies, as no reconstruction is still included in the simulation. Still the inclusion of these efficiencies will not change the sensitivity curves by more than a factor of two, based on the NA62 experience.

This Letter of Intent (LoI) is organised as follows. Section 2 describes the TCC8/ECN3 experimental complex and the position of the SHADOWS detector in the TCC8 tunnel. Section 3 presents an in-depth description of the P42/K12 beam line, the maximum intensity that can be reached while maintaining compatibility with the normal operation of the overall North Area complex, and the required upgrades of the TAXes/target system. The detector concept is outlined in Section 4 along with the physics requirements. Technological options for various sub-detectors are presented in Section 5. The Monte Carlo framework including simulated background and signal samples is detailed in Section 6. Section 7 shows the updated SHADOWS physics reach. The physics reach is also compared with other main players in the same timescale, highlighting the timeliness and competitiveness of the SHADOWS project in a worldwide context, and the synergy and complementarity with the HIKE proposal, as far as FIP physics is concerned. A preliminary idea to install a neutrino detector behind the SHADOWS detector is outlined in Section 8, as part of SHADOWS physics case. Section 9 shows the schedule towards the installation of the detector during Long-Shutdown 3 (LS3) for a timely start of data taking during Run4 and a preliminary cost estimate. Finally Section 10 draws some preliminary conclusions.

2 The ECN3/TCC8 experimental complex

2.1 Description of the area

The ECN3/TTC8 experimental hall is placed underground in the CERN North Area and currently hosts the NA62 experiment. This is shown in Figure 1.

The floor of the underground complex lies about 15-m beneath the surface level. TCC8 is split in two parts by an over-pressure double "Blue Wall" aimed to separate the air volumes of the target and detector/beam line areas during operation. It is followed by the ECN3 experimental hall.

Figure 1. View of the ECN3 hall hosting the NA62 experiment.

Figure 2 shows a layout of the target area in the TCC8 tunnel, with the Be-based T10 target and the TAX (Target Attenuator for eXperimental areas) complex 23 m downstream of the T10 target that acts either as a collimator when the beam is used in Kaon mode or as a proton beam dump when the beam is used in dump mode. A description of the part of the K12 beam line interesting for SHADOWS is reported in Section 3.

A larger view of the target area including the beginning of the NA62 experimental area is shown in Figure 3. The SHADOWS detector will be placed in *zone 1* while a possible neutrino detector (Section 8) could be placed at the beginning of *zone 2*.

Figure 4 and Figure 5 show the position of the SHADOWS detector in the TCC8 cavern just downstream of the shielded zone that contains the TAX system. The dimension of the spectrometer is driven by the dimensions of the available space and by the constraints coming from safety rules and accessibility. A detailed description of the detector is reported in Section 4.

A study of the necessary modifications to the experimental area has been carried out in collaboration with the ECN3 Task Force [13], the North Area Consolidation Project

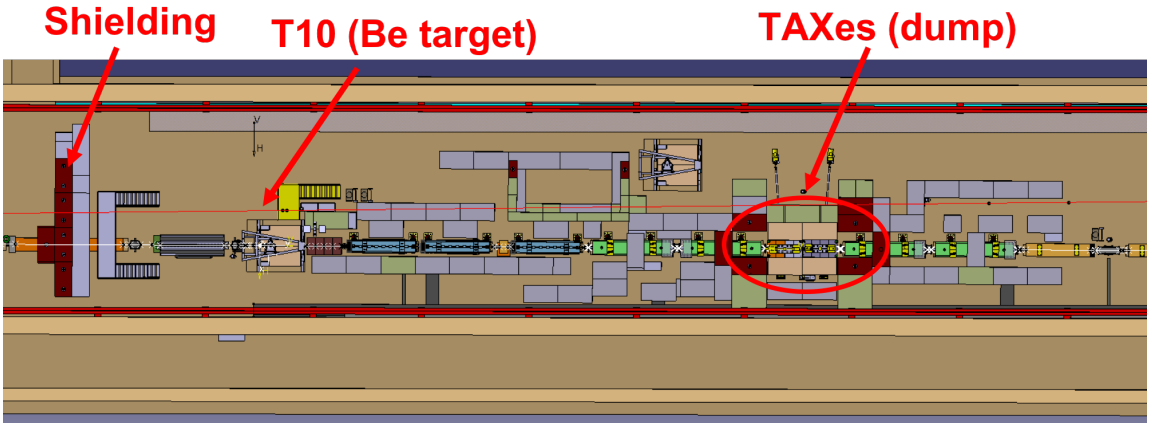

Figure 2. Schematics of the T10 Be target and TAX area in the TCC8 tunnel. The proton beam direction goes from left to right.

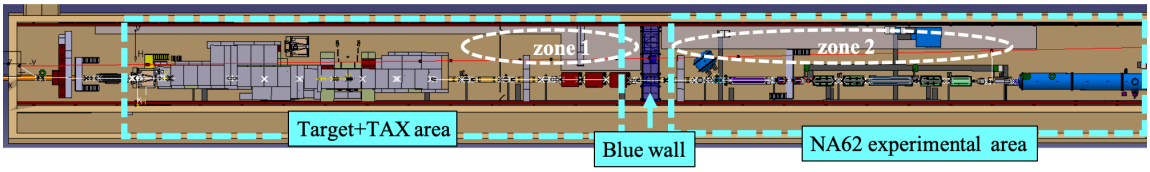

Figure 3. Schematics of the TCC8 tunnel comprising the target area and a fraction of the NA62 zone. The SHADOWS experiment can be placed in *zone 1* while a possible neutrino detector in *zone 2*. The beam runs from left to right.

(NA-CONS) [14–16] and the Conventional Beams Working Group [17]. The following, non-exhaustive list of topics has been addressed:

- beam infrastructure, including the target complex and TAX
- civil engineering aspects
- vacuum requirements
- handling and transport of detectors
- access to the experimental area
- radiation protection and safety
- cooling and ventilation
- IT infrastructure
- electrical distribution

The full set of detailed user requirements can be found in Ref. [18]. In order to ensure full compatibility with the North Area consolidation Project and as a central access point to all CERN service groups, discussion for the implementation of all requirements is steered through the NA-CONS Technical Coordination Committee (TCC) meetings, while integration aspects are handled in the Integration Committee for Experimental Areas (ICEA) as part of NA-CONS.

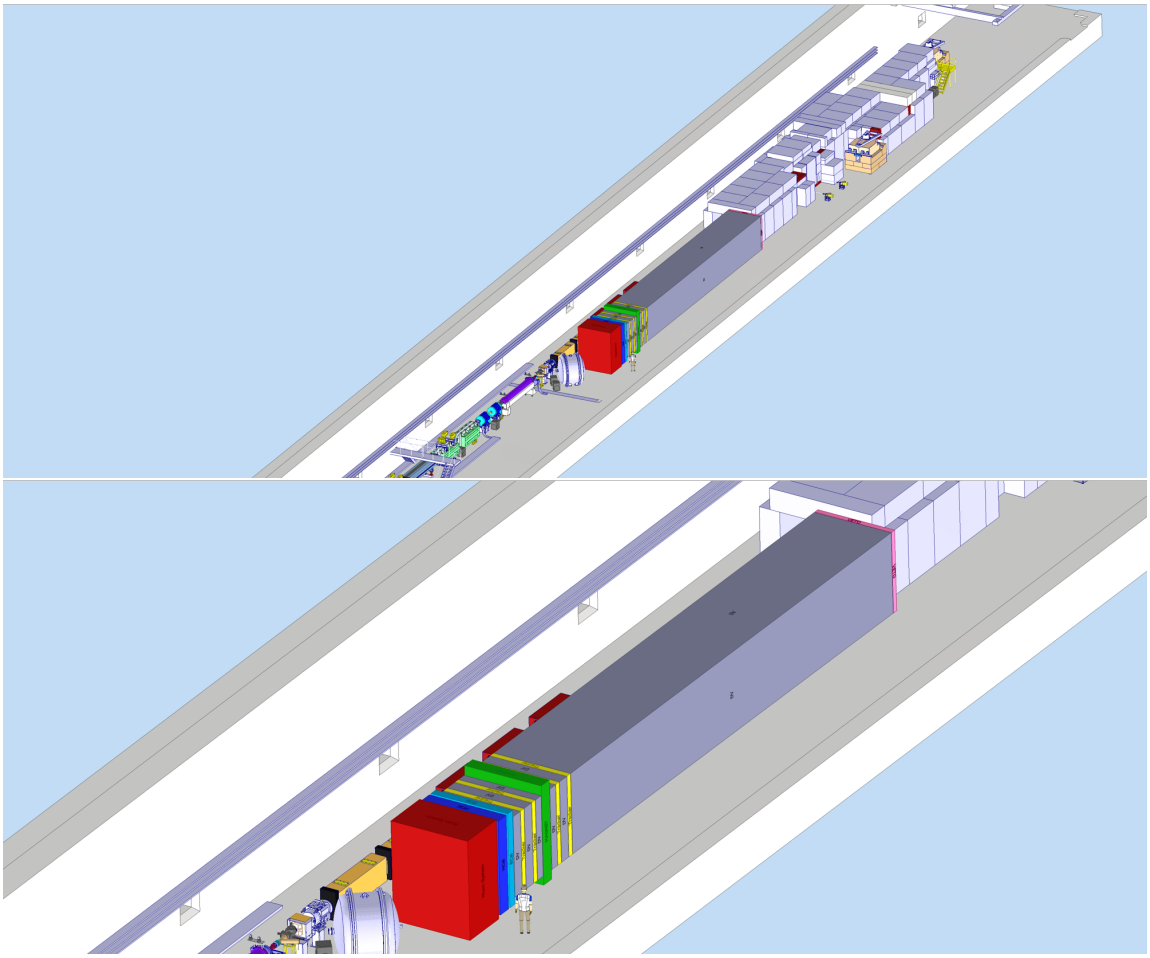

Figure 4. 3D views of the SHADOWS detector adiacent to the beam line and close to the TAX shielded zone. Top: full view in the ECN3/TCC8 cavern. Bottom: zoom in of the top plot. The dimensions of the detector and the beamline elements are to scale.

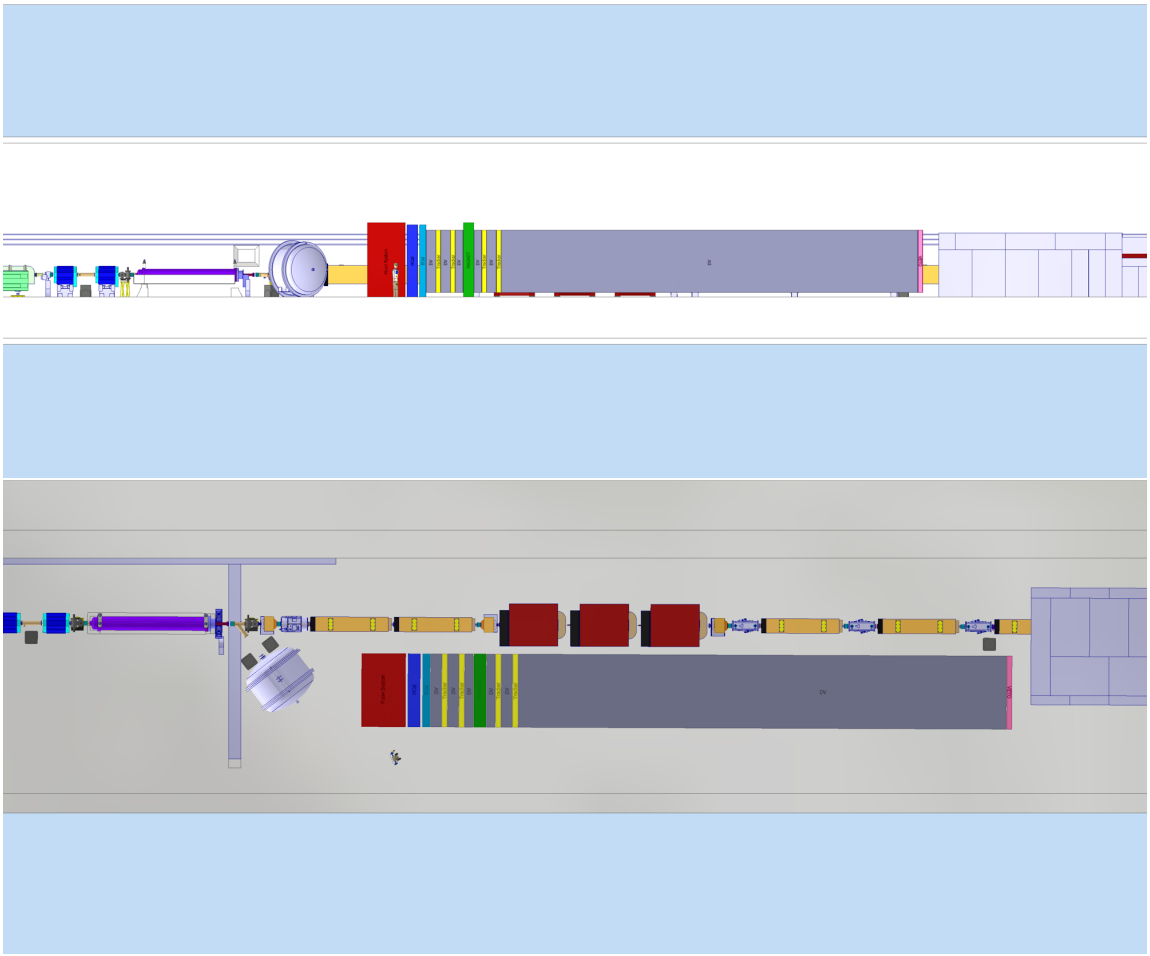

Figure 5. Lateral (top) and Top (bottom) views of the SHADOWS detector. The dimensions of the detector and the beamline elements are to scale.

3 The K12/P42 beam line

3.1 Beam line description

As a baseline scenario, SHADOWS can run in parallel with HIKE when the K12 beam runs in Beam Dump mode. The slowly-extracted primary proton beam from the SPS is transported to the T2, T4 and T6 primary targets of the North Area. Then, protons that do not interact in the T4 target are transported via the 838 metres long P42 beam to the T10 target which is located in the TCC8 cavern. Figure 6 shows the schematic layout of the extracted beam lines from the SPS in the CERN North Area complex [19].

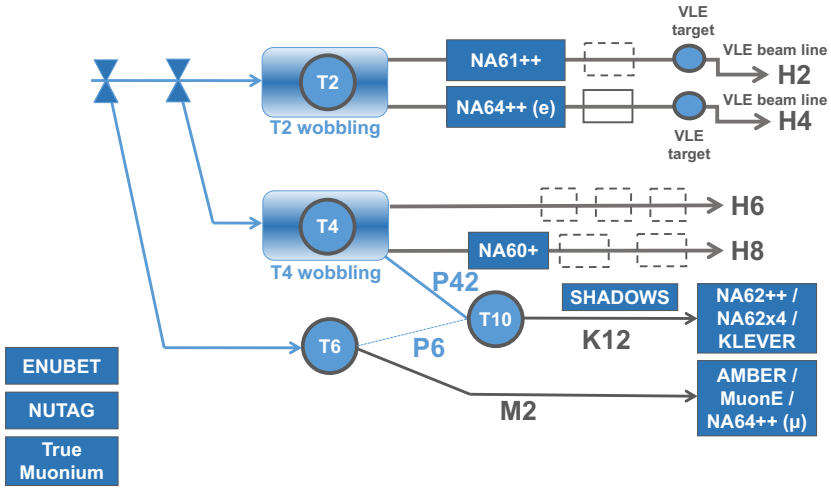

Figure 6. A schematic layout of the North Area complex. The blue arrows show the path of the protons towards the T10 target in ECN3. Figure taken from Ref. [19].

Today the P42 beam delivers $3 \cdot 10^{12}$ protons per SPS spill of 4.8 sec onto the 2 mm diameter and 40 cm long T10 beryllium target, that produces the K^+ beam for NA62. The non-interacting protons are dumped 23 m downstream in the so-called TAX dump collimator. For operation in Beam Dump mode, the primary proton beam can be focused at the TAX instead and the target put in OUT position. The TAX has 10 mm diameter holes for the beam passage in kaon mode. These will be moved further away from the location where the protons are dumped when the beam runs in Beam Dump mode. This is done by changing beam settings in software, within minutes.

The schematic layout and beam optics of the K12 beam line relevant for SHADOWS is shown in Figure 7. Only the very upstream part of the K12 beam line is relevant for SHADOWS, due to the proposed location of the detector. The T10 target is immediately followed by a 90 cm long Copper collimator (inside the target shielding) with a small aperture for the secondary beam. Hadrons outside its acceptance are stopped as quickly as possible, i.e. before they decay and produce muons that potentially can reach detectors downstream. Then follows a quadrupole triplet that would maximise the angular accep-

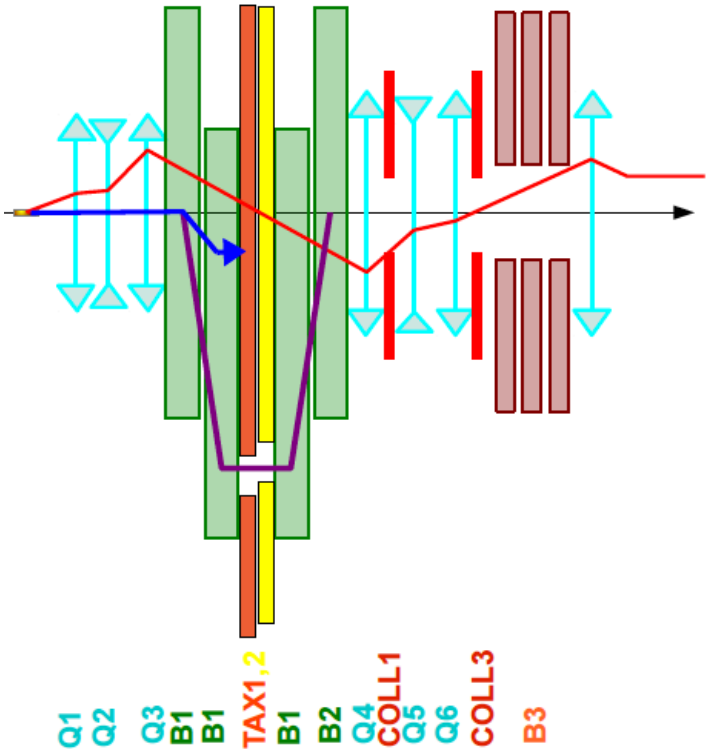

Figure 7. Schematic layout and beam optics (vertical plane) of the K12 beam line relevant for SHADOWS. The thick blue line shows the calculated proton trajectory, stopping in the TAX absorber. The purple line shows the kaon trajectory when in kaon mode and the blue arrow the proton trajectory when it operates in beam dump mode. The red line depicts the local values of the R34 beam transport matrix element, which is related to the local divergence of the beam, here given only for completeness. The abbreviation Q means quadrupole, B denominates bending MTR-type dipole magnets, and COLL stands for collimators.

tance for the secondary kaon beam and focuses the 75 GeV/c kaons at the TAX, where they would pass though typically a 12 or 14 mm diameter hole in the TAX, when not in Beam Dump mode. In Beam Dump mode, the TAX is moved into a position where all particles are dumped. In between the quadrupole triplet and the TAX, two vertical MTR-type dipole magnets produce a parallel shift of the primary protons over 20.6 mm at the TAX, where they are dumped.

In case of HIKE kaon mode operation, the beam must be brought back on the original horizontal axis by two more MTR type dipole magnets immediately following the TAX (B1 and B2). Another quadrupole triplet, interspersed with a horizontal and a vertical acceptance collimator, transports the beam towards a muon sweeper, called BEND3 (B3 in the Figure). This is a set of 3 horizontal dipole magnets, of which the gap is filled with iron with the exception of a 40 mm diameter field-free hole. It sweeps muons outside the hole horizontally, in opposite direction for opposite charges. From there on the beam has no more function for SHADOWS. The schematic view of the relevant part of the beam line shown in Figure 7 corresponds to a length of about 58 m from the T10 target centre till the exit of B3.

SHADOWS will be installed off-axis on the Jura side (i.e. towards the left when looking in beam direction) of the K12 beam line. It starts about 10 m downstream of the dump, offset by approximately 1 m towards the Jura side and has an active section of 2.5×2.5 m^2. In between the exit of the TAX and the entry of the SHADOWS detectors, an active muon sweeper and shielding (Magnetized Iron Blocks or MIBs) will be installed, as discussed in Section 3.4. For the sake of SHADOWS, the current of B2 will be optimised for muon sweeping [20].

3.2 Current intensity and known limitations

Conceptually no changes are required to the K12/P42 beam line. However, SHADOWS requests an ultimate proton intensity of $2 \cdot 10^{13}$ protons per spill (same as HIKE), which is more than 6 times higher than the nominal beam intensity for NA62. This requires a significant consolidation of the more than 40 years old beam equipment, as well as some specific upgrades. The first phase of the consolidation has already been approved and funded in the framework of the NA-CONS project [14–16]. The second phase has been documented. The present TAXs, both in the P42 and K12 beams, are not designed to withstand a beam flux of 2×10^{13} protons per spill. Their upgrade is managed via the ECN3 delivery task force[1] for P42 and by the PBC Conventional Beams Working Group (CBWG)[2] for K12. The TAX requirements and possible solutions are briefly addressed in Section 2.3. The full documentation will be provided by the respective working groups.

For the T10 target, the only requirement for SHADOWS is to preserve the possibility to have a target OUT position with a minimal amount of material on the beam. The delivery of such high intensities will also require changes all along the extraction and transfer line to the T4 target. Further options include bypassing the T4 target head with all or a fraction of the beam. These options, as well as different super-cycle compositions, are studied by the ECN3 Beam Delivery task force and will be documented in its forthcoming report. All the above beam line upgrades, as well as improvements of the magnet protection system, are also necessary for HIKE.

[1] Beam delivery ECN3 task force report, forthcoming.
[2] CBWG updated report, forthcoming.

3.3 The K12 TAX complex

The K12 TAX system consists of two motorised and water-cooled tables of 1.6 m length and 80 cm width, that each house 4 metal blocks of 40 cm length and 120 cm height. The first two blocks on the first table are made of Copper, the remaining six of cast iron. Each set of 4 blocks has two holes of 10 mm diameter and separated by 220 mm. By positioning the tables appropriately, a single effective aperture of 10 mm width and ±2.5 mm height can be created 110 mm below the straight axis from the T10 target to the experiment for the kaon mode. A beam of 2×10^{13} protons at 400 GeV/c carries a total energy of 1.28 MJ that will be deposited in the TAX over 4.8 seconds once every $\sim$ 20 seconds on average. This will lead to an unacceptable temperature rise, as reported in the Conventional Beams working group report [20]. Initial studies were performed by the SY-STI experts [4,5] which propose solutions with different block materials and with cooling circuits inside the blocks, much closer to the proton beam impact points. The same problem exists for the TAXes in the P42 beam and this is studied in the framework of the ECN3 Beam Delivery task force. The same concept will be applied to the K12 TAX system. Details like TAX hole dimensions will be worked out by the PBC Conventional Beams working group.

$CuCrZr$ is an alloy with radiation and interaction lengths similar to Copper, but with much better thermal properties. As it would be an advantage for muon background suppression to replace the iron blocks by higher-Z materials, such as CuCrZr or even denser, the use of these heavier materials would also be an advantage for HIKE. This should be studied as an option with respect to the baseline scenario.

3.4 The Magnetized Iron Block (MIB) system

The aim of the SHADOWS muon sweeping system is to reduce the muon background at the SHADOWS detector. These muons have their origin in the beam dump and are pushed off-axis into the SHADOWS acceptance by the return yokes of the two MTR type bending magnets directly downstream the dump (B1 and B2 in Figure 7), which are part of the muon sweeping system for HIKE in beam dump mode. The illumination of the muon flux immediately after the second MTR magnet (B2) is shown in Figure 8. This off-axis background has to be mitigated by a dedicated sweeping system for SHADOWS.

3.4.1 MIB conceptual design

For mitigating these backgrounds there are two options:

- **Passive mitigation:** The muons loose energy when they move through dense material. Especially lower energetic muons therefore can loose enough momentum to fall below the sensitivity of the SHADOWS detectors.
- **Active mitigation:** Magnetic fields can be used to push or pull the muons away from the detectors.

The SHADOWS muon sweeping system uses both approaches by placing dense magnetised iron blocks (MIBs) between the beam dump and the detector.

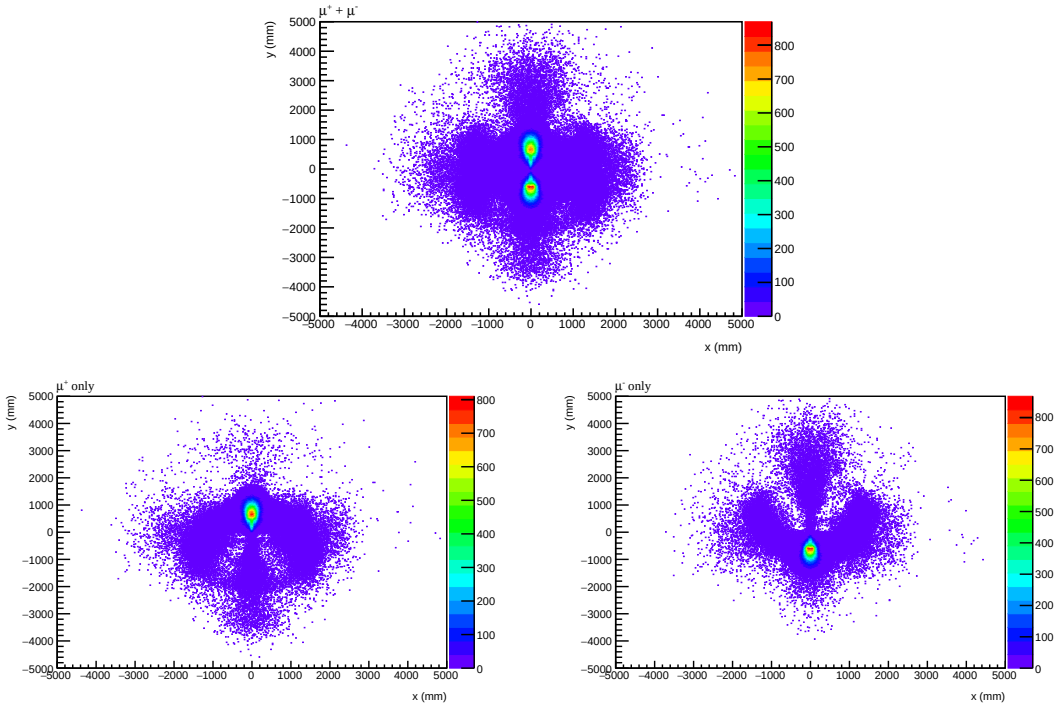

Figure 8. Top: Muon illumination at the plane corresponding to $z = 34.4$ m (after the second MTR magnet, B2). Bottom: same but divided per charge (left: positive muons, right: negative muons).

The background mitigation was found to be most efficient if done in two steps. In a first stage it is necessary to separate the positively and negatively charged muons from each other. Then in the second stage the separated muon charges can be effectively swept off-axis. Each of the two steps would be done by separate magnets, which are accordingly called Stage 1 and Stage 2 magnets in the following discussion. A schematic layout of the shape of the Stage 1 and Stage 2 magnet is shown in Figure 9 along with its 7 defining parameters that are optimised with different values for the two stages. Furthermore the magnets have found to be most effective if placed as close to the beamline as possible to assure the maximum effect of passive mitigation while sweeping the muons that enter the magnet sideways at the same time. The presently proposed, preliminary, setup of the SHADOWS MIB system is shown in Figure 10.

The muons created in the beam dump (purple) are pushed off-axis by the MTR3 and MTR4 magnets (yellow) to reduce the muon background for HIKE in beam dump mode. The 3.5 m long Stage 1 magnet (blue) is placed just downstream of MTR3, where the muons were found to be already far enough off-axis for the magnet to act on them. Its position just next to the MTR4 magnet yoke ensures that the most critical magnet components remain accessible. The impact of Stage 1 on the evolution of the muon flux is shown in Figure 11.

Stage 2 (red) is placed directly after Stage 1 to move the separated muons off-axis right

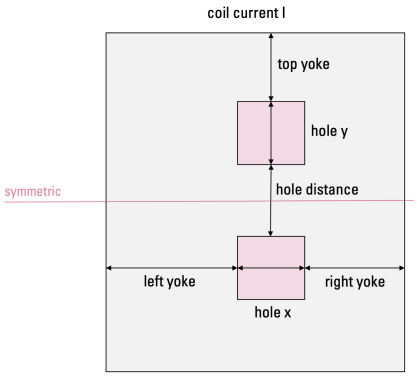

Figure 9. The concept layout ("Stage magnet") of the Stage 1 and 2 magnets and their 7 defining parameters.

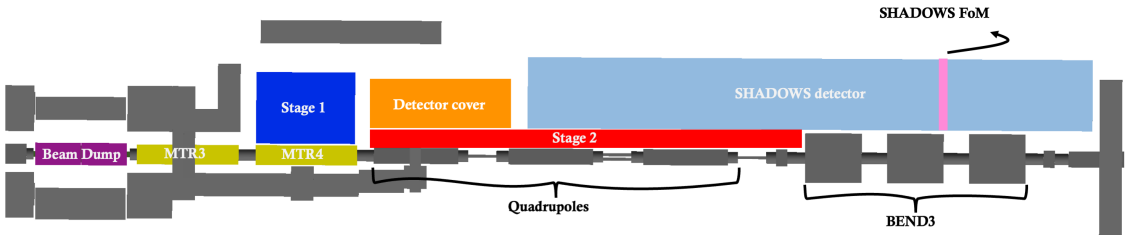

Figure 10. The optimised SHADOWS setup including the MIB system. The muons created in the beam dump (purple) are pushed off-axis by the MTR3 (B1) and MTR4 (B2) magnet (yellow) to reduce the muon background for HIKE in beam dump mode. The 3.5 m long Stage 1 magnet (blue) is placed right after MTR3, Stage 2 (red) is placed directly after Stage 1 to move the separated muons off-axis right away.

away. While Stage 1 pulls the two muon components into the direction of the MIB holes, Stage 2 pushes them away from the hole, which only works due to the separation of the charges. This means Stage 1 and 2 must have opposite polarity. Since the magnet is quite slim, it is possible to place the SHADOWS detector (skyblue), whose position is limited in x-direction by BEND3, alongside Stage 2 without moving the detector further off-axis.

In the current design Stage 2 impacts the muon background in three ways. First of all, the separated muon charges from Stage 1 are pushed further off-axis by the yoke that is further away from the beamline. Secondly, the yoke that is closer to the beamline will push back the muons that are entering from the side. Finally, Stage 2 also works as passive shielding for all muons that enter from the side. Since these muons only enter this magnet relatively late, they must have only a small angle with respect to the beamline. This means that due to its length of about 15.2 m, the passive mitigation via material interaction in iron (about 1 GeV/m of iron for muons between 1-100 GeV) will decrease the energy of these muons by up to about 15 GeV depending on the longitudinal position at which they enter the MIB. Since the majority of the muons entering sideways have relatively low momenta,

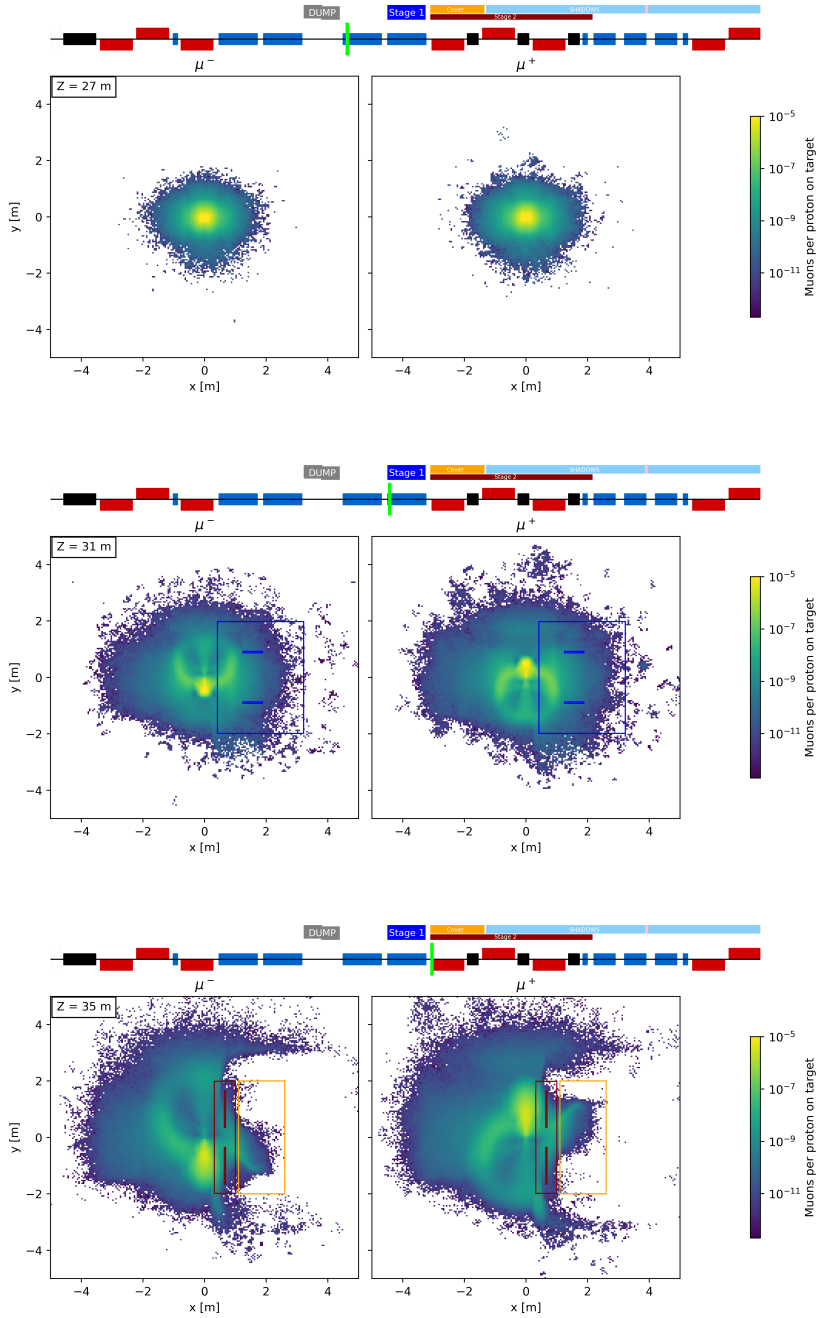

Figure 11. Evolution of the muon illumination from the dump exit to the end of the first Stage (Stage 1) of the MIB system. From top to bottom: illumination at the end of the dump; illumination before Stage1; illumination after Stage1. The scoring plane is defined by the position of the light green bar in the layout on top of each plot. See Section 6.6.1 for the detailed description of the muon flux evolution. The simulations are based on a sample of 10^{12} pot.

this is sufficient to completely eradicate the background component coming from the side.

In addition to the MIBs, a 5m long iron block is placed as shielding for the detector alongside the first few meters of the slim Stage 2 magnet, which works as additional detector cover (orange). This additional material is only a passive element in the current setup. Future optimisations foresee to magnetise the detector cover as well as a possible Stage 3. This enables to also actively sweep the remaining background that is too far off-axis to be in the acceptance of Stage 2. Indeed in chapter 6.6.1 it will be shown that most of the remaining background that enters the SHADOWS detector passes through this detector cover making it the perfect candidate for further optimisation.

The muon background that is seen in the SHADOWS Figure of Merit (short SHADOWS FoM, pink) was taken as the baseline for the optimisation of this setup. It covers the region of 1.0 m $< x <$ 3.5 m, -1.0 m $< y <$ 1.5 m, $z = 55.0$ m only taking into account muons with energies of 3 GeV and higher. The impact of Stage 2 is shown in Figure 12. Table 9 anticipates the overall background reduction factor that the current MIB design is able to achieve, that will be discussed in detail in Section 6.6.1.

Table 1. Muon flux rate in SHADOWS acceptance without and with the MIB for the two muon charges together and for each charge separately.

	$\mu^+ + \mu^-$	μ^+	μ^-
rate without MIB	100 MHz	50 MHz	50 MHz
MIB reduction factor	~ 120	~ 110	~ 150
rate with MIB	0.8 MHz	0.5 MHz	0.3 MHz

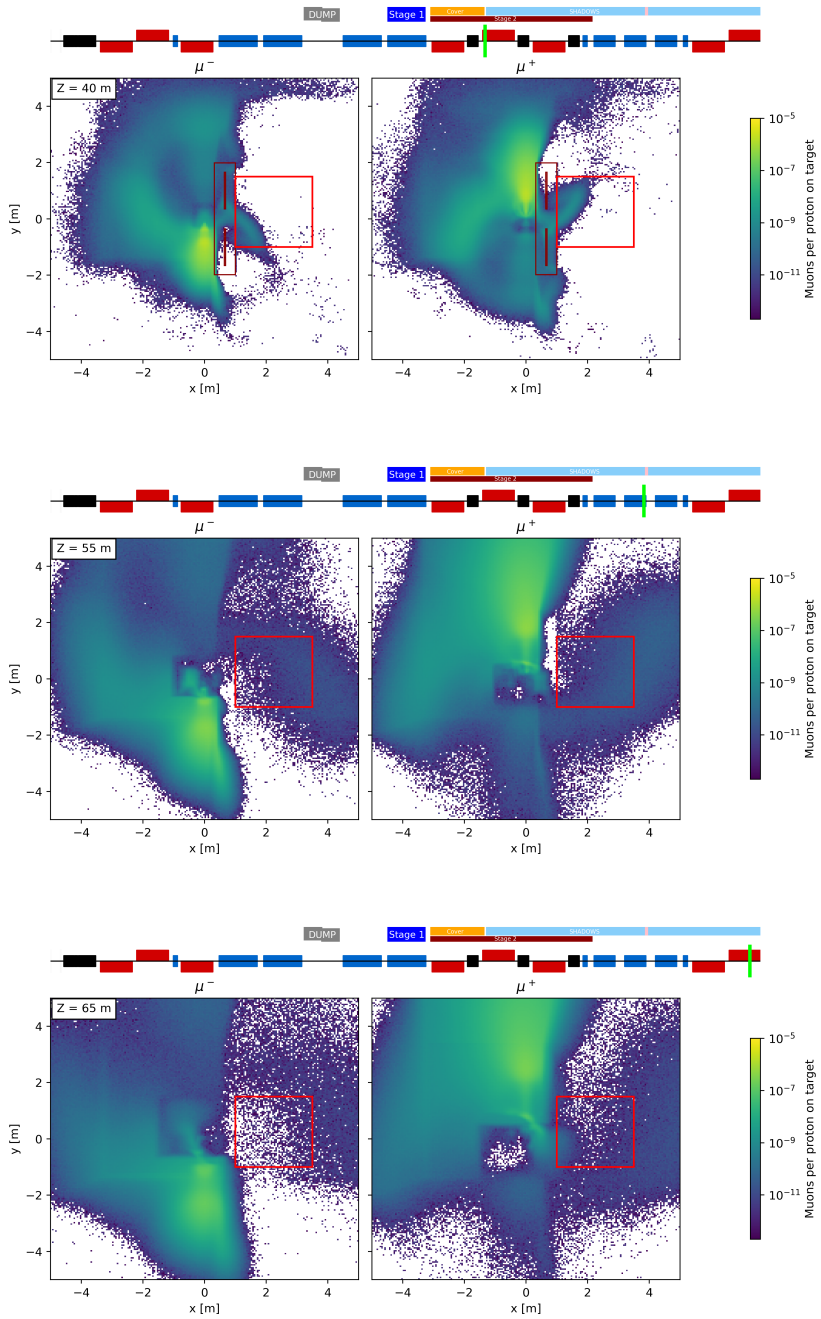

Figure 12. Evolution of the muon illumination from the beginning of the Stage2 to the position of the first muon station. From top to bottom: illumination at the end of Stage2; illumination in front of the first tracking chamber; illumination at the first muon station. The scoring plane is defined by the position of the light green bar in the layout on top of each plot. The red square box is the SHADOWS acceptance. See Section 6.6.1 for detailed description of the muon flux evolution. The simulations are based on a sample of 10^{12} pot.

As a side-note it is worth mentioning that the impact of the quadrupoles and BEND3 magnets on SHADOWS has been studied. It was found that their effect on the muon background for SHADOWS is negligible since they are relatively far downstream. For the neutrino detector downstream of SHADOWS (see Section 8) there are options to even further reduce the background. On the one hand it might be beneficial to consider adding another slim MIB (similar to Stage 2) after BEND3 to continue the sweeping and to cause more energy loss via material interaction. Alternatively, one can consider changing from horizontal to vertical sweeping in BEND3. Both options and their implications on HIKE shall be studied for the proposal.

3.4.2 MIB preliminary finite element layout

This Section describes the design of the two MIBs and the process that has been undertaken to optimize their dimensions. To understand the design choices that have been made it is useful to recall the purpose of Stage 1 and 2 again.

The Stage 1 magnet aims for an efficient vertical charge separation of the muon background. This demands a strong magnetic field in horizontal direction (x-direction) alongside the K12 beamline. Stage 2 on the other hand must provide a strong magnetic field in any direction that pushes the muons away from the SHADOWS detector behind it while simultaneously not pulling the separated muon charges back together. The centre of both magnets should be aligned at the same height as the centre of the MTR magnets - and therefore the K12 beamline - to treat both muon charges symmetrically. This directly implicates that both magnets must be symmetric in vertical direction (y-direction).

These considerations led to the idea of a certain type of MIB, which is called the "Stage Magnet" (see Figure 9). The Stage Magnet consists of an iron yoke with two holes in it, which is filled by the copper coils that are used to magnetise the iron block. It is symmetric along $y = 0$ and is a suitable candidate for both, Stage 1 and Stage 2. Apart from its length in $z-$direction, which is chosen as long as possible to maximise the passive mitigation, the Stage Magnet can be described by only 7 parameters as is indicated in Figure 9. Depending on its task it is necessary to optimise the design and therefore these very parameters for Stage 1 and Stage 2 separately.

The magnet design software FEMM [21] was used to model the Stage Magnet, which allows to calculate the magnetic field of such a MIB for any given set of parameters. The computed field can then be extracted as a fieldmap and be utilised to accurately describe the magnet within Monte Carlo frameworks like the GEANT4-based beam particle tracking software `BDSIM` [22, 23]. For the time being, the yoke material in the simulation was set to be ARMCO iron and the coils within the holes are made of copper, which should be in good agreement with whichever final materials will be chosen.

Furthermore, a python framework was created that enables the user to easily modify the 7 magnet parameters in the FEMM model to whichever constellation is desired and to directly perform the FEMM simulation with the updated design to already extract the

fieldmap. Using this framework a vast set of 20000 Stage Magnet samples was created for various different parameter constellations.

A simulation in `BDSIM` was run using BE-EA-LE's model of the K12 beamline [24, 25] to extract the incoming muon distribution at the foreseen Stage 1 location right next to MTR4. Combining this muon distribution with the knowledge that for the charge separation a strong magnetic field in x-direction is beneficial at the location where there are the most muons, made it possible to define a Figure of Merit (FoM) for what would be a suitable magnet for the task at hand. Therefore, it was possible to rank the 20000 Stage Magnet samples by this Stage 1 FoM and investigate what a "good" Stage 1 Magnet would look like.

After calculating the FoM for all of the magnet samples, the next step was to train a deep neural network (DNN) to predict the Stage 1 FoM for given MIB parameters using linear regression. It was made sure that the loss function converged and with an r^2-value of 0.99 the DNN can be assumed to make reliable predictions. The trained DNN was then used to predict the FoM for the 100 best performing sample magnets after changing their parameters slightly. If the FoM for the magnet got better, the changes were kept, otherwise discarded. This was then repeated over and over again until an equilibrium was reached and the predicted FoMs did not get any better. Now the parameter constellations of 100 optimised Stage 1 magnets were available that could be forwarded to FEMM to evaluate which of the 100 candidates really was the best performing one after calculating the FoM from the fieldmaps computed with FEMM. Thereby, the best Stage 1 candidate could be evaluated, its fieldmap extracted and Stage 1 added to the `BDSIM` model of K12 as part of the SHADOWS muon sweeping system.

Finally, an updated BDSIM simulation was run - this time with the optimised Stage 1 magnet already in place - to get the muon distribution at the exit of Stage 1. Again a FoM could be defined by combining this (now charge separated) muon distribution with the knowledge that for Stage 2 a strong field in any direction away from the SHADOWS acceptance is helpful. This enabled to rank the sample magnets with respect to the Stage 2 FoM and to optimise the MIB dimensions by training and using a second deep neural network in the same manner as described before.

Apart from the FoMs, the magnet design also took into account several limitations, which also restricted the parameter space available for the DNNs. These limitations are laid out in the following:

- The maximum current within the coils is limited to 250 A to ease the powering of the magnets.
- To avoid the need for water cooling within the coils, the current density in the holes must not exceed 1 A/mm^2. Considering the maximum current of 250 A, a limit of not more than 80 coil windings and a fill factor of only 50% to take into account a margin of safety. This means that the minimum size for each hole should not be much smaller then 0.03 m^2, which was chosen as the lower limit for the hole area.

The maximal current density then is

$$a = \frac{NI_{max}}{fA} = \frac{80 \times 250[A]}{0.5 \times 0.03[m^2]} = 0.8\left[\frac{A}{mm^2}\right] < 1.0\left[\frac{A}{mm^2}\right]$$

with winding number N, maximal coil current I_{max}, fill factor f and hole area A.

- The size of the magnet was chosen to not exceed 3 m in x-direction (width) and 4 m in y-direction (height).

By this procedure the optimised designs for Stage 1 and Stage 2 were found, their fields were calculated and both MIBs were successfully implemented in the BDSIM model to perform the simulations described in this Section and in Section 6.6.1, which evaluate the impact of the MIB system on the muon background. The optimised MIB parameters for both Stage Magnets are laid out in Table 2. Figure 13 shows these optimised magnets and what their magnetic fields look like.

It can be seen that the charge separation in Stage 1 demands a large space between the holes to pull the muons as far apart from each other as possible. Since the muon background is denser at the left side of the magnet, which in these plots is the one that would be next to the beamline, the holes are shifted to the left. The DNN found a magnet that is capable of having a magnetic field of more than 1.7 T in x-direction over the whole distance of 1.7 m between the two holes.

Stage 2 on the other hand is a slim magnet with strong fields in y-direction, which is due to the fact that there are a lot of higher energetic muons entering the magnet from the left, which are to be swept back to the other side of the K12 beamline. The hole in the centre was minimised by the DNN to avoid pulling the separated muon components back together. The right side of the yoke pushes the separated muon components further off-axis using a strong magnetic field of 1.8 T in y-direction. Therefore, the Stage 2 magnet acts like a blade that cuts through the muon background so that the affected muons miss the detector on both sides.

	Hole x	Hole y	Hole distance	Top yoke	Left yoke	Right yoke	Coil current	Length
Stage 1	0.63 m	0.05 m	1.74 m	1.06 m	0.83 m	1.34 m	250.0 A	3.5 m
Stage 2	0.04 m	1.30 m	0.71 m	0.33 m	0.32 m	0.32 m	250.0 A	15.2 m

Table 2. Preliminary optimised MIB parameters.

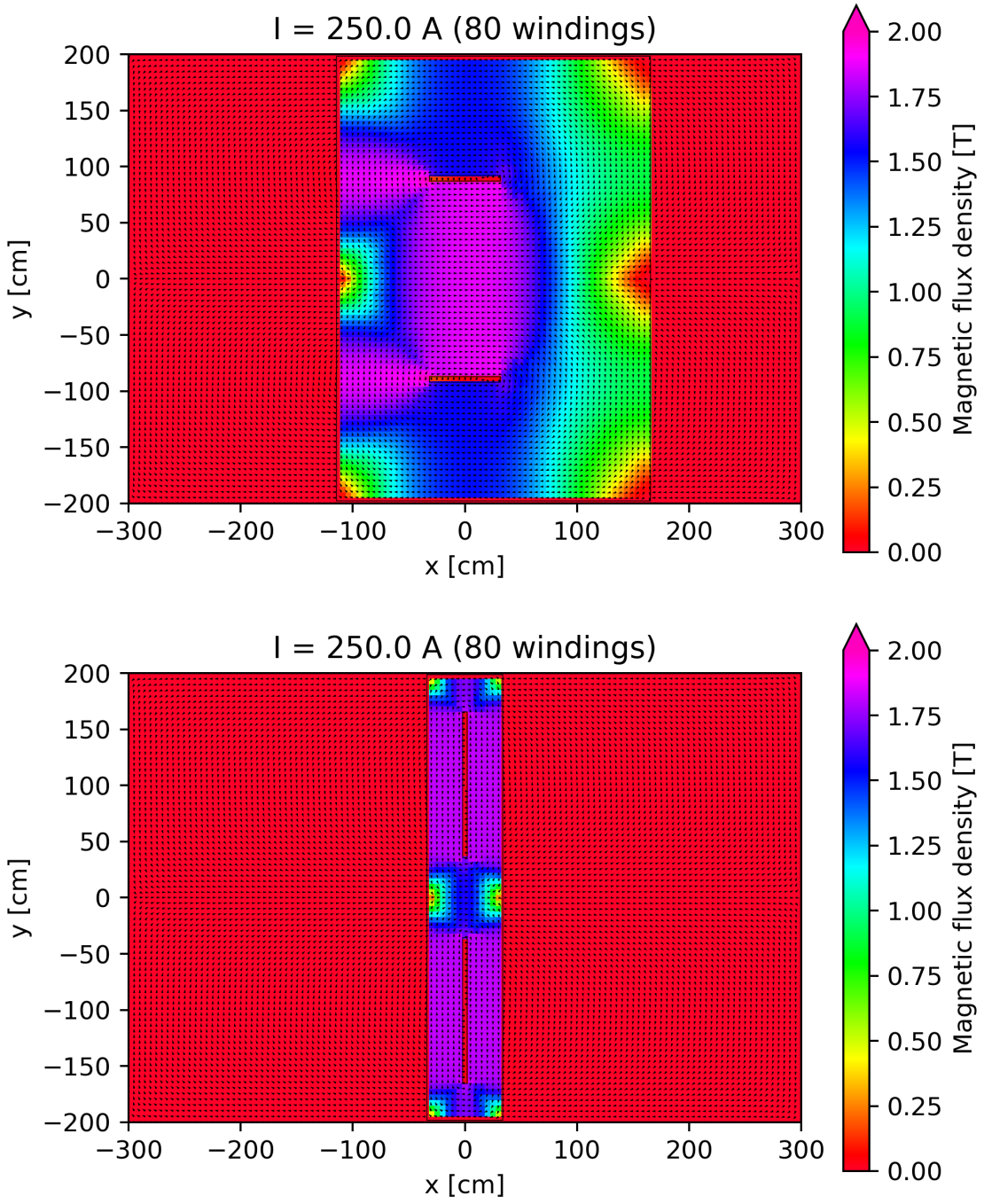

Figure 13. Preliminary design of the Stage 1 (top) and Stage 2 (bottom) magnets. Magnetic field computed using FEMM. The K12 beamline would be located at the left side of the magnets.

4 Detector Concept and Physics Requirements

4.1 Detector concept

The detector requirements are defined by the characteristics of FIPs produced in the interactions of 400 GeV/c proton beam with a dump. At these energies, FIPs with masses above the kaon mass are mostly produced in the decays of charmed and beauty hadrons and in proton bremsstrahlung and/or Primakoff effect occurring in the dump. At the SPS centre-of-mass energy ($\sqrt{s} \sim 28$ GeV) the heavy hadrons are produced with a relatively small boost and therefore FIPs emerging from their decays have a large polar angle, which is the reason of having an off-axis detector. The distance of the detector with respect to the impinging point of the proton beam onto the dump is a compromise between the maximisation of FIP flux in acceptance (that requires short distances) and the maximisation of the probability that the FIP decays before reaching the detector (that requires long distances). The optimal distance varies as a function of the FIP model and benchmark.

An off-axis detector is also much less affected by the muon and neutrino backgrounds resulting from the interactions of a proton beam with the dump. The transverse distance with respect to the beam axis is a compromise between the loss of signal acceptance and the background reduction.

The current dimensions of the detector are still those considered in the EoI with the decay volume but the detector has been shifted downstream by about 4 m to allow the current MIB system to be included between the TAX and the beginning of the decay volume. The decay volume is 20 m long with transverse dimensions of 2.5×2.5 m^2, placed $\sim$ 1.0 m off-axis with respect to the beam direction, and starting 14 m downstream of the dump. The spectrometer of about the same transverse dimensions and a length of about 12-14 m follows the decay volume. A conceptual layout of the decay volume and the spectrometer is shown in Figure 14.

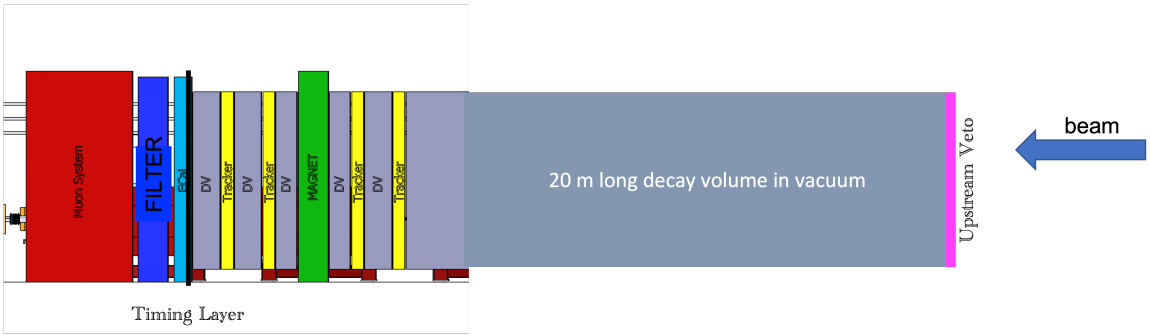

Figure 14. SHADOWS conceptual layout. The beam comes from right to left. The dimensions of the detector and the decay volume are not to scale.

4.2 Physics requirements

The SHADOWS detector must be able to reconstruct and identify most of the visible final states of FIPs decays. These are listed in Table 3 for the main portals used in the Physics Beyond Colliders exercise [7].

Table 3. Main decay modes for FIPs represented in the four portals of the PBC exercise. $\ell = e, \mu, \tau$.

Scalar portal	$\ell^+\ell^-$, $\pi^+\pi^-$, K^+K^-
Pseudo-scalar portal	$\ell^+\ell^-$, $\gamma\gamma$, $\pi^+\pi^-$, K^+K^-
Vector portal	$\ell^+\ell^-, \pi^+\pi^-, K^+K^-$
Fermion (neutrino) portal	$\ell^\pm\pi^\mp, \ell^\pm K^\mp, \ell^\pm\rho^\mp(\rho^\mp \to \pi^\pm\pi^0), \ell^+\ell^-\nu$

To this aim a standard spectrometer with excellent tracking and timing performance and some particle identification capability is required. The spectrometer should be made of:

- *an upstream veto* able to tag the residual muon flux surviving the MIB system before it enters inside the decay volume. The tagging efficiency should be 99.0 or 99.5%.

- *a tracking system* able to reconstruct with high accuracy the mass, the decay vertex and the impact parameter with respect to the impact point of the beam on the dump for FIP decays with at least two charged tracks in the final state. We require: i) a mass resolution of a few MeV for masses of the order of $\sim$ GeV; ii) a vertex resolution of $\sim$ 1 cm in the transverse plane over a volume length of $\sim$ 20 m; iii) an impact parameter resolution of $\mathcal{O}$(cm) for FIP decays into two charged tracks when the total momentum is extrapolated backward at the impact point of the beam onto the dump. All these requirements are important to separate the signal from the background.

- *a timing detector* with $\sim$ 100 ps time resolution in order to reduce any combinatorial background (and in particular the muon one) by requiring the tracks to be coincident in time. Combinatorial tracks are in fact intrinsically respectively out-of-time as they have an origin time spread over the 4.8 sec effective duration of a typical P42 proton spill;

- *an electromagnetic calorimeter* able to reconstruct the energy, the position and (possibly) the direction of photons coming from FIP decays. The directionality information is paramount for fully neutral decays, like ALP$\to \gamma\gamma$.

- *a muon detector* to positively identify muons and with timing capabilities to reinforce the rejection of the combinatorial muon background via timing measurements in combination with the timing detector.

Since the detector is off-axis the inelastic interactions of neutrinos with the air of the decay volume are a less serious concern with respect to an on-axis detector, as the

neutrinos that can enter the decay vessel are dominated by those with a large p_T. In order to reduce such a background the decay volume will be in a mild ($\sim$ 1 mbar) vacuum (see Section 6.6.4).

In the following Sections we describe our current understanding of technologies suitable for the SHADOWS sub-detectors.

5 Detector Description

5.1 Upstream Veto

The veto detector of SHADOWS is located upstream the decay vessel and has to guarantee the effective rejection of events from charged particles originated by the proton collisions on target. The vetoing of such events can be achieved off-line after the complete event reconstruction.

The vast majority of charged particles arriving to the surface of the veto detector is composed by muons of both signs, thus the detector is called Muon Veto.

At the time of the writing of this document, the design of the magnet system after the target, in charge to separate the two muon components and to sweep them outside of the detector volume (see section 3.4), is still in progress. For that reason the results of this section are based on data simulated in absence of the sweeping magnet and without any shielding layer between the detector and the beam line, and can be thus considered as a worst-case scenario. Recent studies indicated that the combined effect of the sweeping magnet and a shielding layer properly designed can reduce the muon flux by up to a factor of 120 (see Section 6.6.1).

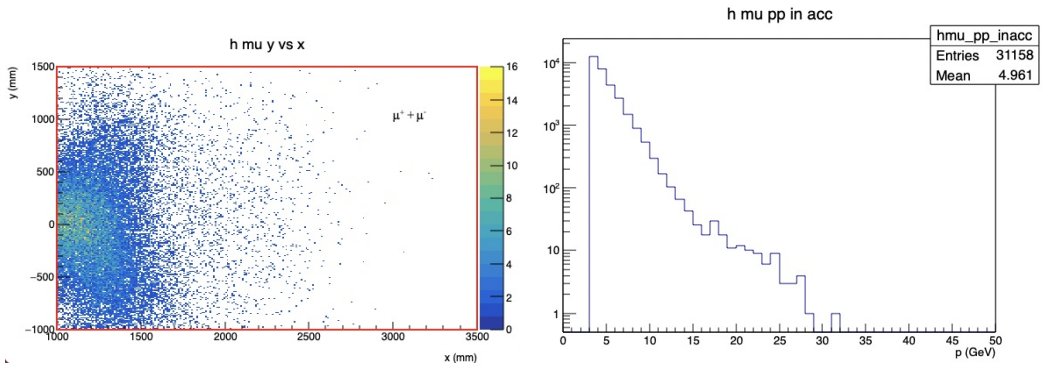

Figure 15. Hit position (left) and momentum distribution (right) of the muon tracks at the Muon Veto location.

Figure 15 shows the hit position of the muons in the $x - y$ plane at the veto location, together with the momentum distribution without including the effect of the MIB. All muons have momentum between 3 and 20 GeV, and the low-momentum component is dominant. Figure 16 shows the hit position separately for positive and negative muons.

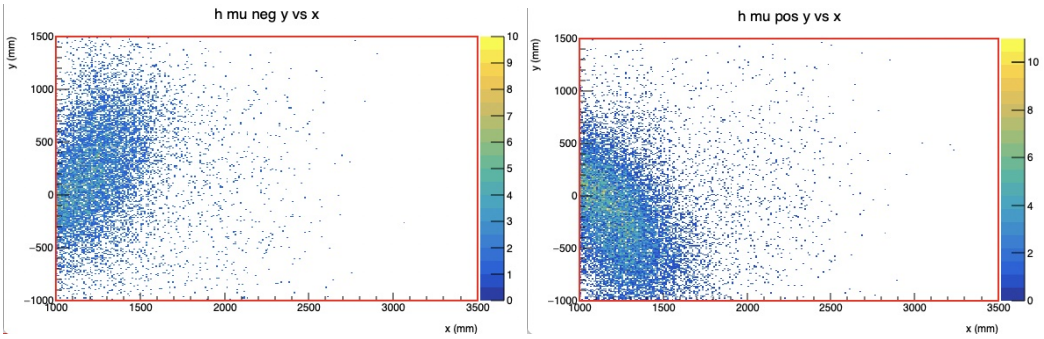

Figure 16. Hit position of the negative (left) and positive (right) muon tracks at the Muon Veto location.

5.1.1 Requirements

The main performance requirements for the Muon Veto are summarised in what follows:

- **Rate Capability.** The rate capability is estimated for the hottest region of the Veto (see fig. 15) with the results obtained from the simulated data sample increased by a Data/MC safety factor of 3. The maximum resulting expected rate of tracks with $p > 3$ GeV (the GEANT4 threshold used everywhere in the simulation is 3 GeV, as explained in Section 6) is of the order of 150 kHz/cm^2. The maximum rate will eventually reduce down to few kHz/cm^2 with the effect of the MIB magnet and the detector shielding; however to take into account the component below the 3 GeV threshold in the following the conservative value of 20 kHz/cm^2 is retained as target value. A reduction of the rate will translate in less stringent requirements on the detector.

- **Spatial resolution.** The Muon Veto must be able to assign a reconstructed cluster in both the x and y views to a track reconstructed by the SHADOWS tracking stations. The estimated uncertainty in the position reconstruction of the extrapolated track from the tracking system is in the range of 3–5 mm, depending on the muon momentum and the estimate of the multiple scattering, as reported in table4. Therefore, a resolution of about 3 mm can be considered for the Muon Veto, easily achievable with pads with about 1 cm pitch.

- **Time resolution.** The required time resolution of the Muon Veto is estimated by requiring that the probability to have a background muon in coincidence (in time and space) with the event of interest is less than 10^{-3}. For an acceptance windows of 1 cm^2 and a maximum rate of 20 kHz/cm^2 it gives a time resolution of about 20 ns, well within the reach of MPGD's.

- **Efficiency.** The efficiency of the Muon Veto must be above 99% to reduce the probability to loose an event to be vetoed below 1%.

5.1.2 Resistive Pad Micromegas

The listed requirements are met by the resistive Micromegas detector with Pad readout, a technology that allows to equip large detector surfaces with relatively low costs of construction and operation.

Resistive Micromegas have been developed for the Phase-1 upgrade of the ATLAS Muon spectrometer system [26][27], with the implementation of a resistive layer in the already well-established Micromegas technology in order to highly suppress the discharge probability. In ATLAS the detector boards, covering an active area of about 1280 m^2, have been produced in specialised PCB companies, demonstrating that the technology can be massively produced in industry. The maximum counting rate expected in ATLAS in the SHLC era is 20 kHz/cm^2.

Based on the experience for the construction of the ATLAS Micromegas, some of the authors of this LoI have[3] developed in recent years resistive Micromegas capable to efficiently and stably operate as precise tracking and triggering devices in environment with high background rates, up to 10 MHz/cm^2. This new technology exploits a different construction technique for the resistive layer with respect to the ATLAS Micromegas and a readout plane segmented in small pads of few mm^2.

The first published paper on this development is [28] and a more recent and complete review of the various prototypes designed and tested can be found here [29]. Here we focus on the description of a medium-size prototype (20×20 cm^2 active area) which layout is the base for the SHADOWS Muon Veto.

The detector is a bulk-Micromegas built at the CERN MPT workshop. The resistive protection is done with two Diamond-Like Carbon (DLC) layers deposited on insulating Kapton substrate. The two Kapton-DLC foils are glued one on top of the other on the readout plane. A pattern of conductive wires for charge evacuation interconnects the top DLC foil to the bottom one and the latter to the readout plane. The interconnection wires have a pitch of 8 mm and the two pattern (top and bottom) are staggered by half pitch. On top of the uppermost DLC layer the standard bulk-Micromegas structure is realised. The readout pads of the 20×20 PAD Micromegas have a dimension of 8×1 mm^2. The DLC surface resistivity is 30 $M\Omega/cm^2$. Figure 17 shows a schematic view of the detector construction and the layout of the readout pads.

Figure 18 shows the 20×20 Pad Micromegas under test at the GDD laboratory at CERN, together with the energy spectrum from ^{55}Fe, The measured energy resolution for 5.9 keV photon is 18%.

Figure 19 shows the gain variation as function of the counting rate induced by the photon flux. The figure of merit of the rate capability is the rate at which the gain is reduced to 90%, corresponding to more than 10 MHz/cm^2. The detector is still fully working without any gain reduction at 1 MHz/cm^2. Considering the smaller rate expected at the SHADOWS Muon Veto the detector design can be adapted accordingly, for instance by

[3] INFN RomaTre and INFN Napoli, in collaboration with the CERN MPT workshop and until 2020 with the CERN ATLAS team

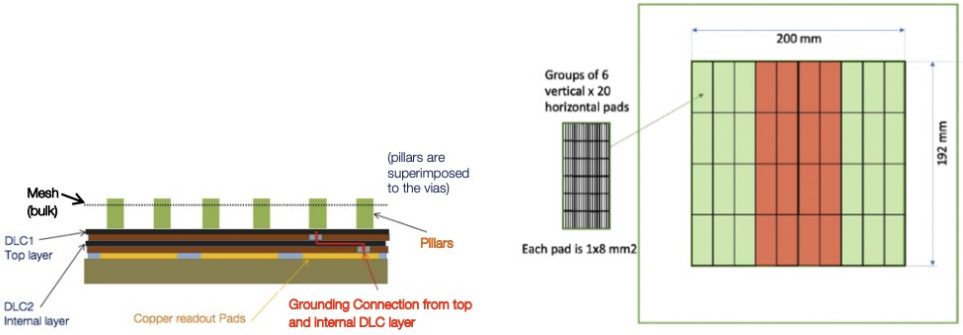

Figure 17. Schematic of the detector concept of the DLC Pad Micromegas (left) and layout of the readout pads for the 20×20 cm^2 prototype (right).

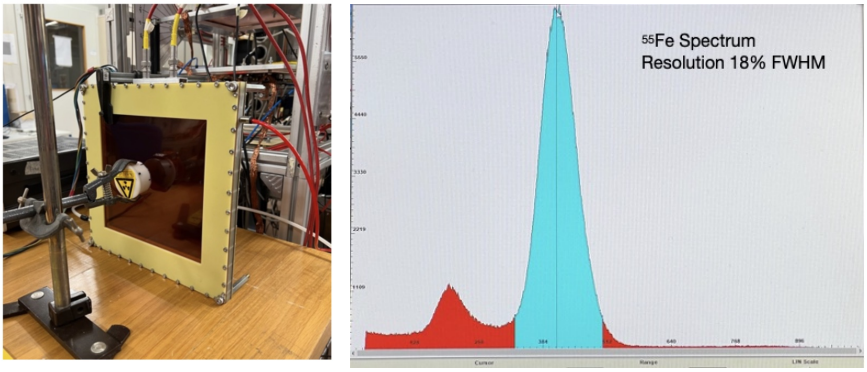

Figure 18. Picture of the 20x ×20 cm^2 prototype during laboratory test (left) and ^{55}Fe energy spectrum (right).

increasing the pitch of the evacuation wires, resulting in a simplified construction process. If the first indications of the effectiveness of the MIB magnet and the detector shielding turn out to be confirmed, a single DLC-kapton layer with charge evacuation on the sides could suffice and would further simplify the construction process.

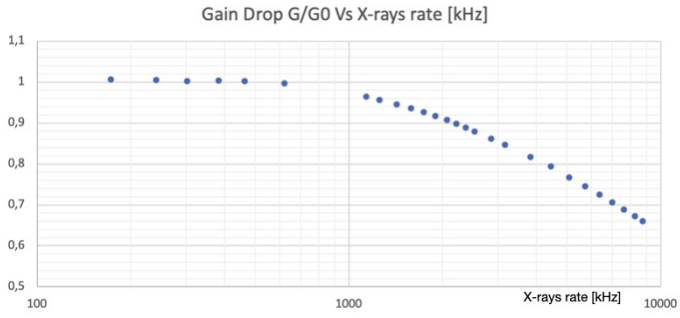

Figure 19. Relative gain as function of the irradiation rate form a Cu X-ray generator.

The detector is being tested with muon/pion beams at the CERN SPS at the time of the writing of this document, thus only few preliminary results can be included here. We will otherwise refer to results obtained with previous tests performed on smaller prototypes, with an active area of 4.8×4.8 cm^2.

Figure 20 shows the single-layer space resolution and the efficiency obtained for several PAD Micromegas detectors with a readout pad of 1 mm. The reference one for SHADOWS is the prototype named DLC20. The charge spread on the DLC allows to reach a space resolution below 100 μm. A resolution better than 3 mm is then attainable with pad size up to 10×10 mm^2, which represents the maximum size of the readout pads for the design of the SHADOWS Muon Veto. This is conformed with the first indications form the ongoing test beam of the 20×20 detector at the SPS: Figure 21 shows the online resolution obtained with 0.8 mm–wide pad. A more refined analysis should further improve it.

As shown in the Figure 20 the detector efficiency of a single plane is already matching the SHADOWS requirements. The efficiency of the DLC20 prototype has been measured to be above 98% at the working point of 500 V as amplification voltage and 300 V as drift voltage on a 5 mm drift region. Both results have been measured with an Ar:CO_2 93:7 gas mixture. Subsequent tests demonstrated that the non-flammable mixture Ar:CO_2:iC_4H_{10} in volume ratio of 93/5/2 allows to reach a gain above 10^4 at V_{amp}=480 V, while keeping the detector performance unchanged.

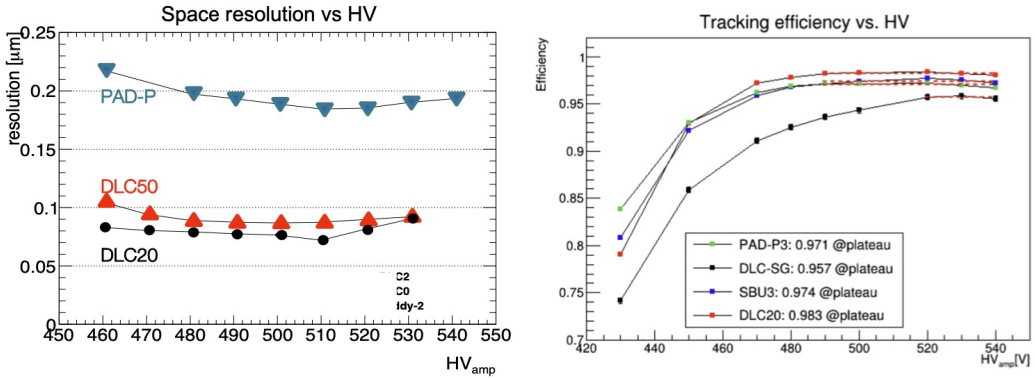

Figure 20. Space resolution (left) and efficiency turn-on curve (right) of various Micromegas Pad.

The single-layer time resolution in Ar:CO_2:iC_4H_{10} and Ar:CO_2 mixture for resistive Micromegas has been measured to be of the order of 15 ns[30], including the detector and electronics contributions and the uncertainty introduced by the analysis technique. The time resolution is expected to substantially improve with the usage of a more appropriate front-end electronics and of a faster gas mixture, in particular for the Ar:CF_4:iC_4H_{10} mixture.

5.1.3 Detector concept

The Muon Veto detector must cover a surface of about 250×250 cm^2 without dead area. For it we propose a realisation based on modular resistive Micromegas with pad readout.

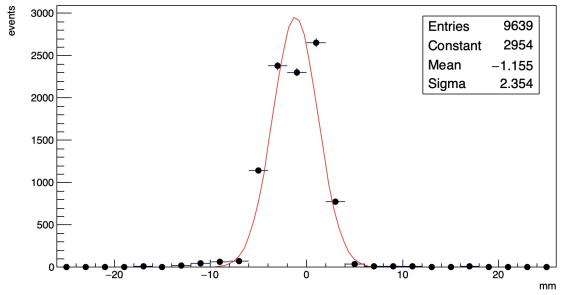

Figure 21. Preliminary on-line results of the space resolution measured for the 20×20cm^2 prototype at the CERN SPS with a Muon beam.

Each module can be built using the *bulk* technique with an active area of the order of 100×50 cm^2. The modules can be arranged side-by-side with a dead area of about 1 cm in between, or in partial overlap to remove any dead area. The number of modules needed to cover the whole surface varies between 12 and 20, depending on the dimension of the single modules and on the selected arrangement.

In both cases we propose to equip SHADOWS with two independent layers of Micromegas. This choice has a number of advantage, at the cost of doubling the total number of readout channels. The combined efficiency of two detector layers (each of them with an efficiency of 98%) is 99.96%, perfectly matching the requirement of an highly efficient detector. Moreover in 96% of the events for which a muon is detected by both layers, the double measurement of the track allows to reduce by a factor $\sqrt{2}$ both the spatial and the time resolutions. Finally, the double layer makes the detector redundant and able to cope with local problems that can develop during the operation of the system like dead electronics channels.

The readout pad segmentation should be chosen to meet the established detector requirements and it results to be essentially driven by the spatial resolution requests, which are the same for both coordinates. Such a requirements can be fulfilled by the use of 1×1 cm^{-2} square pads. Considering an active area for each of the two detector planes of 250×250 cm^2 the number of channels per layer is 62500. Hence, 125k channels for the full system.

Concerning the front-end electronics, different ASICs are under evaluation. The current tests are carried out using the APV25 chip, which could be not the optimal choice for large systems. We are planning to test other chips in use or under advanced developments in the MPGD community, such as the VMM (also used in ATLAS Micromegas and extensively used in hybrid cards in the RD51 group at CERN), the Tiger and its next upgrade (developed by the INFN Torino group and used on GEM at BESII) and the low-noise fast FATIC chip (developed by the INFN Bari group).

5.2 Tracking system and dipole magnet

The SHADOWS tracking and spectrometer system should provide on one hand the momentum measurement of the final state particles. Through the precise reconstruction of the particle tracks and their back extrapolation into the decay volume, the tracker will however also reconstruct the decay vertex of the potential FIP candidate. For the vertex reconstruction, a resolution better than 10 mm in the transverse plane and better than 50 mm in the longitudinal direction is required over the full length of the decay volume (20 m) to suppress combinatorial background. The expected hit rate per detection layer integrated over the full acceptance of a tracking station is rather moderate and less than 0.5 MHz with a maximum hit rate of 100-200 Hz/cm^2.

Preliminary studies (see below) indicate that the required tracking performance can be reached with a spectrometer design shown in Figure 22. The spectrometer is composed of 4 tracking stations, each with 2 stereo-layers x and y with a stereo-angle of 90°. The layers should cover an active area of about 2.5 × 2.5 m^2 (quadratic in x and y). The stations are grouped in pairs, with two stations positioned upstream and two stations positioned down stream of the dipole magnet. The dipole magnet provides a vertical (y-axis) field, and the field integral along z over the region of ±3 m around the dipole's symmetry axis is about 1 Tm (see Sect. 5.2.3). To minimise the effect of multiple scattering on the back-tracking, necessary to achieve the required resolution of the vertex reconstruction and on the momentum measurement, we propose that the tracking stations are placed inside the vacuum vessel of the decay volume. The vacuum vessel exit window would otherwise deteriorate the track reconstruction significantly.

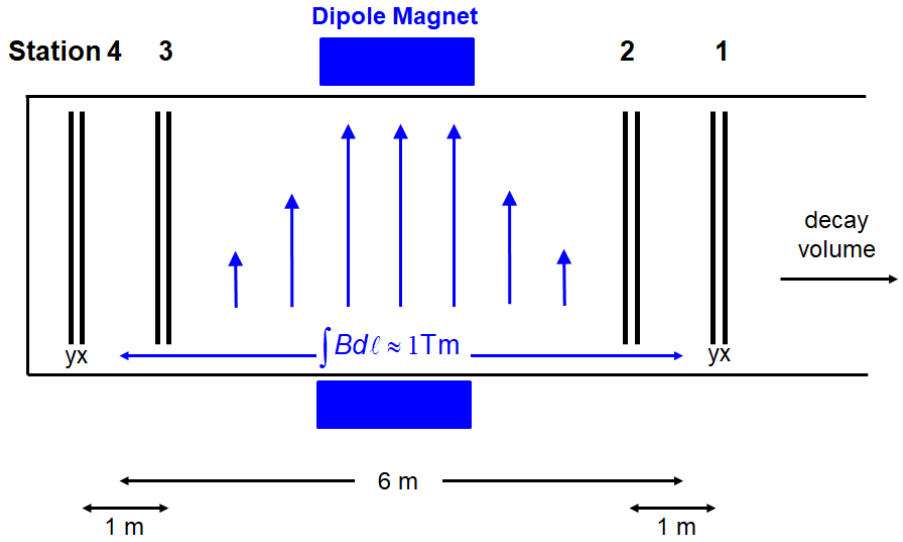

Figure 22. Layout of the tracking / spectrometer system: Four stations, each with an x and y stereo layer are placed inside a vacuum vessel around the dipole magnet. The relevant B-field integral along the $z-$axis is 1 Tm.

The very low number of hits per layer expected from backgrounds–for an assumed

sampling window $< 1\mu$s one expects less than one hit per layer–will lead to a small number of combinations when joining the hits in the x and y stereo-layers to form 2-dimensional space-points. The proposed two stereo-layers are therefore sufficient to handle the combinatorics.

For the tracking stations two different technologies are proposed:

- Straw tubes with a diameter of 1 cm as used for the NA62 tracker [31][32]: The material budget per stereo layer is with about 0.1% of a radiation length very low. The achievable relevant cluster resolution of a layer varies between 100 μm to 150 μm [32].

- Scintillating fibres of 250 μm read out by silicon photomultipliers (SiPMs) as used for the LHCb main tracker [33]: The achievable cluster resolution is better than 80 μm [34]. In contrast, the material budget per stereo-layer is significantly larger than the one of the straw option. Combining the two stereo-layers into a single mechanical object an average of 0.6% of a radiation length can be achieved.

The two technologies are complementary–medium resolution and low material budget versus high resolution and more material–and will be discussed below. Detailed simulation studies are necessary to chose between the technologies and to optimize the spectrometer design. Beside the technology choice, the optimization should address the following spectrometer parameters:

- the number of stereo views and their stereo orientation,

- the placement along the z-axis,

- the configuration (2+2 versus 3+1) of the four tracking stations,

- the question whether the decay vessel needs to be evacuated or whether it can be filled with helium at atmospheric pressure, and depending on the outcome,

- the question whether all tracking stations should be placed inside the vacuum vessel.

For this LoI we estimated the performance of the spectrometer geometry sketched in Fig. 22, assuming conservatively a spatial cluster resolution of the stereo-layers of 150 μm and a material budget of $0.6\%X_0$ per stereo-layer, parameters which can be achieved with both technologies. A simple analytical evaluation following [35] gives the momentum resolution and the angular resolution of the track the values summarised in Table 4. The table also shows the transverse and longitudinal vertex resolution which can be achieved for a distance of 5 m (15 m) from the spectrometer corresponding to a late (early) decay inside the decay volume. All numbers are given as function of the momentum.

A comparison of the two proposed technologies reveals (as expected) an advantage of the straw technology for low momentum tracks ($p \leq 20$ GeV) and an advantage for of the SciFi technology for tracks with higher momentum.

Table 4. Estimation of the spectrometer performance based on a simple analytical evaluation (see text) considering the spectrometer geometry, the hit resolution (150 μm) and multiple scattering from material (0.6%X_0 per stereo-layer). As function of the momentum, we have evaluated the momentum resolution, σ_p/p, the angular resolution σ_{θ_y} (σ_{θ_x}) of the reconstructed track in the non-bending (bending) plane, and the transverse and longitudinal vertex resolution, σ_{xy} and σ_z, respectively. The vertex resolutions σ_{xy} and σ_z have been calculated for a short (5 m) and long (15 m) back-extrapolation, corresponding to an late (early) decay in the decay vessel. To calculate σ_z we have assumed a track angle of 50 mrad w/r to the z-axis.

p [GeV]	σ_p/p	σ_{θ_y} [mrad]	σ_{θ_x} [mrad]	σ_{xy} [mm]		σ_z [mm]	
				5 m	15 m	5 m	15 m
2	0.0027	0.33	0.42	2.7	8.0	53	160
5	0.0053	0.14	0.26	1.5	4.3	29	87
10	0.01	0.07	0.22	1.2	3.5	23	70
20	0.02	0.04	0.22	1.1	3.3	22	66
50	0.05	0.03	0.21	1.1	3.2	21	64
100	0.1	0.03	0.21	1.1	3.1	21	64

5.2.1 Straws tracker option

The straw-tube tracker option proposed for the SHADOWS tracking stations is based on the design of the NA62 tracking detector [32][31]. The NA62 requirements on the tracker are very similar to SHADOWS with the exception that the higher occupancy in NA62 requires more stereo-views to solve ambiguities when combining stereo-hits to space points. The NA62 tracker consists of 4 stations, each with 4 stereo-views x, y, u and v where always the straws of two views (xy and uv) are grouped in a double-layer. The straws are operated in vacuum. As depicted in Fig. 23, each stereo-view consists of 4 layers of straws with a diameter of 9.82 mm. The four straw-layers per stereo-view ensure on one hand a high efficiency of the particle detection and on on the other hand provide a spatial resolution of the formed hit-cluster better than 150 μm [31]. The size of the stereo layers of $2.1 \times 2.1\,\mathrm{m}^2$ is close to the SHADOWS requirements. In NA62 the inner straws in each stereo-view are missing to allow the passage of the high-intensity kaon beam.

For SHADOWS, tracking stations with only two stereo-views (xy) are sufficient to handle the ambiguities of the space point assignments. Each stereo-layer with a dimension of $2.5 \times 2.5\,\mathrm{m}^2$ will comprise 570 straw-tubes of a length of 2.5 m. The total channel count of a station thus amounts to 1140. As in NA62, the straws will be operated in vacuum. We therefore will use the NA62 straw technology [31]: Each straw with a diameter of 9.82 mm is made from 36 μm thick polyethylene terephthalate (PET), coated with 50 nm of copper and 20 nm of gold on the inside to ensure electrical conductivity of the surface; The straws are fabricated by ultra-sonic welding; They with-stand a pressure of 1 bar. As anode, a gold-plated tungsten wire is used; The straws are operated with $ArCO_2$ (70:30) at atmospheric pressure.

The NA62 station design as shown in Fig. 24(left) can easily be adapted for SHAD-

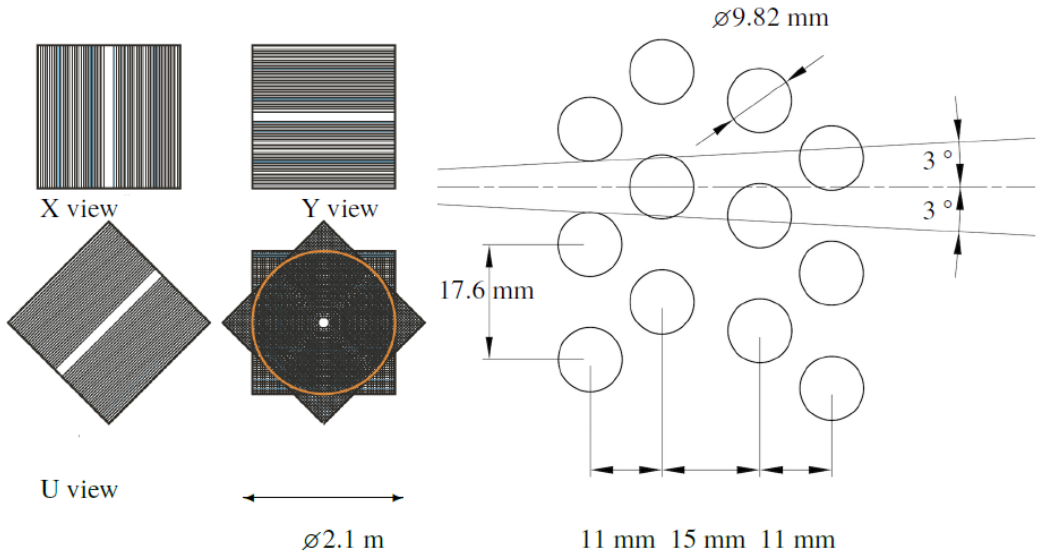

Figure 23. Stereo layer design of the NA62 straw tracker: (left) Four stereo-views (x, y, u, v) of a NA62 tracking station. The stereo-layer are about $2.1 \times 2.1\,\mathrm{m}^2$. (right) Straw arrangement within a stereo-view. Figure taken from [31].

OWS. The straws of two rectangular stereo views are mounted into a quadratic aluminum frame. The frame serves as support structure but also as vacuum enclosure. Circular shape flanges allow their integration into the vacuum vessel. Signals and the counting gas are fed through the frames. In Figure 24(left), the blue frame carries the x and y stereo view. Electronics and services are mounted on the top or on the front-side of the frame correspondingly. The second, tilted frame shown in the figure, carries the u and v-layer but would not be used for SHADOWS. Fig.24(right) shows a photograph of the straws of and x and y layer installed inside the frame. Visible is also the circular flange to connect to the vacuum vessel and to the other frame.

Correcting the material budget of NA62 by the reduced number of stereo-layer one obtains $0.23\% \cdot X_0$ for the material budget of one tracking station for SHADOWS.

5.2.2 Scintillating fibre tracker option

The Scintillation Fiber (SciFi) option proposed for the SHADOWS tracking stations is based on the technology developed for the LHCb SciFi tracker which was installed in LS2 (2019–2022) to upgrade the LHCb tracking system for the operation in LHC Run 3 and 4 [33][34]. The LHCb SciFi tracker covers an active area of 340 m^2, provides a single hit resolution better than 80 μm and a hit efficiency greater than 99%. The material budget of a single detection layer of $3 \times 5\,\mathrm{m}^2$ amounts to 1% of a radiation length X_0 [34].

The active element of the LHCb SciFi consists of 250 μm thick and and 2.5 m long scintillating fibres arranged as hexagonally close-packed six-layer mats of 13 cm width. The fibres are read out from one end by 128-channel arrays of Silicon Photo-multipliers

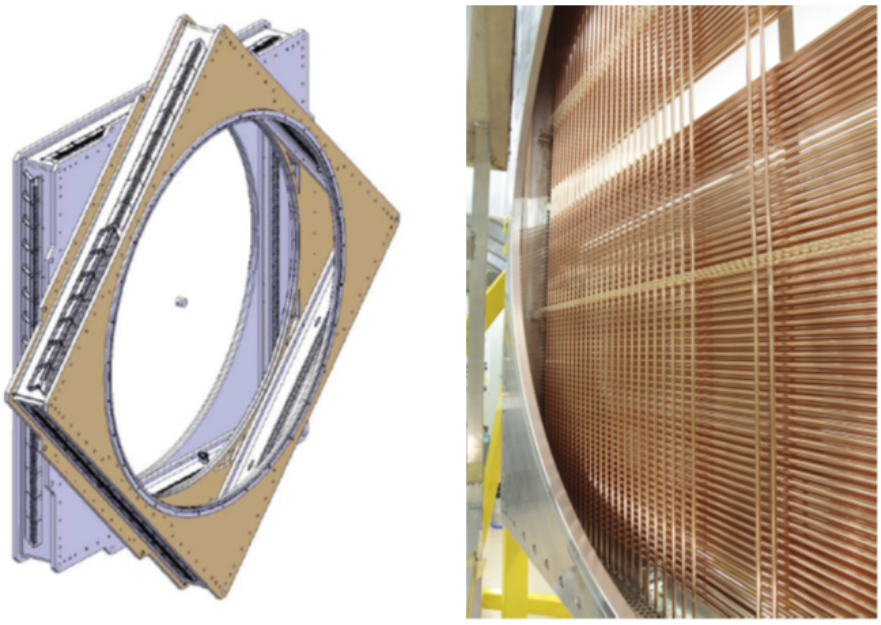

Figure 24. (left) CAD drawing of the two mounting frame for the xy-layers and the uv-layers. The individual frames are rotated by 45° with resepect to each other. Both frames have two flanges with a circular inner cut out to connect either to the vauum vessel or to each other. For the SHADOWS tracking station on the xy-layer frame is needed. (right) Photograph of mounting frame partially filled with straws. The y-layer is complete, the x-layer still misses straws on the right side. (left) Four stereo-views (x,y,u,v) of a NA62 tracking station. (right) Straw arrangement within a stereo-view. Figure taken from [32][36].

(SiPMs)[4] with a total width of about 32 mm. The other end of the fibre mats carry a mirror to increase the light yield for hits at the far end of the fibres. The fibres, blue-green emitting double-clad plastic scintillating fibres[5], have an attenuation length of about 3.5 m. A minimal ionizing particles passing the fibre mats at the far end produce about 18 photo-electrons in the SiPMs. The detection principle, a fiber mat and a SiPM is shown in Fig. 25.

In LHCb, 8 fibre mats are joined together to form 5 m long and 52 cm wide modules. To gain the necessary mechanical stability of the 5 m long modules the fibre mats are sandwiched in between two honeycomb panels and two 0.2 mm thick carbon-fibre reinforced polymer (CFRP) skins (see Fig.26).

For the SHADOWS tracking stations with a smaller height, this technology can be adapted to reduce the material budget. We propose to join the x and y stereo layers into a common $2.5 \times 2.5\,\mathrm{m}^2$ large mechanical object as shown in Fig. 27(left). Each active layer will be built from 19 fibre mats, each with a widths of 13 cm and a length of 2.5 m. The active layers will be sandwiched with 1.5 cm spacers built either from very

[4] Hamamatsu™

[5] SCSF-78MJ by Kuraray™

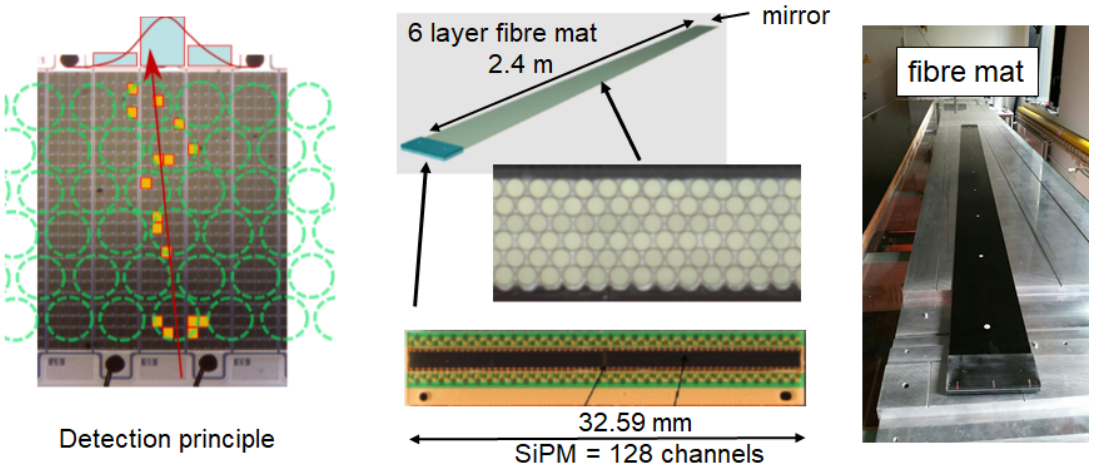

Figure 25. (left) Detection principle of the SciFi tracker: the SiPM channels are not aligned with the fibre pattern. The position is deduced from the SiPM channel position. (middle) 6-layer fibre mat with an endpiece for the mounting of four 128-channel SIPMs on the readout end and a mirror on the far end. (right) Photograph of a finished fibre mat. The fibre mat is laminated with a thin foil. At the near end the polycarbonate end-piece is visible. Also visible are white alignment pins along the centre of the mats.

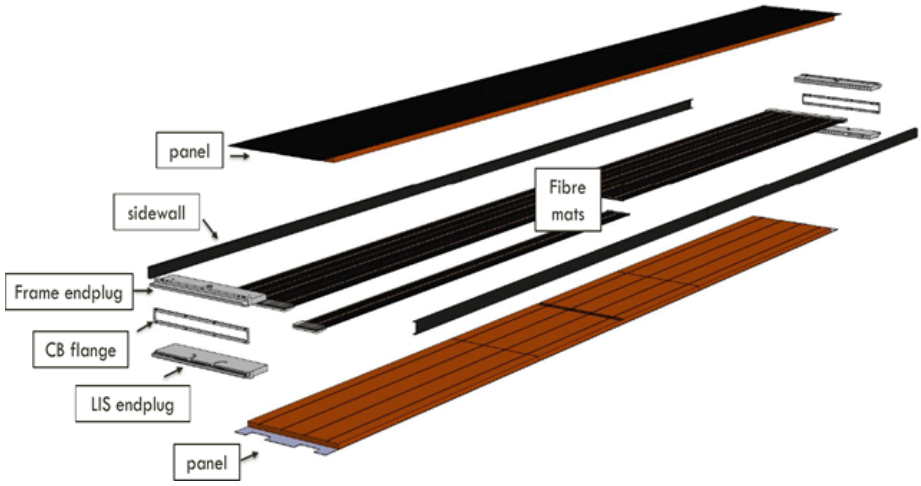

Figure 26. View of a LHCb fibre-tracker module. The module has a width of 52 cm, a total length of 5 m and comprises 8 individual fibre mats. The fibre mats are sandwiched between to honeycomb panels with a CFRP lamination at the outside. Aluminum endplugs carry a light-injection system and provide mounting points for the installation into the detector.

light honeycomb or rohacell. The material choice depends on the vacuum properties. The outside will be laminated with 0.2 mm CRRP. The sandwich layout of the module is shown in Fig. 27(right).

The $2.5 \times 2.5\,\mathrm{m}^2$ large double layer module will be installed inside a support frame

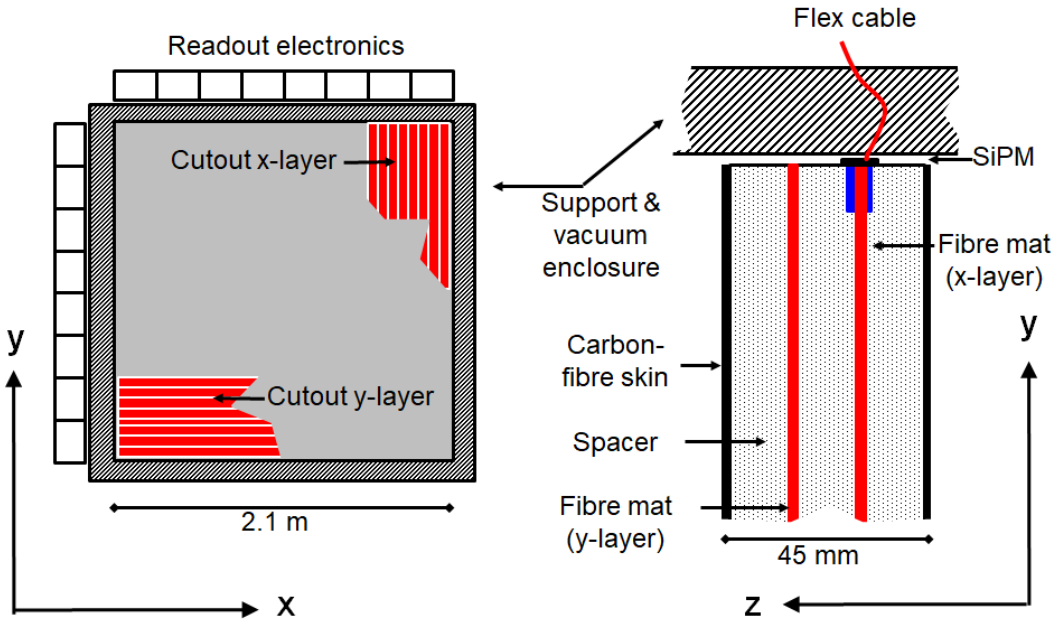

Figure 27. (left) Proposed station design of a fibre tracker station with x and y-layers. The readout of the x-layers are to the top, the one for the y-layer to the side. The support frame carrying the two-layer module also acts as vacuum enclosure. A flange similar to the one in Fig. 24 should be foreseen to connect the layer to the vacuum vessel. (right) Composition of station: two fibre layers are sandwiched with a light weight spacer material (e.g. honeycomb material) and the outside is laminated with CFRP. The flex-cable carrying the SiPM for the fibre readout feeds the signal and bias voltage through the vacuum enclosure frame.

which will also serve as vacuum enclosure to the outside. Similar to the LHCb tracker, the SiPM will be mounted on 20 cm long flex-cables which will pass the vacuum enclosure. The electronics readout is mounted on the outside of the vacuum enclosure. The proposed design comprises 9700 SiPM channels per layer (19400 per station).

The expected irradiation damage of the fibres and thus the change of the attenuation length of the fibre with time is negligible for SHADOWS, and thus the light yield will stay constant over the lifetime of the experiment. We therefore propose fibre mats with only four layers of fibres to reduce the material budget further. For the 2-layer module of a station, Table 5 lists the material budget in the detector acceptance assuming the same materials as have been used for the LHCb SciFi [34]. For the full station a value of $1.17\% \cdot X_0$ is obtained.

5.2.3 Dipole magnet

The dipole magnet of the spectrometer tracker should satisfy the following constraints:

1. provide a field integral of about 1 Tm oriented in the vertical direction.

Table 5. Estimated material budget in faction of a radiation length X_0 for the proposed station layout. The numbers are taken from the LHCb SciFi tracker [34] and are scaled where necessary.

Material	thickness (mm)	material X_0 (mm)	fraction of X_0 (%)
Fibre mats	2×0.95	332	0.57
Spacer (NOMEX)	4×15	13000	0.35
CFRP Skin	2×0.2	276	0.14
Glue	4×0.1	361	0.11
Total Station			1.17

2. reduce the power consumption to a minimum (< 0.5 MW) to cope with the increasing electricity cost.

3. have a rectangular aperture of 2.5×2.5 m^2 to cope with the spectrometer acceptance.

4. keep the yoke size at minimum. Vertically, because of the need to make excavations in the TCC8 concrete floor (the NA62 beam height being marginal at only about 1.26 m from the floor). Horizontally, because of the need to lean tight to the K12 beam line.

The shape of the dipole magnet could be very similar to the NA62 MNP33 dipole magnet (Figure 28).

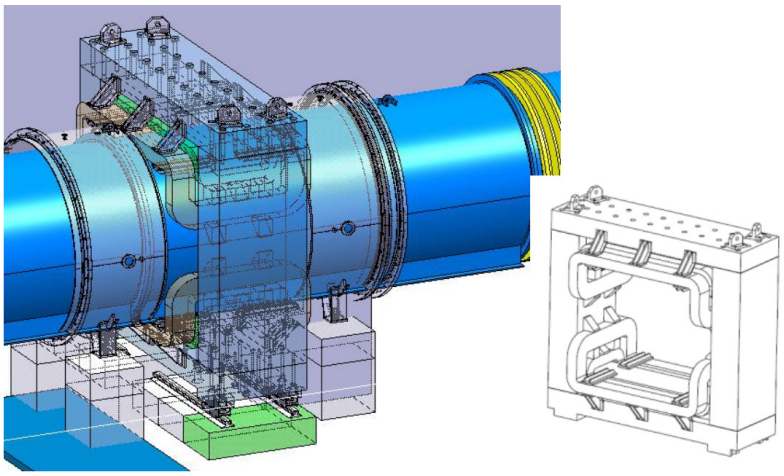

Figure 28. An example of a rectangular-aperture spectrometer magnet : MNP33 for NA48/NA62.

We are currently investigating a normal-conducting *warm* design. The classic arguments for not pursuing a superconducting alternative, namely investment cost and complexity, are only part of the reason. Apart from the vacuum tank and assembly problems, at least two more serious threats would be present for a superconductive magnet. Firstly,

the rather small bending radii in their corners, would raise issues with the safe field-current-temperature envelope of a superconductor. Furthermore and possibly more seriously, there are the Lorentz forces on the coil. A rectangular spectrometer magnet would lead to serious problems with a fully spatial Lorentz force distribution. No superconducting version of such configuration is known today in high-energy physics. Still some study will be done for the Proposal before discarding completely the superconducting option.

In the case of a warm magnet, the dissipated power can be reduced by increasing the dissipating pack volume (as the Joule heat decreases quadratically with the dimensions) and using copper instead of aluminum.

A sketch of the first volume octant is shown in Figure 29. The dimensions of the yoke for each octant (as indicated in Figure 30) are:

$$\begin{aligned} &\text{inner dimensions: } X_{y,i} = 1.6 \text{ m}, Y_{y,i} = 1.35 \text{ m} \\ &\text{outer dimensions: } X_{y,o} = 2.3 \text{ m}, Y_{y,o} = 1.93 \text{ m}, Z_y = 1.3 \text{ m} \end{aligned}$$

The iron yoke has a total mass (8 octants) of 187 tonnes. This configuration has a power consumption of $\sim$ 0.3 MW, which is about 10 times less than the current power consumption of the NA62 dipole magnet.

The vacuum tank, assumed to be a sandwich of about 100 mm thickness will be ankored to the dipole, as shown in Figure 29. Figure 31 shows a cross-sectional dimensions in mm of the chosen (copper) conductor and how several conductor can be packed together.

Figure 32 shows the y component of the magnetic field as a function of the $z$axis while Figures 33 and 34 show the maps of the field integral or bending power. Because of the assumed symmetry, our definition of the field integral $FI_{x,y}$ is :

$$FI_{x,y}(x,y) = 2\int_0^{Z_{int}} B_{x,y}(x,y,z)dz$$

where the integration is done over a line segment of limited extension, at constant x and y. We see that in the short span ($\pm$1.9 m) we reach a bending power of about 0.7 Tm while in the long span ($\pm$2.7 m) about 0.81 Tm. The component of main interest (B_y) is quite uniform over the entire range, while the component in the orthogonal direction (B_x) is almost zero, as it should be.

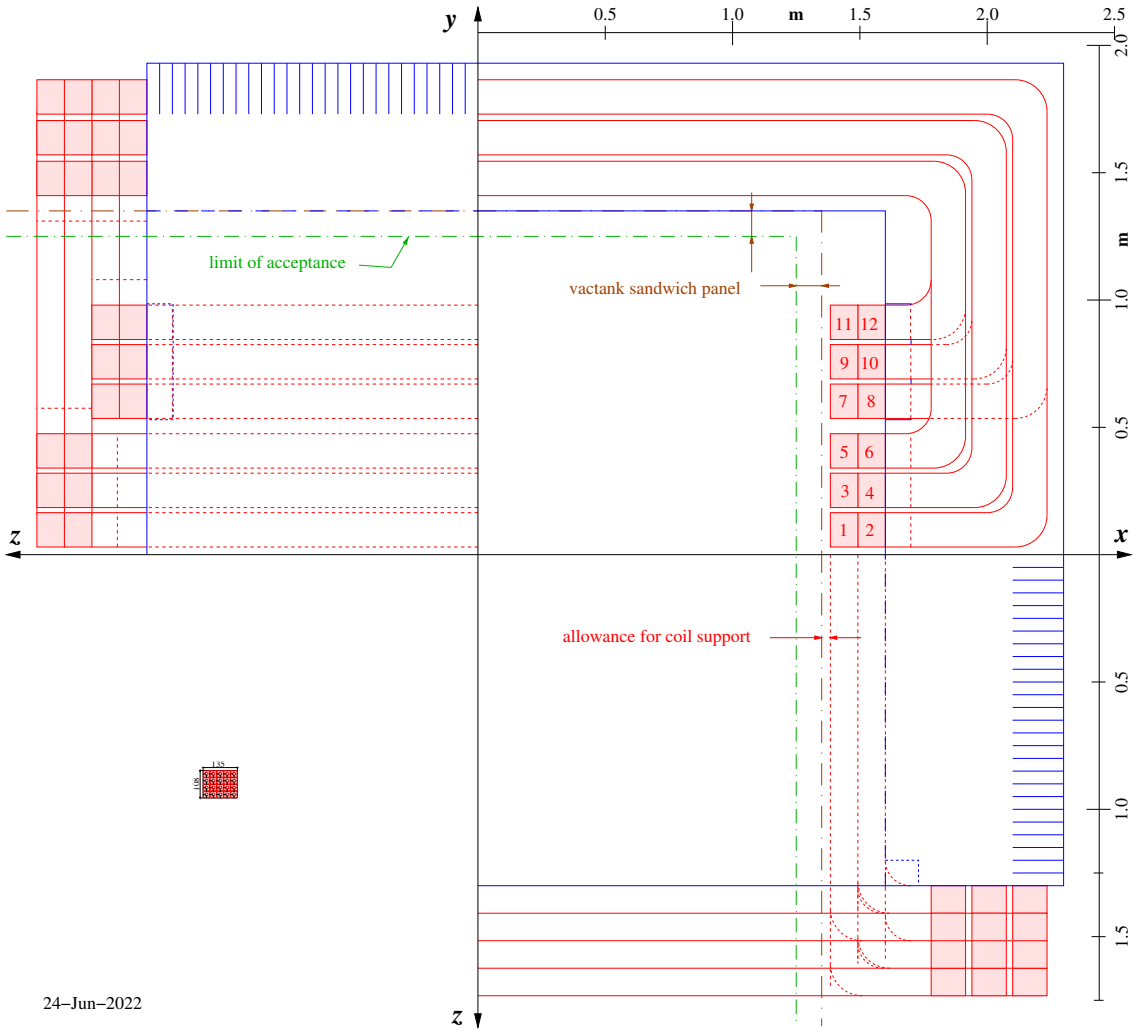

Figure 29. Preliminary layout of the dipole magnet. The engineering standard is to divide the dipole magnet volume in eight parts (so called "octants"), symmetric in x and y, four for the front and four for rear side, being "front" and "rear" defined with respect to the centre in z fixed at half width. The only point common to the eight octants is the point $(x, y, z) = (0, 0, 0)$. The first $(+x + y + z)$ volume octant, in 3 projections, is shown in the plot above.

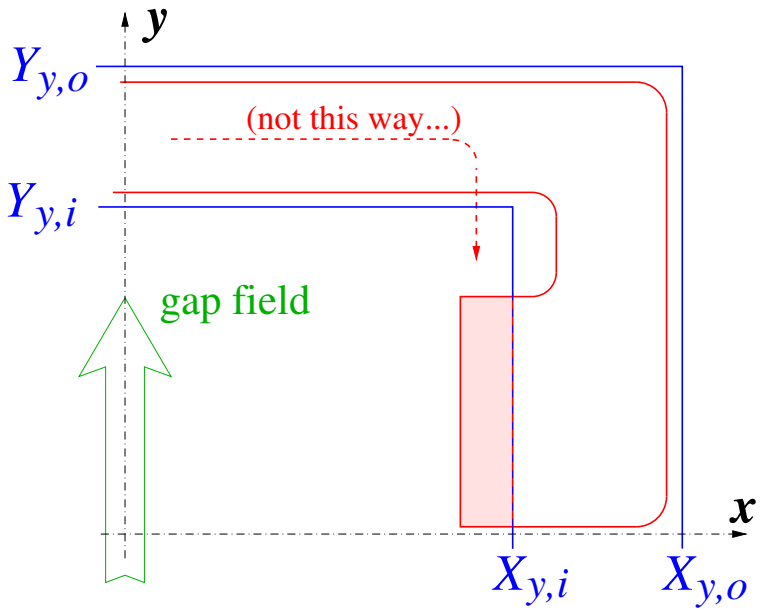

Figure 30. Sketch of the rear view onto top-right (area) quarter. Yoke in blue. Coil mass in red/pink.

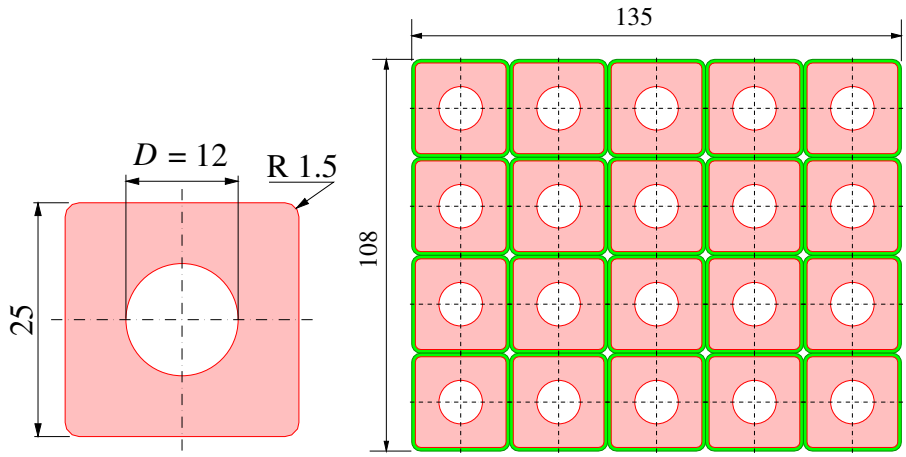

Figure 31. Left: Cross-sectional dimensions in mm of the chosen (copper) conductor. Right: pack of insulated (green) conductors in a racetrack. Dimensions again in mm.

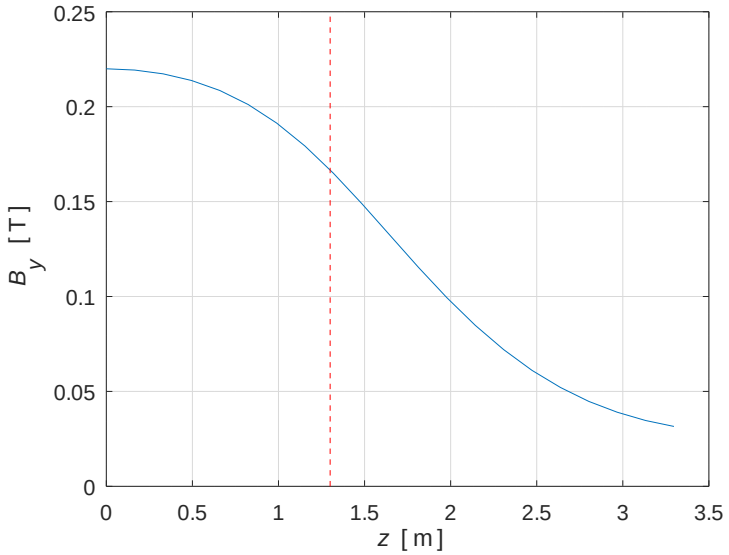

Figure 32. Field on z axis. The dashed- red demarcation line marks the z-extent of the yoke.

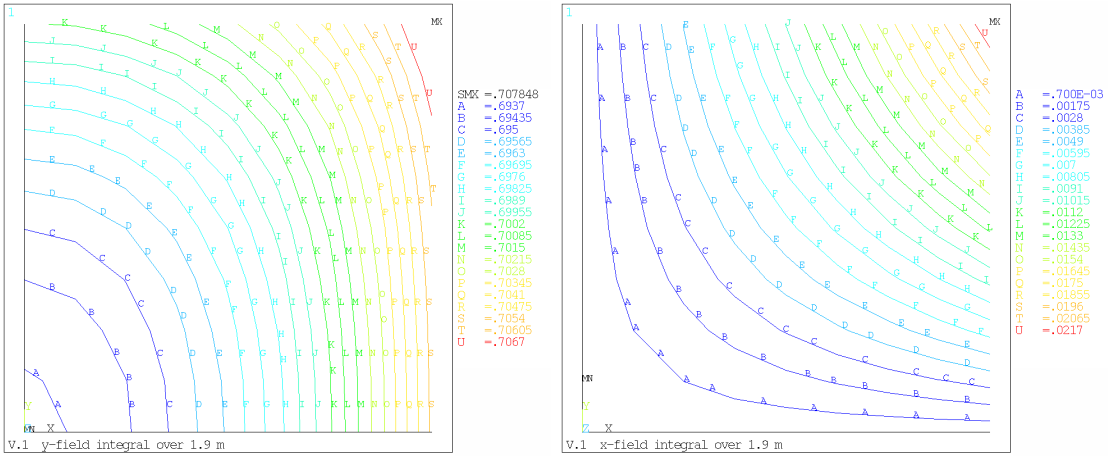

Figure 33. Field integrals in Tm as function of x and y , in the Tracker acceptance. *Short* integration span : $Z_{\text{int}} = 1.9$ m. Left: B_x component. Right: B_y component.

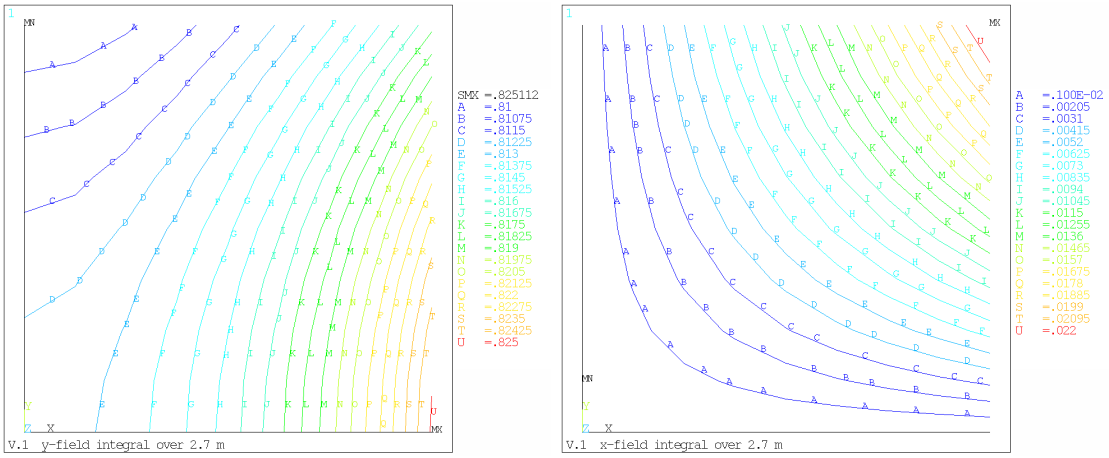

Figure 34. Field integrals in Tm as function of x and y , in the Tracker acceptance. *Long* integration span : $Z_{\rm int} = 2.7$ m. Left: B_x component. Right: B_y component.

5.3 Timing Detector

The timing detector has to provide a time resolution of $O(100-150)$ ps to reject combinatorial backgrounds made of out-of-time charger tracks, mostly muons. Several options are possible and we are currently investigating the interest from several groups.

1. *Scintillating bars:* scintillating bars read out by arrays of silicon photomultipliers. This option has been considered for the SHiP timing detector. The detector comprises more than 500 bars of EJ200 scintillating material with dimensions 168 cm×6 cm×1 cm. The end of each bar is read out by an array of eight SiPM attached to custom PCBs. A time resolution of ∼80 ps almost uniform along the bar length has been demonstrated on prototypes [37].

2. *Glass Multigap Resistive Plate Chambers, glass-RPC*: This option is based on the RPC technology derives from a novel concept of Multigap Resistive Plate Chambers (MRPC) with a Sealed Glass Stack (SGS). Also this option has been considered for the SHiP timing detector. A time resolution of < 60 ps has been measured on prototypes.

3. *Scintillating pads*: a double layer of the redesigned scintillating pads considered for the muon detector (see below) could provide a timing detector with ∼150 ps time resolution.

5.4 Electromagnetic calorimeter

The electromagnetic calorimeter (ECAL) has to fulfil several purposes:

- *Energy measurement.* While for $e^{\pm}$ an accurate energy measurement is needed for their identification (see below), the γ energies and positions directly enter the measurement of the mass of decaying particles. For both purposes, an energy resolution of about $\sigma(E)/E \sim 10-15\%/\sqrt{E(\mathrm{GeV})}$ is sufficient for the goals of SHADOWS.

- *Particle identification.* The $e^{\pm}$ identification is done by the measurement of the ratio E/p with the energy E measured in the calorimeter and the momentum p in the spectrometer. By requiring the E/p ratio to be close to 1, $e^{\pm}$ can be identified with an efficiency of $\mathcal{O}(99\%)$ and a $\pi^{\pm}$ misidentification rate of $\mathcal{O}(1\%)$. This may further be improved by also measuring the shower shapes.

- *Shower direction.* For decays into at least two charged particles, the decay vertex can be reconstructed from the spectrometer tracks, which allows an accurate mass measurement of the decaying particle even if some decay products are π^0 or γ. However, for decays into only neutral particles like the decay of an Axion-like Particle $X \to \gamma\gamma$ (the most likely decay in many ALP models) the γ direction needs to be known to reconstruct the mass of the A particle. For this reason a measurement of the shower direction (pointing capability) is required for reconstructing decays into only neutral particles. Pointing capability can only be achieved by longitudinal segmentation of the calorimeter.

In the following we describe several options for the ECAL design which are currently under study. For all considered options we do have expertise inside the collaboration. The final decision on the ECAL design will be taken in the upcoming months, based on detailed simulations and taking into account both physics requirements and financial constraints.

5.4.1 Shashlik option

Electromagnetic sampling calorimeters in the Shashlik technique consist of alternating layers of a heavy absorber plates that generate the electromagnetic showers, an active medium (scintillator) that provides light signals, wave-length shifting (WLS) fibres that run through holes in the scintillator and lead plates to collect the light, and photo-detectors for the readout of the light. This technology has been used successfully since the 1990s and was applied for the calorimeters of E865 and the PHENIX experiments at BNL, for the calorimeter of the HERA-B experiment at DESY and for the LHCb experiment at CERN [38–42].

Shashlik calorimeters are very stable and reliable detectors. Low costs together with a well understood construction method and an energy resolution better than $10\%/\sqrt{E[\mathrm{GeV}]}$ make this technique to a very suitable choice for SHADOWS. Figure 35 shows Shashlik calorimeter modules produced for the KOPIO experiment at BNL at different stages of the module assembly [43].

Energy resolution: The energy resolution of Shashlik sampling calorimeters depend on the absorber material, the thickness of the absorber and the scintillator plates, the type of the scinitillator and the WLS fibres, and the photo-sensors. Typically, lead plates of a thickness between 1.5 and 2 mm together with plastic scinitillator plates of about 4 mm have been used. The transverse dimensions of the calorimeter modules is mostly defined by the required spatial resolution and varies from 22×22 to 110×110 mm^2. The longitudinal dimension of the module, given by the number of sampling layers, typically correspond to a total depth in range from 16 to 20 X_0. For these parameters a typical energy resolution for electrons of

$$\frac{\sigma_E}{E} \simeq \frac{(8-9)\%}{\sqrt{E[\mathrm{GeV}]}} + (1-2)\%,$$

with E being the electron energy in GeV, is achieved. The constant term of 1-2% accounts for longitudinal non-uniformity, electromagnetic shower leakage and electronic noise.

The energy resolution can be further improved using much thinner sampling plates. This approach was tested for the KOPIO experiment. Shashlik modules with 0.35 mm (0.275 mm) lead sheets and 1.5 mm thick scintillator plates and a total depth of 15.9 X_0 corresponding to 240 (300) layers, respectively [44]([43]), have been built. For photons with 50 to 1000 MeV, an energy resolution of $\sim 3\%/\sqrt{E}$ was achieved[43]. Figure 36 shows the energy resolution for electrons with different WLS fibres and photon detectors [44]. Simulation studies of the absorber and scintillator thickness have further shown that an energy resolution with a sampling term $\frac{\sigma_E}{E}$ smaller than 2% can be achieved for appropriate selections of the material thicknesses (e.g. lead sheets with 0.35 mm together with scintillator plates thicker than 3 mm) [44].

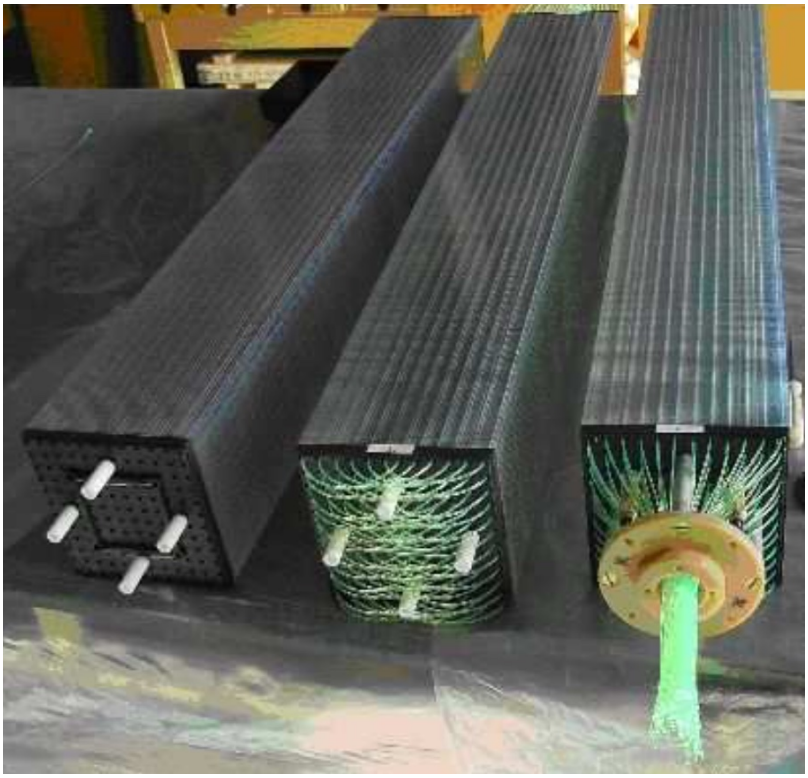

Figure 35. Photograph of prototype Shashlik modules manufactured for the KOPIO experiment at different stages of their assembly. Figure taken from Ref. [43].

Time resolution: The KOPIO experiment has also measured the time resolution of the calorimeter modules in [43] using a 340 MeV photon beam. An energy dependent time resolution,

$$\sigma_t = \frac{(72 \pm 4)\ \text{ps}}{\sqrt{E(\text{GeV})}} \oplus \frac{(14 \pm 2)\ \text{ps}}{E(\text{GeV})},$$

mostly limited by fluctuations in the light collection, was found. Faster WLS fibres could further improve the time resolution.

Spatial resolution: The center position of the electromagnetic showers is determined from the lateral energy distribution in neighboring cells. The availability of low cost silicon photo-multipliers (SiPMs) allows a finer lateral segmentation by reading-out individual WLS fibres. This would allow the determination of the shower position even within a module. The PHENIX collaboration [45] tested an array, 12×12 Shashlik modules, in an electron beam with energies of 5 to 80 GeV. The individual modules had lateral cross-sections of 52.5×52.5 mm^2. The obtained position resolution is described by the formula[45]:

$$\sigma_x(\text{mm}) = 1.4\,\text{mm} + \frac{5.9\,\text{mm}}{\sqrt{E(GeV)}}\,.$$

To achieve a direction measurement of the shower, two points must be measured along the shower, which requires a longitudinal segmentation of the module. Alternatively one

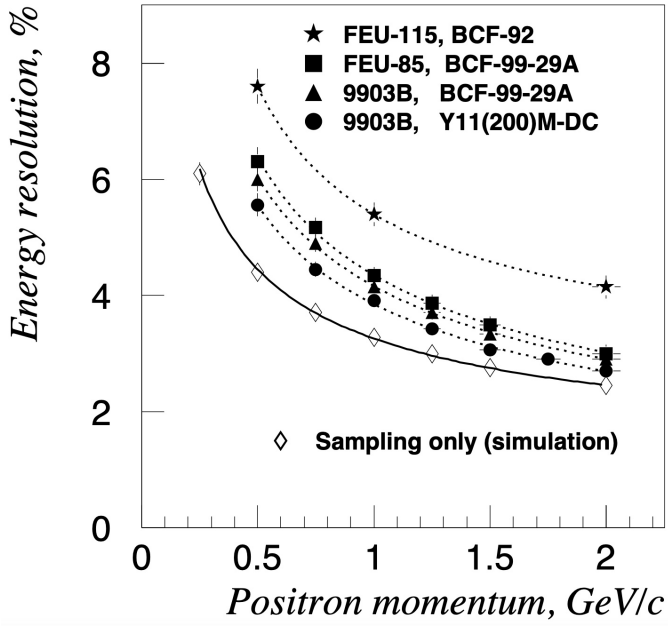

Figure 36. Measured energy resolution of a Shashlik calorimeter (nonet of modules) as function of momentum of the positron beam. The calorimeter modules used 0.35 mm lead sheets, 1.5 mm scintillator plates and had a depth of 240 layers corresponding to a total depth of 15.9 X_0. The measurements were done for four different combination of WLS fibres and photo-multiplier tubes. WLS fibres: BCF-92-SC, BCF-99-29A, KURARAY Y11(200)M-DC. Photo-tubes: FEU85, FEU115 and 9903B. Figure taken from [44]. For details see reference.

can use an independent preshower detector with a depth of 2-3 X_0 placed in front of the calorimeter (see Sect. 5.4.3).

Module design: Electromagnetic calorimeter modules built in the Shashlik technology with very thin sampling layers thus provide excellent energy, time and position resolution. However, the assembly of a Shashlik module from many thin layers poses technological challenges. The KOPIO collaboration has proposed a novel design to simplify the assembly process [43]. Fig. 37 shows how a module with a very fine sampling structure can be assembled using the *Lego lock method*. These locks, four per tile, accurately maintain the mutual position of the scintillator plates providing the air gaps, where lead tiles can be mounted without tight optical contacts between lead and scintillator. In this way the scintillator light is collected by the WLS fibres by total internal reflection, and reflector paper layers can be avoided which otherwise would shorten the effective radiation length by 10%. We propose to adapt a similar concept for the SHADOWS calorimeter.

5.4.2 PbWO4 option

The endcaps of the CMS electromagnetic calorimeter (EE) will be replaced at the end of the LHC Run 3 by a high-granularity and radiation hard calorimeter (HGCAL). Thus

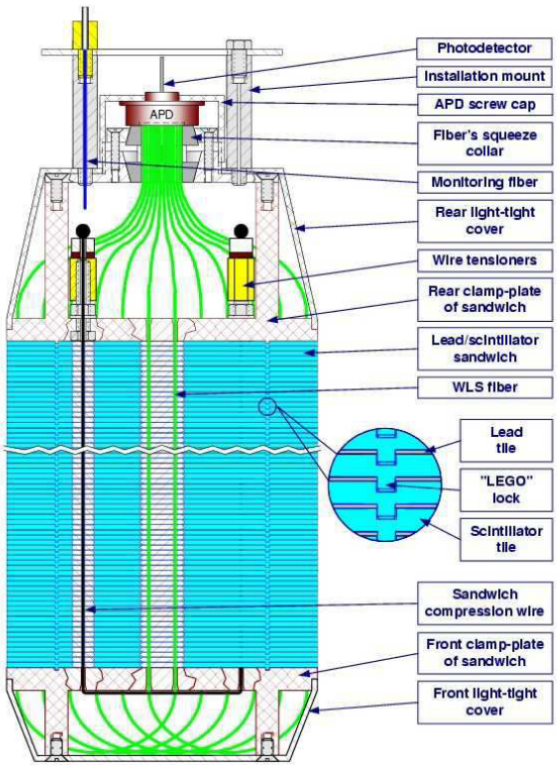

M

Figure 37. Shashlik module design for the KOPIO experiment [43] .

a potential reuse of the replaced detector elements as a SHADOWS calorimeter is under consideration.

The EE sits immediately outside the inner trackers, in a cylindrical volume covering a pseudorapidity from about 1.4 to 3.0. It is a homogeneous calorimeter constructed with about 15000 lead tungstate (PbWO4) crystals. The PbWO4 crystals emit light at a wavelength of 420–430 nm upon excitation by the incident particles. It has a high density of 8.3 g/cm^3, short radiation length of 0.89 cm, and small *Molière* radius of 2.19 cm. The choice of PbWO4 in CMS is also motivated by its radiation hardness of up to 10 Mrad and fast scintillation decay time. The ECAL endcap crystals have a cross section 28.62×28.62 mm^2 at the front face and 30×30 mm^2 at the rear face. They are 220 mm ($\sim 24.7X_0$) in length and are placed with the axes tilted in the direction for the collision region. The crystals are arranged in mechanical units of 5×5 crystals, referred to as supermodules, arranged in a $x - y$ grid.

Photodetectors are installed to the rear of the crystals to detect and amplify the signals. Considering the effect of the strong magnetic field and the radiation environment vacuum phototriodes (VPTs) are chosen for the high-radiation environment in the EE.

The energy resolution σ_E at an energy E for the CMS ECAL can be approximated by

a parameterized function:

$$\left(\frac{\sigma_E}{E}\right)^2 = \left(\frac{S}{\sqrt{E/GeV}}\right)^2 + \left(\frac{N}{E/GeV}\right)^2 + C^2, \tag{5.1}$$

where S is the stochastic term for the fluctuations in the shower containment and photo-electron statistics, N represents the electronics and radiation-background noise, and C is a constant term accounting for the calibration uncertainty and crystal non-uniformity. They are measured to be S = 2.8%, N = 12% and C = 0.3%, yielding a few-percent-level energy resolution.

The EE will be decommissioned at the end of the LHC Run 3 scheduled for the end of 2025. The activated detector needs to be stored and cooled for a period of time before it can be handled. This requires a climate controlled room, for example at the CERN Prevessin site. Special care needs to be given to the fact that the large mass of the EE and the hadronic calorimeter has to be stabilized while being dismantled.

The transparency of crystals is affected by irradiation leading to a reduced response and energy resolution of the crystals. This effect is a function of the crystal position, i.e. pseudorapidity. We estimated that a sufficient number of crystals with a response greater than 30% of the initial response are available. The response of each crystal needs to be calibrated and monitored. In principle the transparency can be recovered by heating the crystals. This would require a special facility and a complete deconstruction of the individual components, i.e. the crystal. Keeping the structure of supermodules intact including the photodetectors is a more feasible scenario. Details on the design of EE can be found in [46].

5.4.3 Pointing Calorimeter option

To obtain a reasonable pointing capability for reconstructing $X \to \gamma\gamma$ decays, a longitudinal segmentation of the ECAL is necessary. This can be realised by an iron or lead sampling calorimeter, with absorber plates orthogonal to the incoming beam direction, and two types of active layers: scintillator layers with coarse spatial segmentation for energy and time measurement, and high resolution layers to determine the transverse position and direction of the shower.

The normal scintillating layers consist of 6 cm wide and 1 cm thick plastic scintillator strips, which span alternating in horizontal and vertical direction over the whole 2.5 m width of the detector. The primary scintillation light of each strip is absorbed by two WLS fibres which are read out by one SiPM on each side of the strip. There is no need for high granularity in these layers, since any ambiguities between shower positions are resolved by the additional layers with high spatial resolution. Studies show that with iron absorbers of 0.5 X_0 thickness an energy resolution of $\sigma(E)/E \sim 15\%/\sqrt{E(\mathrm{GeV})}$ is achievable with this design (see Fig. 39 (left) [47]) as well as time resolutions of a few ns.

SplitCal concept The SplitCal calorimeter, as originally proposed for the SHiP experiment [48], contains only 2-3 additional layers, but with very high resolution of $\mathcal{O}(2\ mm)$ for single shower particles. To enlarge the lever arm for the directional measurement, the

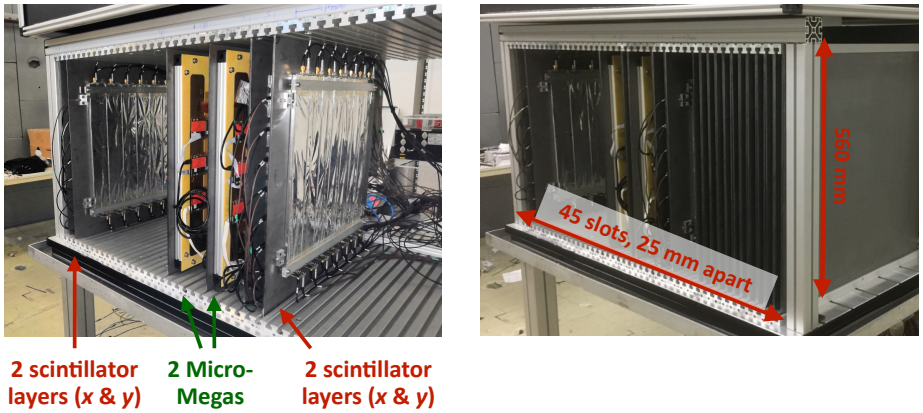

Figure 38. SplitCal prototype without (left) and with (right) absorber layers.

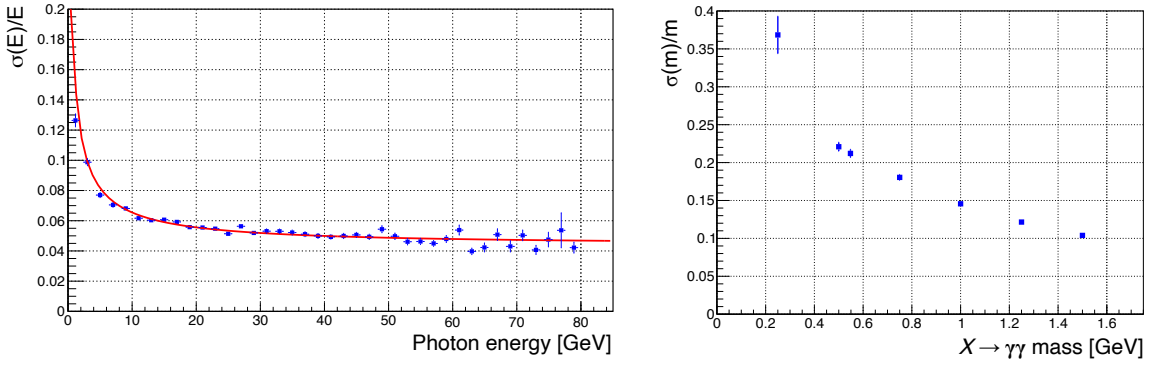

Figure 39. Simulations for the SHiP ECAL with similar dimensions as proposed for SHADOWS [47]. Left: Energy resolution. The fit shown in red yields $\sigma_E/E = 15.5\%/\sqrt{E\,[\mathrm{GeV}]} \oplus 4.4\%$. Right: Mass resolution for different $X \to \gamma\gamma$ masses.

calorimeter together with the high-precision layers may be split into two longitudinal segments which are about 0.5 m apart (thus the name "SplitCal"). A preliminary prototype with four scintillating and two high-precision layers has successfully been operated in test beams at CERN and DESY (Fig. 38).

As a baseline for the high precision layers we consider MicroMegas detectors with two-dimensional readout as they are in use for the ATLAS muon system [26], but with a larger strip pitch of 500 μm which is sufficient for high precision measurements of the shower positions. Each layer would consist of 3×3 double-sided MicroMegas detectors with 85×85 cm^2 active area (larger sized chambers are difficult to manufacture), which results in about 30000 channels per HP layer. The signal readout could be based on the VMM-2 chipset [49], which sparsifies and digitises the signals directly at the detectors.

The mass resolution of $X \to \gamma\gamma$ decays has been simulated for a detector with similar dimensions as teh SHADOWS ECAL using the resolutions as measured with the prototype (see Fig. 39 (right)). For X masses above 500 MeV the mass resolution is 20% or less or about 100-150 MeV in absolute terms.

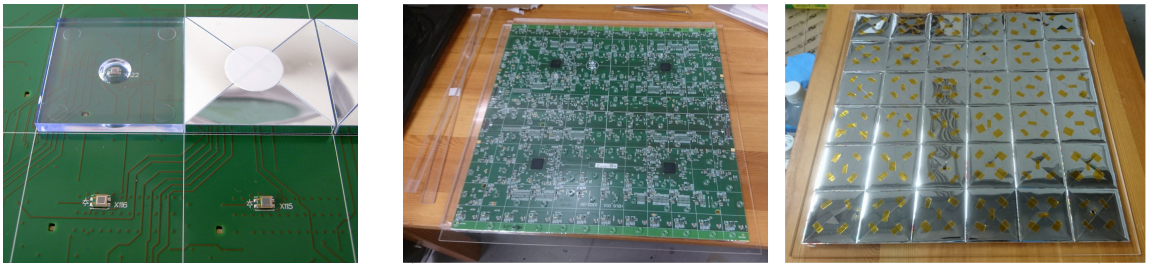

Figure 40. Left: 3×3 cm^2 scintillator tiles of the CALICE AHCAL, wrapped and unwrapped, mounted on a common readout board with SiPMs [50]. Centre and Right: Back and front side of a readout board with 6×6 cm^2 scintillator tiles [52].

Tile concept Another concept for high-resolutions layers are highly granular scintillating tiles. For the ILD detector at the proposed International Linear Collider (ILC) the CALICE Collaboration has e.g. developed a highly granular analogue hadron calorimeter (AHCAL) [50] and a similar detector is being constructed for the CMS High Granularity Calorimeter Upgrade (HGCAL) [51]. Both detectors employ the particle-flow concept for improved jet reconstruction. In SHADOWS, however, direction reconstruction and particle identification is important rather than the application of particle-flow algorithms. It is therefore sufficient to interleave high-granularity layers with regular layers, e.g. having consecutive layers of tiles, vertical strips, and horizontal strips.

For high-resolution layers we consider as baseline option scintillating tiles of 3×3 cm^2 cross section and 1 cm thickness. Each scintillating tile is readout by a single SiPM, which is connected to a common readout board (see Fig. 40 for the Calice AHCAL layout). The SiPM needs a relatively large dynamic range and therefore a large number of pixels for a linear energy measurement of both minimum ionising particles and electromagnetic and hadronic showers. Candidates for such SiPMs are e.g. the existing Hamamatsu types S13360 or S14160 with more than 14000 pixels and a sensitive area of 3×3 or 6×6 mm^2.

Each readout board of 36×36 cm^2 size carries 36 or 144 scintillating tiles, depending on the tile size, wrapped in reflective foil and glued to the PCB. The SiPMs are surface-mounted on the PCB and are housed in small cavities on the bottom side of the tiles (Fig. 40). The front-end electronics together with a digitising ASIC occupy the back side of the readout board. The digitisation therefore takes place directly next to the photo detectors, ensuring an excellent time resolution. A suitable ASIC for the digitisation is the KLauS chip [53], which has been developed at the University of Heidelberg and has been in use for Calice AHCAL readout boards. It should be noted, that in this design it is possible to read-out the strips by the same method and in particular with the same ASIC as the tiles. Only the shape of the PCBs holding the SiPMs would need to be modified.

Assuming a general design with 3×3 cm^2 cells and a front face of 252×252 cm^2 results in 7056 cells in each high-resolution layer. Adding the channels of layers with scintillating strips and assuming a total length of about 15 X_0 results in a total number of about 72000 channels. However, this could be reduced by using less high-granularity and more strip layers.

5.5 Muon detector

The primary role of the muon system is the identification of muons with high efficiency ($> 95\%$), and the subsequent reduction of the hadron contamination to less than 1% in a momentum range between 5 - 100 GeV/c. Furthermore, it complements the timing detector in rejecting the combinatorial muon background pairs from the beam muon halo. The combinatorial muon background from beam halo is spread along spills 4.8-sec long and can be controlled by requiring a tight ($< 3 \cdot \sigma_t$, $\sigma_t \sim 150$ ps) time coincidence of the two tracks.

In order to meet the efficiency and purity requirement, four active stations are foreseen, with an area of $\sim (2.5 \times 2.5)$ m^2, interleaved by iron filters $\sim 3.0\lambda_I$ thick. In order to achieve the required time resolution over the four stations, a time resolution of ~ 300 ps per station is required. No significant spatial resolution is required, with segmentation over the plane driven primarily by background occupancy concerns and ease of construction.

The basic active element of the muon detector will be a plastic scintillator tile of $(150 \times 150 \times 10)$ mm^3 which will be read out by four Silicon PhotoMultipliers (SiPMs). Approximately 1100 tiles will be needed to equip the four stations. The tiles will be grouped in *modules* of 16 or 32 tiles each. Each stations will be equipped with 8 or 16 modules, installed on both sides of a supporting structure in a staggered chequerboard pattern: such a design allows both the dead zones to be minimised and the weight on the supporting wall to be equally shared between the two wall sides. Each station can slide on rails to ease the access to the modules during installation/repair. A schematic layout of the SHADOWS muon system is shown in Figure 41.

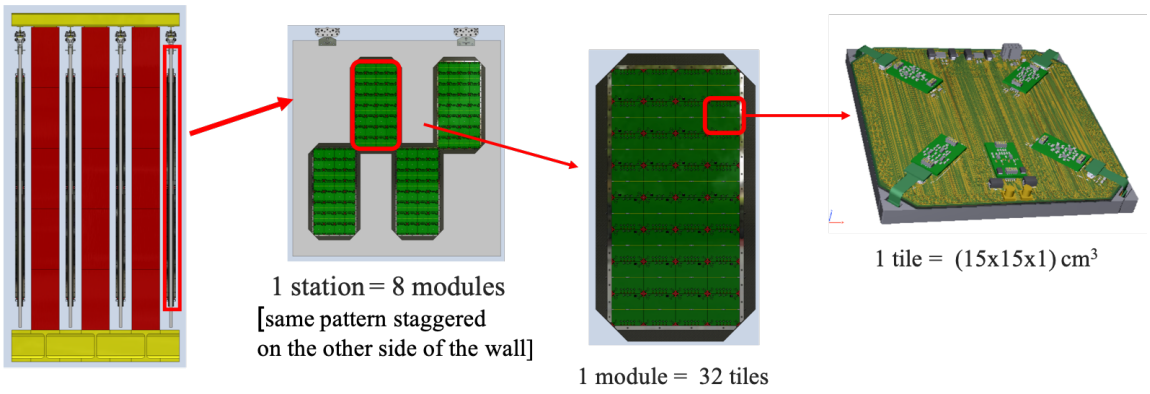

Figure 41. Schematic layout of the SHADOWS muon system. The system is made of four active stations interleaved by passive filters. Each station is made by 8 or 16 modules, 16 or 32-tile each, respectively. The modules are organised in a chequerboard pattern. Each tile covers an area of ~ 225 cm^2.

A combination of plastic scintillators and SiPMs offers a prompt response and generous signal amplitude with a relatively low number of channels, and therefore represents an excellent compromise for a system of this size. In addition to a very good timing per-

formance, the choice of tiles guarantees the determination of the x, y coordinates with a single active layer and a good tolerance against hit rate variations.

Studies performed on similar scintillator-based detectors show that this technology is suitable for detectors exposed to an integrated dose of about 100 kRad/year. The reliability of scintillators and SiPMs, which limits the needs for maintenance, as well as the lack of requirement for infrastructure located near the detector are well suited to the limited space available in the experimental hall.

5.5.1 Prototype tile studies

Four tile prototypes have been built and characterised at several test stands in Frascati and Bologna INFN laboratories and their performance assessed during a test beam at the Beam Test Facility (BTF) of Laboratori Nazionali di Frascati in January 2021 [54]. The aim of this study was the characterization of the performance of different scintillator manufacturers and different assembly techniques.

Two (out of four) tiles were made of PVT-based EJ200 cast scintillator from Eljen [6] and the other two of PS-based scintillator from UNIPLAST (Vladimir, Russia).

Each tile was read out by four Hamamatsu S14160-6050HS[7], with 6×6 mm^2 active area each. The SiPMs were mounted on short Kapton flex cables that ensure the connection with the front end board mounted above the tile. SiPMs were either glued into slots machined in the scintillator or glued on the bevelled corners, with Eljen EJ-500[8] bi-component optical glue. In both cases the SiPMs were pointed towards the centre of the tile.

Three out of the four tiles were painted with three coats of Eljen EJ-510[9] reflective painting, while the fourth one was covered by a chemical reflector obtained by etching the scintillator surface in a chemical agent, that results in the formation of a white micropore deposit over polystyrene.

The main characteristics of the four tiles that were tested are summarised in Table 6.

Table 6. Main characteristics of the four tiles under test and average breakdown voltage of the four SiPMs in each tile.

	Scintillator	SiPM placement	coating	V_{break} (V)
Tile 1	EJ200	slots	painting + Teflon	38.34 ± 0.06
Tile 2	EJ200	corners	painting + Teflon	38.43 ± 0.09
Tile 3	UNIPLAST	slots	etching + Teflon	38.55 ± 0.05
Tile 4	UNIPLAST	slots	painting + Teflon	38.31 ± 0.08

An example of prototype with the four SiPMs connected to flex cables and glued in slots engraved at the tile corners is shown in Figure 42. All tiles were later wrapped with Teflon tape to ensure light tightness, and the readout electronics mounted on top.

[6] https://eljentechnology.com/products/plastic-scintillators/ej-200-ej-204-ej-208-ej-212
[7] https://www.hamamatsu.com/eu/en/product/type/S14160-6050HS/index.html
[8] https://eljentechnology.com/products/accessories/ej-500
[9] https://eljentechnology.com/products/accessories/ej-510-ej-520

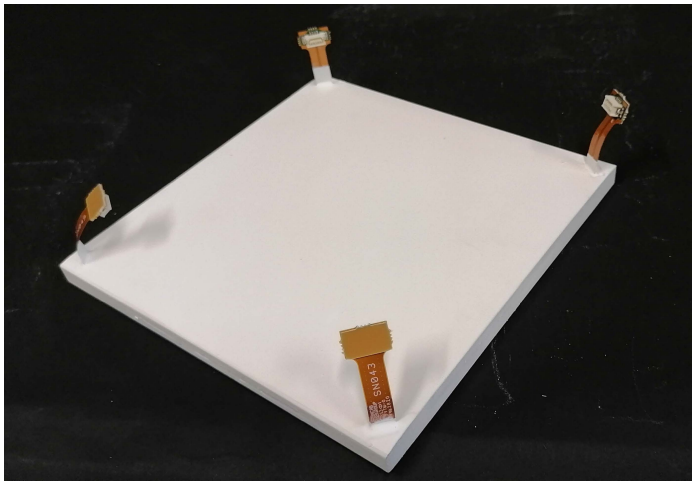

Figure 42. Tile prototype with white reflecting painting. The four SiPMs are attached to flex cables glued in slots machined in the corners of the scintillator tile.

5.5.2 Front-End Electronics

In order to maximise light collection and improve photon statistics, relatively large area SiPMs have been chosen. A common issue that the large sensor area introduces is the significant parasitic sensor capacitance (up to 2 nF), which requires a low input impedance amplifier in order to maintain an acceptable bandwidth. In order to satisfy this requirement, we have opted for an architecture that employs a single NPN transistor in common base configuration, AC coupled to each SiPM, with a common summing amplifier based on a fast Op-Amp. The Front-End is shown in Fig. 43.

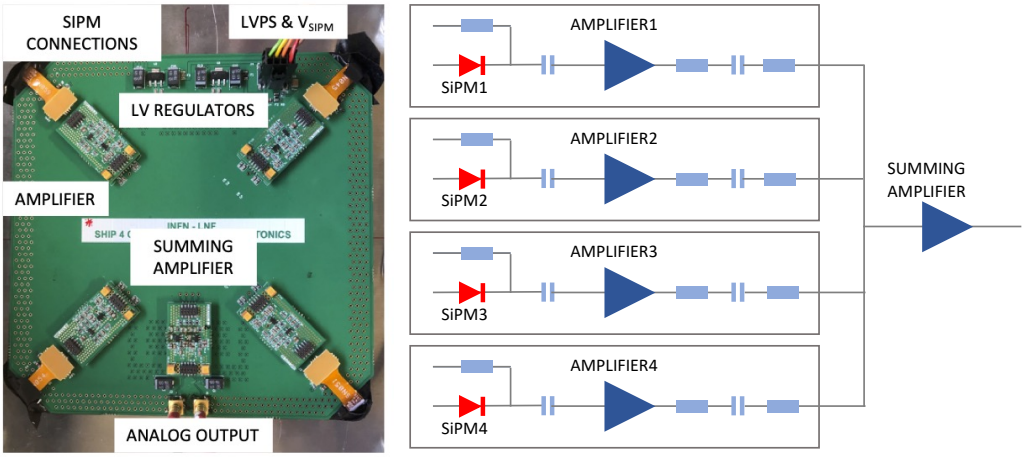

Figure 43. Picture of a fully instrumented tile (left) and its readout circuit block diagram (right).

Measurement of the SiPM and analog electronics chain up to the output of the summing amplifier have been conducted, and the resulting time resolution for a large amplitude laser

signal (similar to the expected tile signal) has been found to be under 80 ps over a wide range of bias voltages.

Several digitisation schemes have been considered for the analog signals, with the baseline option represented by the integration of a hardware Constant Fraction Discriminator on the Front-End board, followed by a 32 channel PicoTDC ASIC[10], housed on a custom board mounted either on a module or immediately adjacent to the detector. It is foreseen to develop this PicoTDC board jointly within the SHADOWS and HIKE collaborations in order for it to serve other timing critical subdetectors as well. The PicoTDC ASIC can resolve both rising and falling edge of a signal with better than 10 ps resolution, providing not just the signal arrival time but also a measurement of amplitude via the time-over-threshold method.

After grouping the SiPMs by nearest breakdown voltage, the spread within a group is sufficiently small to operate all four at a common bias, however each tile will need to be tuned to its optimal working point. A per-tile discriminator threshold will also be provided. A per-module service board will provide the power distribution and slow control signals to set thresholds and biases.

5.5.3 Measurements on beam and with cosmic rays

The four tiles described in the previous section were assembled in a *mini-module*, essentially a light tight box and faraday cage with a side mounted patch panel, shown in Fig. 44 intended to test on a smaller scale the electrical and mechanical integration of multiple tiles. This module was placed on an electron beam at the Beam Test Facility (BTF) of INFN's Laboratori Nazionali di Frascati; the beam was configured to have an energy of 450 MeV, with an average particle multiplicity per bunch of 1.8, and a spot size of a few mm^2.

A scintillator cube of $(1 \times 1 \times 1)$ cm^3, fixed with respect to the beam and read out by two SiPMs, provided the trigger, time reference ($\sigma(T_0) \sim 80$ ps), and allowed to select events with a single charged particle by means of an amplitude cut. The four tiles' SiPMs were powered at a bias voltage of V_{bias}=41.5 V at a temperature of about 26°C. Analog signals from the four tiles were digitized by a 12-bit 5-GS/s waveform digitizer module (CAEN V1742), which also received the signals from the trigger SiPMs.

The average signal amplitude, delay and jitter were measured over a representative set of points over the four tiles, a subset of which is reported in table 7. All four tiles show excellent light yield, and a very uniform single point time resolution.

In order to more correctly evaluate the time resolution over the full area of the tile, and to measure the detection efficiency, a separate cosmic ray setup was built, with the four tiles stacked on top of each other outside the mini-module, at varying distances. Increasing the area over which the cosmics ray produced a valid trigger, the time resolution degraded with respect to single point by a few tens of ps, with measured values between $\sim 260 \pm 25$ ps and $\sim 300 \pm 30$ ps. Finally, the efficiency was measured thanks to an external trigger built

[10] picoTDC: Pico-second TDC for HEP, CERN and University of Barcelona

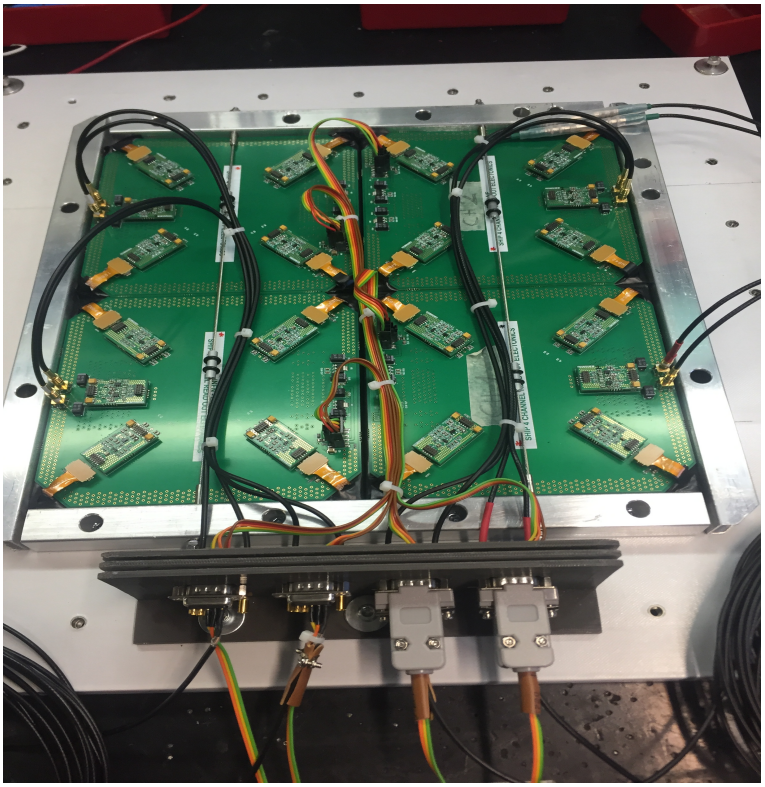

Figure 44. Picture of the minimodule exposed in the test beam.

Table 7. Selected results of the scan over the mini-module. The corner, adjacent to the SiPM, has the largest signal amplitude and often the best time resolution. The time resolution is already corrected for the T_0 time jitter, while the conversion of the light yield in photo-electrons is performed by calibrating the single photoelectron response in a separate measurement.

Tile n.	Label	Position [cm,cm]	Average arrival time [ns]	arrival time resolution [ps]	light yield [N p.e.]
1	Centre	[-7.5,7.5]	8.93±0.003	226±2	230±20
1	Corner	[-1.5,1.5]	7.992±0.003	228±3	520±80
2	Centre	[7.5,7.5]	8.696±0.003	237±3	186±16
2	Corner	[1.5,1.5]	8.542±0.003	223±3	640±110
3	Centre	[7.5,-7.5]	9.188±0.003	229±2	207±18
3	Corner	[1.5,-1.5]	7.87± 0.003	227±3	680 ± 200
4	Centre	[-7.5,-7.5]	10.231±0.003	248±2	138±13
4	Corner	[-1.5,-1.5]	9.898±0.003	207±3	397 ± 78

out of smaller scintillating tiles, finding values above 99.8% in the nominal bias voltage range (Fig. 45).

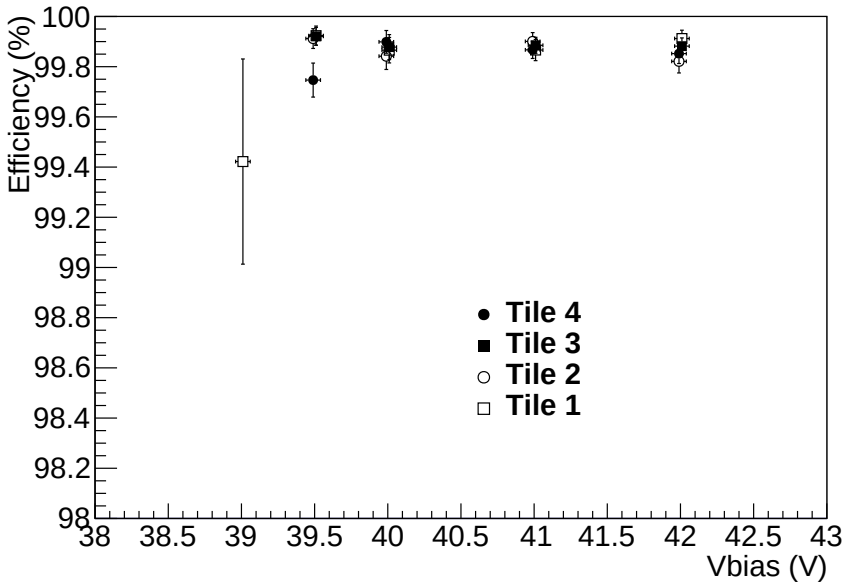

Figure 45. Efficiency values measured for the four prototype tiles as a function of bias voltage.

5.5.4 Outlook

The muon group is currently building a 15 tile module using the design of prototype Tile 1 and an improved front-end electronics. In addition to enabling the systematic performance evaluation of the detector, the construction of this intermediate scale prototype will provide us with realistic cost estimates for the full detector.

6 Monte Carlo simulation

6.1 Monte Carlo framework

SHADOWS full Monte Carlo simulation is part of the general NA62 Monte Carlo framework and is a C++, GEANT4-based code (version 4.10.03) able to simulate the interactions of the particles with the detector elements.

The integration of the simulation of SHADOWS and NA62/HIKE detectors within the same framework has several advantages:

i) a centralised production of signal and MC samples that can be used by both experiments resulting in large CPU power and disk space savings;

ii) the possibility of study the mutual interference as far as the background is concerned (relevant mostly for the impact of SHADOWS material and magnetic elements on the NA62/HIKE background) ;

iii) the possibility of easily combine physics results, having in common the simulation of the production processes (both signal and background) and their interactions with the (common) dump and magnetic elements of the beam line.

The signal is generated with `PYTHIA 8.32` and the background using the `Beam Delivery Simulation` or `BDSIM` package [55]. The output of `BDSIM` package and of `PYTHIA 8.32` is then handed over to the SHADOWS full Monte Carlo where the simulation of interactions of the particles with the detector material and SHADOWS magnetic elements is performed.

In the following paragraphs the status of the simulation of the beamline, detector is detailed and the signal and background simulated data samples described.

6.2 Beamline simulation

The proton interactions with the dump and the rate, composition, and evolution of the beam-induced backgrounds, is studied by using a GEANT4-based simulation of the P42/K12 beam line including the target and TAX area and all the magnetic elements placed along the beam has been developed by the NA62 collaboration and the BE-EA-LE team. This simulation is based on `BDSIM` [55]. The products of the interactions of the 400 GeV proton beam with the TAX material are simulated, transported across the magnetic elements of the K12 beam line, and their kinematic properties and composition stored for further processing.

`BDSIM` uses a suite of standard high energy physics codes (GEANT4, `ROOT` and `CLHEP` to create a computational model of a particle accelerator that combines accurate accelerator tracking routines with all of the physics processes of particles in GEANT4. This unique combination allows one to perform the radiation and detector background simulations in accelerators where both accurate tracking of all particles is required over long range, as well as interaction with the material of the accelerator. We use `BDSIM` 1.6 version that is based on GEANT4-10-07-PATCH-02 [56–58].

The beam line elements are described using the Geometry Description Markup Language (GDML) an XML based file format that enables the user to prepare geometries for applications that support it, and then placed at a relative location one after the other following the structure of the P42/K12 beam line. The `BDSIM` model used in the simulation comprises: i) the beam parameters, ii) the field maps for each magnetic element; iii) the geometry and material composition of each constituent of the beam line; iv) the relative position of the elements.

The 400 GeV proton beam, moving along the z coordinate, is let to interact with the K12 TAXes system. The overall TAX thickness corresponds to approximately 21 proton interaction lengths. The beam impact point is $(0, -2)$ mm in the transverse (x, y) plane. The products of the inelastic interactions of the primary protons with the TAX material with energy above a given threshold E_{thr} are simulated and let further interact with the material or decay. The GEANT threshold adopted for this study is $E_{thr} = 3$ GeV. The GEANT4 physics list `FTFP_BERT` is used and the simulation of short-lived particles is turned on.

6.3 Detector simulation

Figure 46 shows the GEANT4 visualization of the full SHADOWS spectrometer in the lateral and 3D views. The conceptual layout of the detector is shown in the top plot for reader's convenience.

All the sub-detectors but the dipole magnet of the spectrometer have been implemented in the simulation with a realistic technology.

Whenever more than a technology option is under study, only one of them is picked up in the simulation. For the Upstream Veto (Figure 47) a single layer with scintillating tiles has been implemented because the option with MicroMegas (that will be the final choice for SHADOWS) has been considered only recently. For the tracking system four chamber instrumented with four layers of 10 mm diameter STRAWS tubes and the same orientation as in the NA62 detector (Figure 48). The dipole magnet of the SHADOWS spectrometer is still not implemented in the Monte Carlo as the detailed design has been deployed too late to be included in the simulation (it will be for the Proposal). The timing detector is implemented as a double layer of scintillating bars with horizontal and vertical orientation (Figure 49). The ECAL implemented in the simulation corresponds to the Shashlik technology (Figure 50). The Muon system comprises four muon stations instrumented with scintillating tiles and interleaved by iron filters, 30 cm thick except the first one between ECAL and the first muon station that is 50 cm thick.

Table 8 summarises the technologies implemented for every sub-detector. The individual sub-detectors are shown in Figures 47, 48, 49, 50, 51.

No reconstruction code able to folding the raw hits with the simulated detector response and reconstruct high-level objects, as tracks, vertices and electro-magnetic showers has been developed yet (it will be ready for the Proposal). This means that the signal and background analyses shown in the next Chapters are based on the MC truth information associated to the GEANT4 MC hits released in the detector.

Table 8. Simulated SHADOWS sub-detectors in the full Monte Carlo and corresponding technologies.

Detector	Technologies under evaluation	Technology implemented in MC
Upstream Veto	MicroMegas	Scintillating Tiles
Tracking chambers	STRAWS, Fibres	STRAWS
Dipole Magnet	warm magnet	–
Timing detector	Scintillating bars, RPC	Scintillating bars
ECAL	Shashlik, PbWO4 crystals, CALICE	Shashlik
Muon System	Scintillating tiles	Scintillating tiles

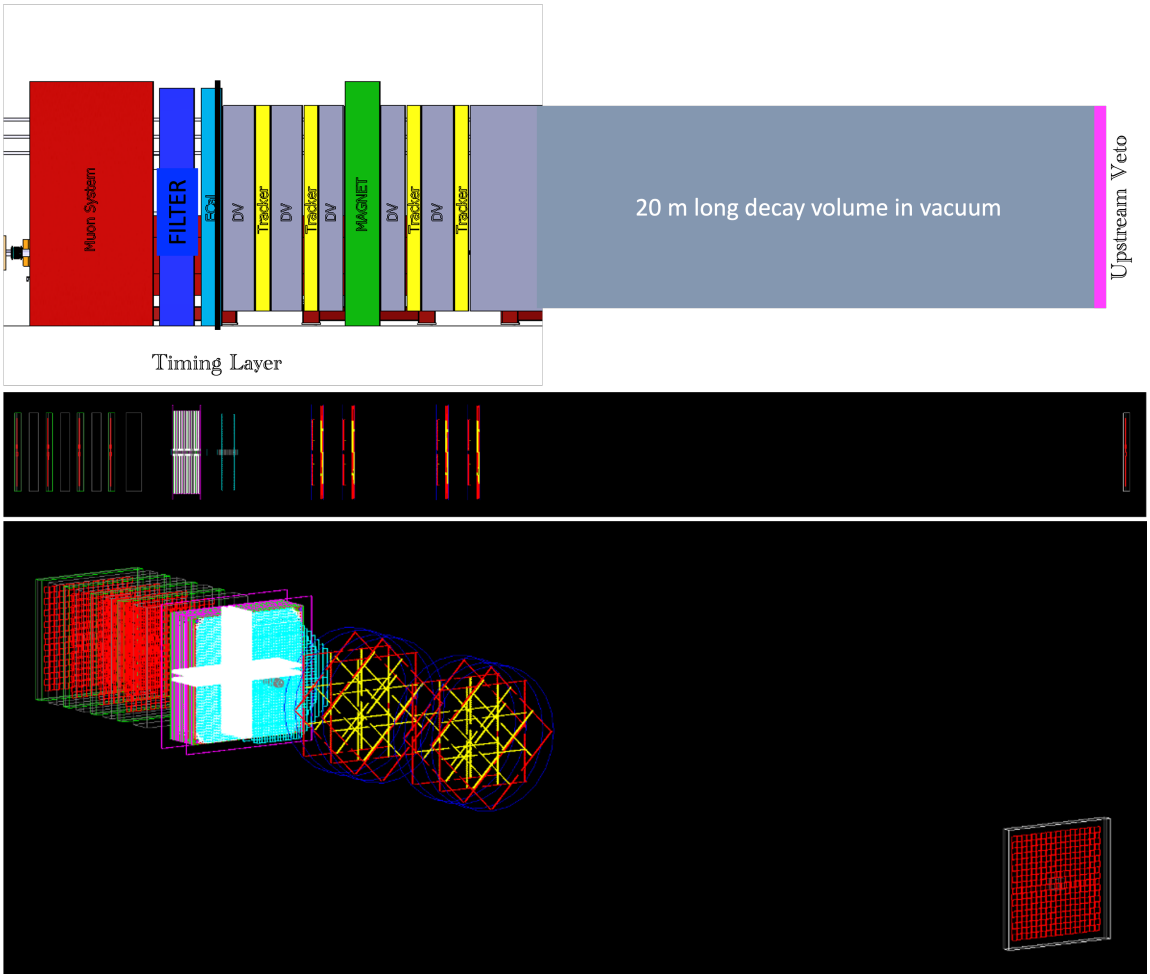

Figure 46. Top: conceptual layout of the spectrometer. Medium and bottom: GEANT4 visualization of the SHADOWS detector (top: lateral view, bottom: 3D view). The dipole magnet is not implemented while the decay volume is omitted to show more clearly the sub-detectors.

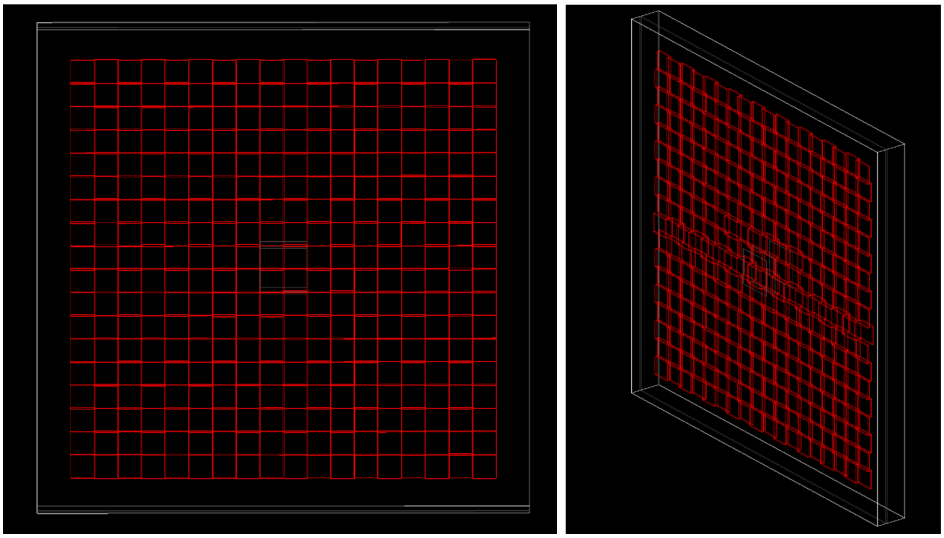

Figure 47. GEANT4 visualization of the SHADOWS Upstream Veto. Top: front view, bottom: 3D view.

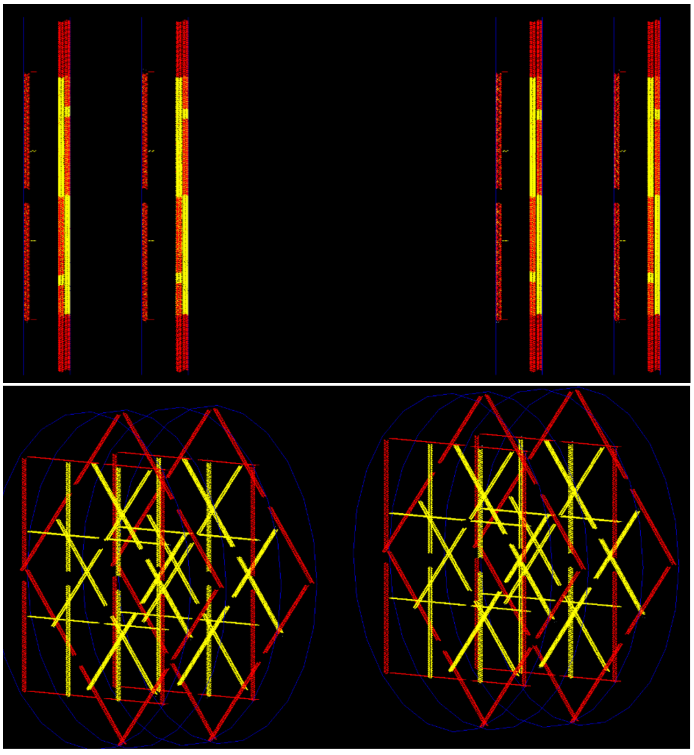

Figure 48. GEANT4 visualization of the SHADOWS STRAW tracker. Top: front view, bottom: 3D view.

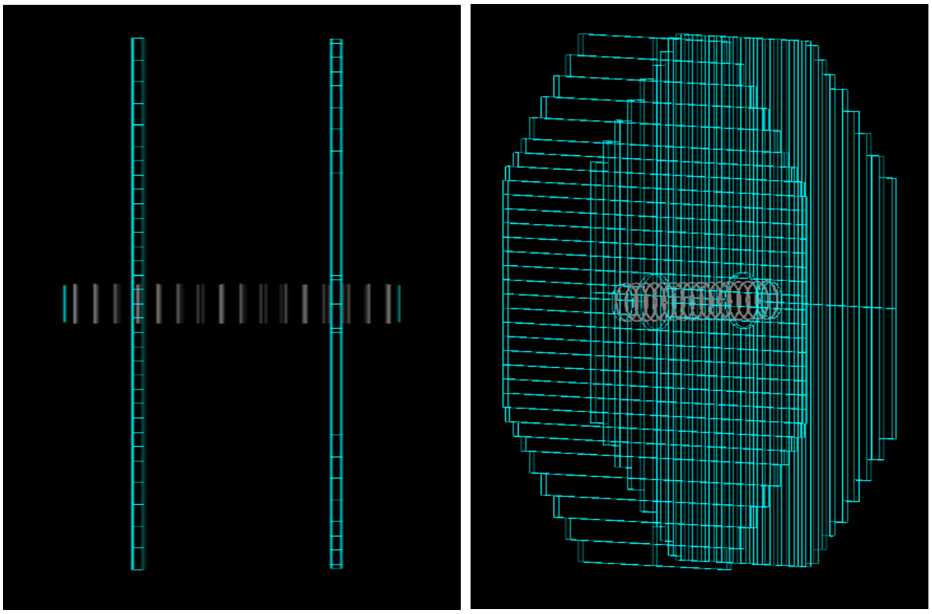

Figure 49. GEANT4 visualization of the SHADOWS Timing detector. Top: lateral view, bottom: 3D view.

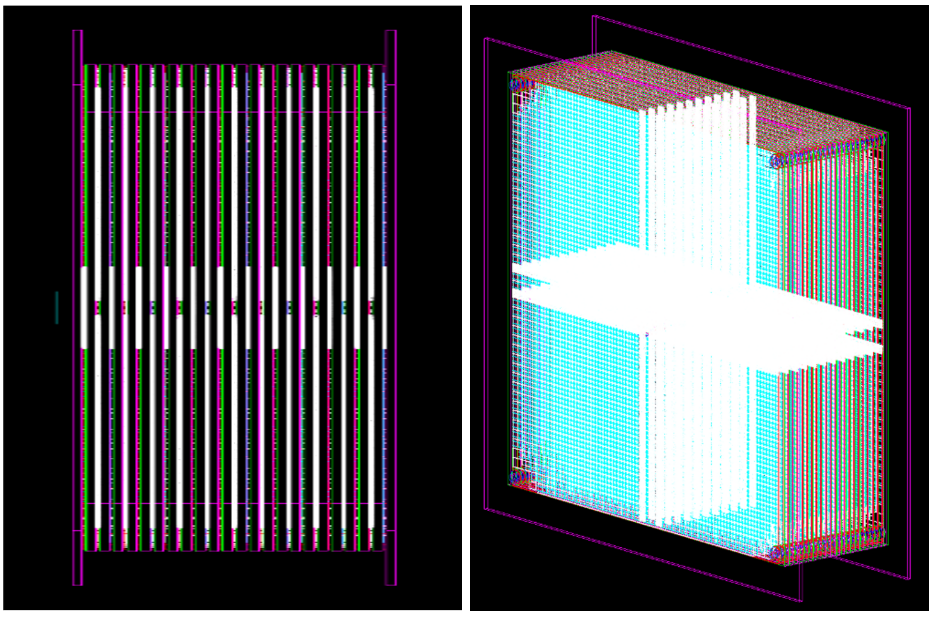

Figure 50. GEANT4 visualization of the SHADOWS ECAL. Top: lateral view, bottom: 3D view.

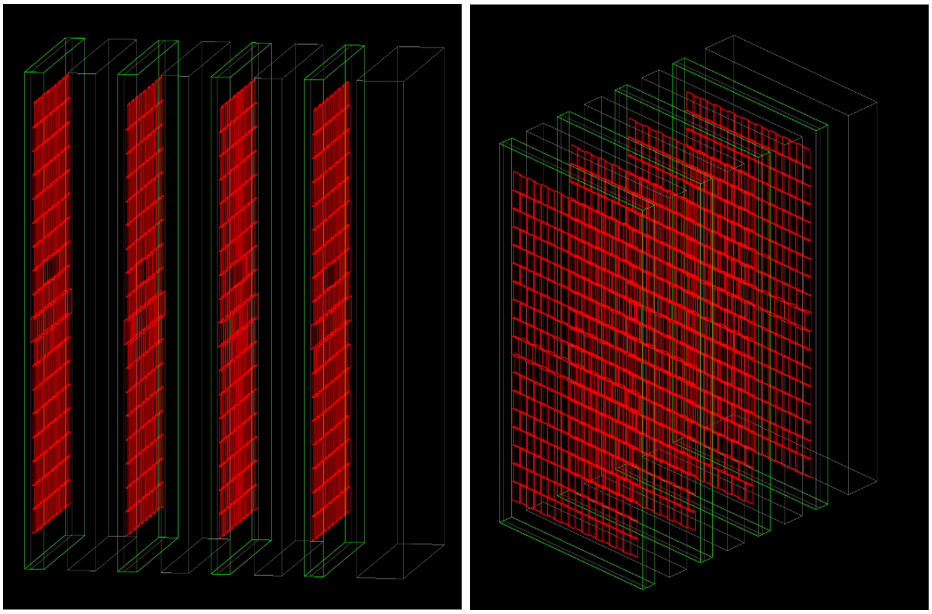

Figure 51. GEANT4 visualization of the SHADOWS Muon system. Left: lateral view, right: 3D view. The four iron filters are shown in green.

6.4 Monte Carlo signal samples

The SHADOWS detector, being off-axis, is sensitive to FIPs emerging from the dump with a sizeable polar angle. This can occur in the decay of mesons/baryons containing heavy quarks (charm and beauty) produced in the interactions of 400 GeV/c protons with the Cu-based dump. We remind that the probability of producing a $b\bar{b}$ and $c\bar{c}$ pair is given by $\chi_{c\bar{c}} = \sigma_{c\bar{c}}/\sigma_{pp} \sim 3.9 \cdot 10^{-3}$ and $\chi_{b\bar{b}} = \sigma_{b\bar{b}}/\sigma_{pp} \sim 2.7 \cdot 10^{-7}$[59, 60], respectively, where both include also secondary heavy quark production in the hadronic shower. In SHADOWS beauty and charm production are simulated using `Pythia` 8.32. We do not simulate - for the time being - secondary interactions and assume that the whole yield of charm and beauty come from primary interactions only. This is a conservative assumption given the fact that secondary interactions produce lower p heavy quarks and therefore enhance the acceptance for an off-axis spectrometer.

The kinematic distributions of charmed and beauty mesons are obtained with `Pythia 8.32` by simulating the interactions of 400 GeV/c protons with a Cu-based dump following the study in Ref. [60]. For charm production we run Pythia with the tuning proposed by SHiP collaboration, `PARP(91)=1.6` , necessary to reproduce the D p_T spectrum measured by the E791 collaboration with a 500 GeV/c pion beam on a carbon target [61], and store the event when a charm is produced. The transverse momentum p_{T} and energy spectra are then produced for D^+, D^-, D_S^+, and D_S^- and stored for further analysis.

For beauty production, given the low cross-section, we force the production of hard-QCD $b-$quarks and then we re-weight properly to get the $\sigma(bb) \sim 2$ nb of 400 GeV protons interacting with $Cu-$based dump [59]. The output is then re-weighted to match the total pp cross section $\sigma(pp) \sim 40$ mb at 400 GeV. The dependence of the cross section with the material of the dump is taken into account by an $A^{1/3}$ correction.

We are aware of the large uncertainty related to the absolute value of the $b\bar{b}$ cross section at the SHADOWS centre-of-mass energy ($\sqrt{s} \sim 28$ GeV). This is illustrated in Figure 52 (left) where the extrapolation from the closest experimental value measured by HERA-B gives more than 100% uncertainty at the SHADOWS energy. In order to reduce this (large) uncertainty, we are currently investigating the possibility to perform a new measurement of the $\sigma_{b\bar{b}}$ cross section using the proton-gas interactions in LHCb with the brand new SMOG2 system when the circulating beam is still not accelerated, hence it has 450 GeV injection energy. Several gases are currently being investigated (Ar, Kr, Xe). We are currently discussing the feasibility of this measurement with the Project leader of the SMOG2 system, P. Di Nezza, and we hope to have more news in a few months time.

The SHADOWS GEANT4 full Monte Carlo inherits many features developed for NA62 Monte Carlo. In particular includes a special tool allowing the user to simulate a multitude of exotic feebly-interacting particles, production methods, and decay states. This tool is designed intentionally to be robust such that different new physics scenarios can be easily simulated. The logic flow of the generation of a feebly-interacting particle is shown in Figure 53.

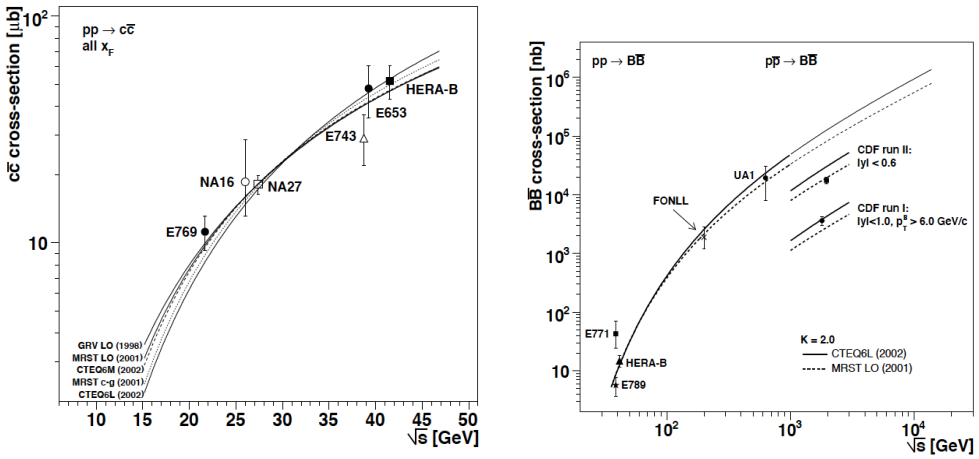

Figure 52. Charm and beauty cross-sections as in Ref.[hep-ph/0609101].

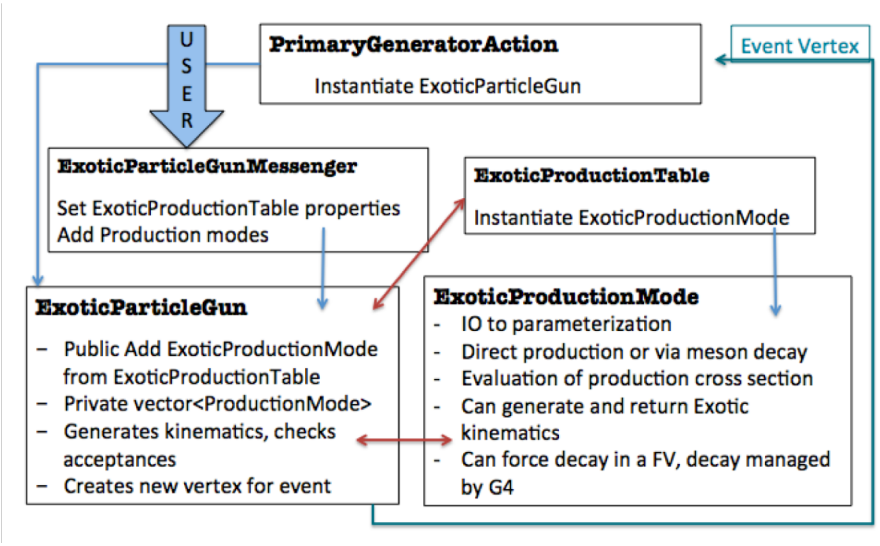

Figure 53. The logic flow of the exotic MC. The `PrimaryGeneratorAction` creates an `ExoticParticleGun` that receives input from the `ExoticParticleGunMessenger`. The particle gun class then passes the parameters to the `ExoticProductionTable` to generate available modes and to the `ExoticProductionMode` to generate the kinematics specific to the event. When the calculation is finished, an event vertex is placed and the simulation returns to the`PrimaryGeneratorAction object.`

To ensure that the correct feebly-interacting particle is generated and that there are no conflicts within the physics lists, the kinematics of production is done outside the GEANT4 simulation. Production is split into two categories: *indirect* and *direct*. For direct production, interactions of the beam with a target produces the feebly-interacting particle, whereas indirect production proceeds through a meson intermediate state.

For *direct production*, the kinematics of the feebly-interacting particle and of any other accompanying particle are calculated directly from the proton interaction. Differential cross sections are then put into a table that is sampled in the `ExoticProductionMode` class. *Indirect production* requires an additional set of steps. First, the kinematics of the meson from the proton beam interaction is generated. The distribution in momentum and θ are produced a priori, using `Pythia 8.3.2`. The meson is then propagated according to its kinematics and PDG lifetime, until it decays into an exotic and an accompanying particle. Since several production modes can be specified in the same run, the `ExoticProductionMode` handles the total cross section and branching ratios such that the number of events for each production mode is in the expected ratio to the others.

Instead of imposing a decay final state on an feebly-interacting-type particle, a task that can be quite difficult, the kinematics of decay is also handled outside of the GEANT4 simulation. The user designates the decay daughters of the exotic particles as well as the region along the beamline where the feebly-interacting particle is supposed to decay. The position of the daughter vertex is determined by uniform sampling in z from a user-specified region. The x and y values of the vertex are determined by the production angle and momentum of the exotic particle. This gives the user freedom to reuse the same MC sample to test different values of the exotic lifetime. A re-weighting of the generated events is then implemented offline, allowing the same MC sample to be reused to evaluate sensitivity for different lifetimes. An example of the decay length distribution for a sample of ALP$\rightarrow \mu^+\mu^-$ generated with infinite lifetime is shown in Figure 54. In the same plot the same distribution is shown by requiring the decay products in SHADOWS acceptance, that clearly enhances the efficiency for decays happening close to the detector.

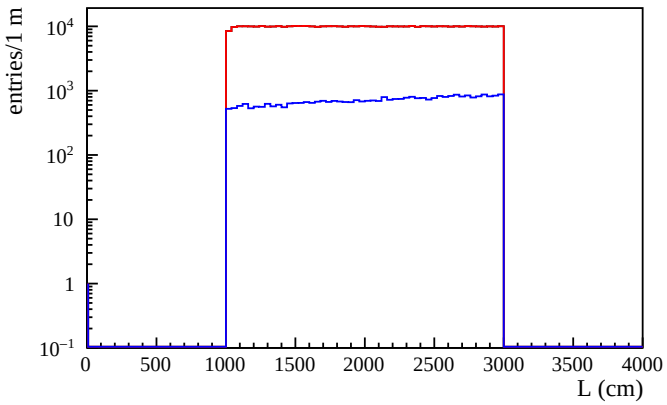

Figure 54. Decay length distribution for a sample of ALP$\rightarrow \mu^+\mu^-$ generated with infinite lifetime in the shadows decay volume without (red curve) and (with) the decay products in the acceptance of the first tracking chamber.

Once the momentum and the vertex position of the decay daughters are calculated, the `ExoticParticleGun` creates a vertex for the event. The vertex contains the decay daughters and any decay partners produced together with the (feebly-interacting) particle.

The laboratory time of each particle is set to the appropriate value, and the vertex is passed to be propagated in the GEANT4 simulation where the SHADOWS detector is implemented.

Figure 55 shows the momentum and transverse momentum distributions of $5 \cdot 10^5$ ALPs$\rightarrow \mu^+\mu^+$ with mass of 700 MeV of the ALP and its the decay products within the SHADOWS acceptance. The blue dots are the results of the full MC code while the solid black curves are the outcome of the toys used to evaluate the physics reach in Section 7. The good agreement between the distributions shows that the toys used to compute the sensitivity curves shown in Section 7 are reliable.

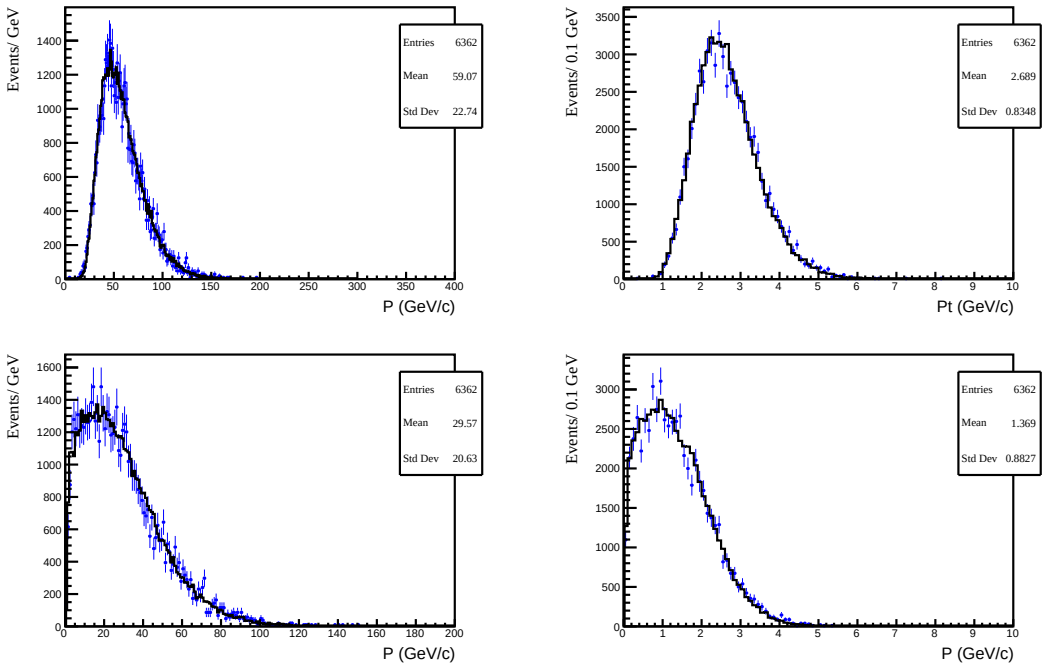

Figure 55. Momentum (left) and transverse momentum (right) distributions of an ALP (top) and its decay products (bottom) for an ALP$\rightarrow \mu^+\mu^+$ decay with a mass of 700 MeV when both decay products are in SHADOWS acceptance. Blue dots correspond to a sample generated with the full MC and black solid line is the outcome of the toy Monte Carlo used to compute the sensitivity curves shown in Section 7.

6.5 Monte Carlo background samples

The simulation of the interactions of a 400 GeV proton beam with a thick target and the subsequent tracking of all the secondary products is extremely heavy CPU-wise. If a thick absorber made of high-Z material is considered, the yield can be as low as $5 \cdot 10^{-4}$ single muons above 10 GeV per proton, making a brute-force simulation quite inefficient.

In order to overcome this problem, a novel *biasing technique* has been developed within the NA62 collaboration [62] that allows one to reach up to three orders of magnitude increase in the simulation efficiency for the muon production in a 400 GeV/c proton beam-dump setup. At the same time, this method is maintaining nearly every feature of the original simulation from first principles. The method is comprehensively described in Ref [62] and is not repeated here. It is only important to mention here that the simulated samples obtained with the biasing technique have been extensively cross-checked against non-biased simulated samples and the agreement is excellent (see Ref. [62]).

The simulated background samples are described in the following. They are all generated with `BDSIM` package and passed to the full SHADOWS Monte Carlo. For each sample a GEANT4 threshold of 3 GeV is used.

- **sample (a):** $N_{\rm pot} \sim 1.3 \times 10^9$. It contains all the final products of the proton interactions with the dump apart the neutrinos to save disk space, for which a dedicated production has been performed (see sample c). No MIB included.
- **sample (a2):** $N_{\rm pot} \sim 1 \times 10^9$. As sample a) but with MIB included.
- **sample (b):** $N_{\rm pot} \sim 10^{12}$ generated with the biasing technique in order to study the muon background component, and optimising the MIB design. No neutrino component simulated.
- **sample (c):** $N_{\rm pot} \sim 10^8$ generated with neutrino component, in order to study the neutrino interactions with the material of the SHADOWS detectors. For this LoI we still did not perform a full MC study of neutrino inelastic interactions but we use the full MC to evaluate the rate of neutrinos in SHADOWS acceptance.

6.6 Background analysis

The proton interactions with the dump give rise to a copious direct production of short-lived resonances, and pions and kaons. While the TAX length ($\sim 22\,\lambda_{\rm I}$) is sufficient to absorb the hadrons and the electromagnetic radiation produced in the proton interactions, the decays of pions, kaons and short-lived resonances result in a large flux of muons and neutrinos. Muons and neutrinos emerging from the dump are the two major sources of background for FIP searches in SHADOWS and are described below. Neutrons can cause problems to electronic equipment, electromagnetic calorimeter response, and heavily contribute to the radiation dose. This component is currently being studied by the CERN radiation protection group along with possible ways to mitigate it.

6.6.1 Muon background

Muons originated in the dump can produce either combinatorial background and secondary tracks and V^0 through inelastic interactions in the last TAX interaction lengths or in the material encountered in the K12 front-end elements, and in the decay vessel material. Both backgrounds are described below.

- *Combinatorial muon background:* A dangerous source of background comes from random combinations of opposite charged muon tracks entering the decay vessel and mimicking signal events with dimuon final state by forming a fake vertex in the fiducial volume.

- *Muon inelastic interactions:* muons emerging from the TAXes can interact inelastically with the material upstream of or forming the decay volume. These interactions can generate particles, including V^0 (K_S, K_L and Λ), that enter the decay volume and mimic signal events.

The beam line and its magnetic elements

In order to understand the rate and the nature of the muon background in SHADOWS acceptance, it is convenient here to repeat the structure of the beam line and its magnetic elements around and after the TAX system.

As summarized in Section 3 and detailed in Ref. [63], the front end of the K12 beam consists of a strong quadrupole triplet followed by a dogleg, called 'achromat' of four identical dipoles. The first two dipoles provide a vertical offset of 110 mm and the last pair brings back the beam to the straight axis. Once back on the original axis, the beam is collimated and the momentum definition refined in another collimator, COLL3. After COLL3, a series of three 2 m long dipoles with the gap filled with soft iron, except for a 40 mm diameter field-free hole for the beam passage, sweeps away muons (both μ^+ and μ^-) produced in the region around the T10 target and TAX dumps. A schematic layout of the K12 beamline is shown in Figure 56.

When operated in beam dump mode the T10 target head is lifted up and the proton beam is dumped entirely on the TAXes. The configuration of the K12 beam line magnets used for studying the background hitting SHADOWS is the same configuration used for the standard NA62 operation in beam-dump mode studied by the Physics Beyond Colliders Conventional Beam Working Group (CBWG) for the operation of NA62 in dump mode [17] and [64] and successfully used during the 2021 dump data taking: The first two dipoles of the achromat surrounding the TAXes were set to the same field value (B = 1.82 T) and opposite polarity. The second pair of dipoles instead was put at the same polarity with the first dipole at the maximum field (1.82 T) and the second (BEND2 or B2) at 0.3 T.

Background components after BEND2 without MIB

Figure 57 shows the simulated momentum distribution of all the particles produced in the dump and scored immediately after BEND2 ($z = 34.4$ m with respect to the T10 target) for: i) any x, y (top plots); ii) $1.0 < x < 3.5$ m, $-1.0 < y < 1.5$ m (bottom plots) which define the transverse dimensions of the decay vessel.

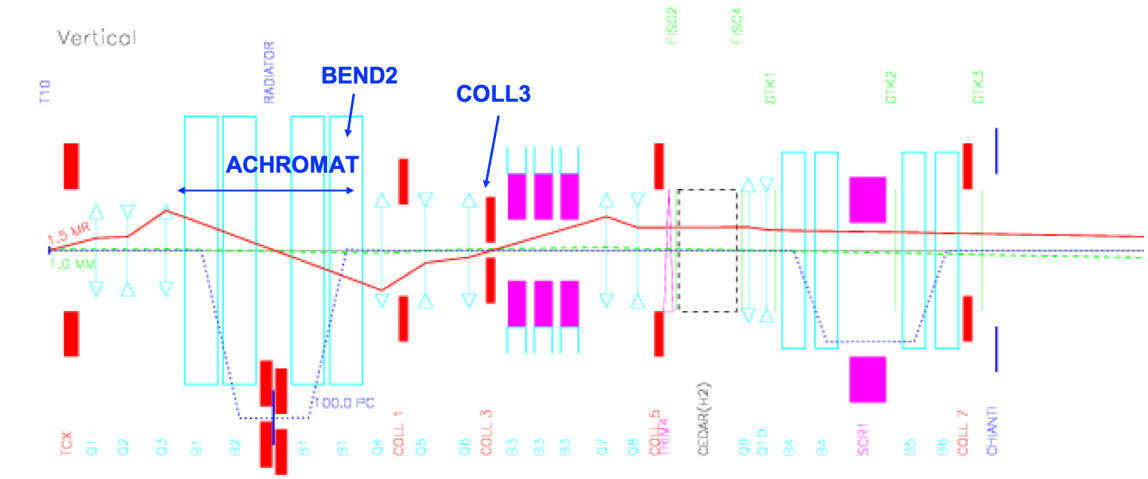

Figure 56. K12 beam line layout, with outlined the position of the Achromat, BEND2 (or B2) and COLL3.

The illumination of the non-muon component (excluding neutrinos that are simulated separately) and a zoom of its momentum distribution in the SHADOWS acceptance is shown in Figure 58.

As expected, most of the background (muon and non-muon component) is produced on-axis and misses the SHADOWS detector. The only relevant background emerging with a non-negligible p_T due to multiple scattering in the TAX material are low momentum (< 20 GeV) muons. The non-muon component (excluding the neutrino one) is instead fully negligible and made of very low momentum particles, mostly charged and neutral pions as we will see in Section 6.6.3.

These distributions are obtained from a sample of $1.3 \cdot 10^9$ pot (sample (a) described in Section 6.3), that has been produced without using the biasing technique, in order to have all the background components correctly normalised.

Muon flux without the MIB

A much larger muon background sample ($\sim 10^{12}$ pot, sample (b)) has been simulated with the biasing technique, in order to study the effect of the MIB system. Figure 59 shows the illumination of the muon component, at the level of the end of BEND2 either integrated over the two charges and each individual charge separately. Figure 60 shows again the muon distribution sampled at $z = 34.4$ m in the plane p versus x: for $|x| > 1000$ mm (region of interest for SHADOWS) the muons have $p < 20$ GeV. This observation is crucial for the design of the sweeping system described in Section 3.4, whose impact was shown in the same Section and detailed here below.

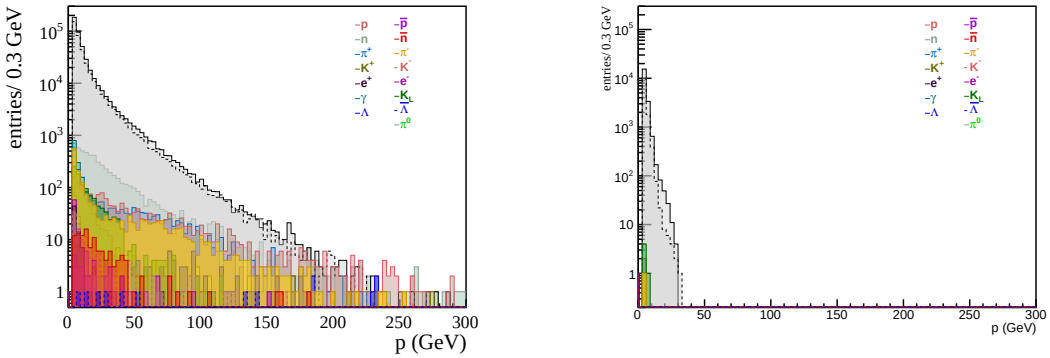

Figure 57. Left: Simulated momentum distribution of particles emerging from TAXes scored immediately upstream of the beginning of the decay vessel of the SHADOWS detector out of a sample of 1.3×10^9 pot. Right: Same as left plot but requiring that the particles are in SHADOWS acceptance ($1.0 < x < 3.5$ m and $-1.25 < y < 1.25$ m). The effect of the MIB is not included.

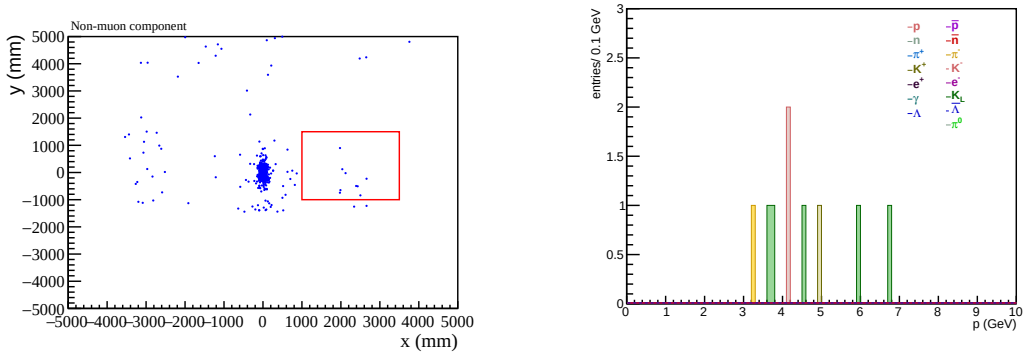

Figure 58. Left: Illumination at the plane z = 34.4 m of all the non-muon components (except neutrinos). The red box indicates the position of the SHADOWS decay volume. Right: momentum distribution of the non-muon component (except neutrinos). This is a zoom of the right plot of Figure 57. The effect of the MIB is not included.

Figure 61 shows the evolution of the same muon flux in absence of the MIB as a function of the distance from the dump in absence of the MIB system: i) $z = 35$ m (about the end of the second pair of dipoles of the achromat), ii) $z = 55$ m (roughly to the position of the first tracking station of the SHADOWS spectrometer); $z = 69.5$ m (roughly the position of the last SHADOWS muon station). The muon flux extends up to several meters with respect to the beam axis and hits all the active detectors of the SHADOWS spectrometer.

Taking into account the normalization factor coming from the comparison of the rates in data and in Monte Carlo (see Section 6.6.2), *in absence of the MIB system we expect a rate on the first tracking station of about 100 MHz, about equally distributed between the two muon charges.*

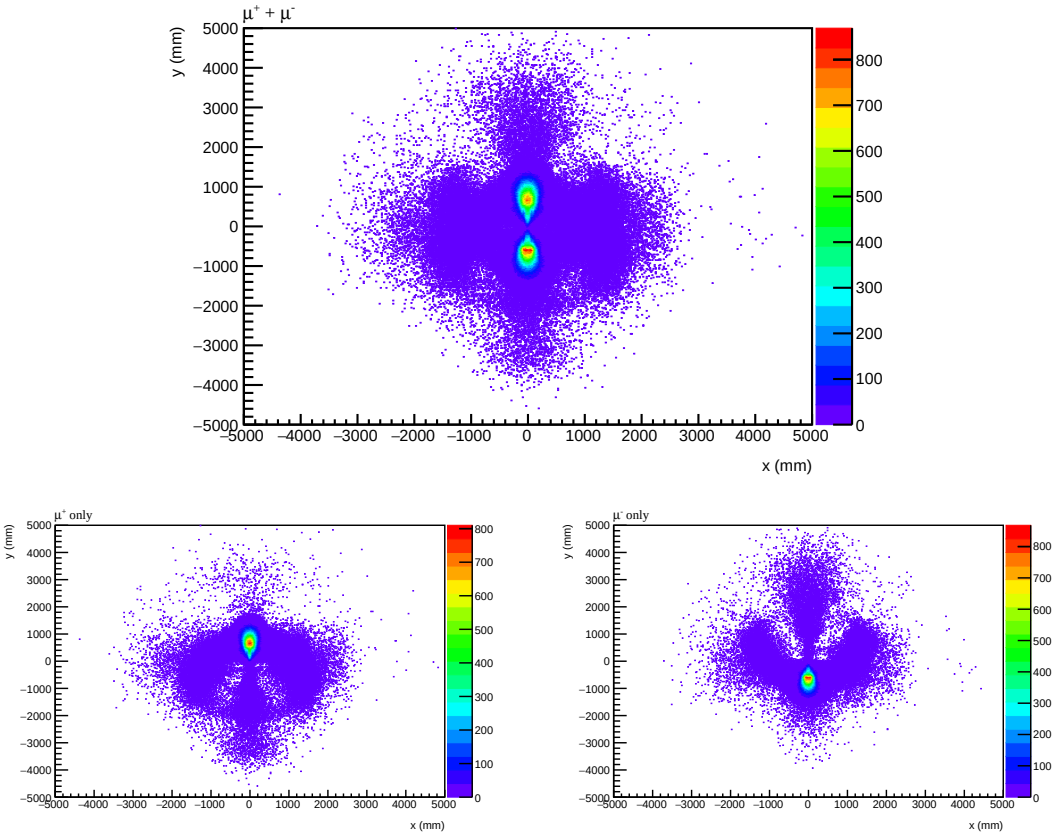

Figure 59. Top: Muon illumination at the plane corresponding to $z = 34.4$ m (beginning of the decay vessel). Bottom: same but divided per charge (left: positive muons, right: negative muons).

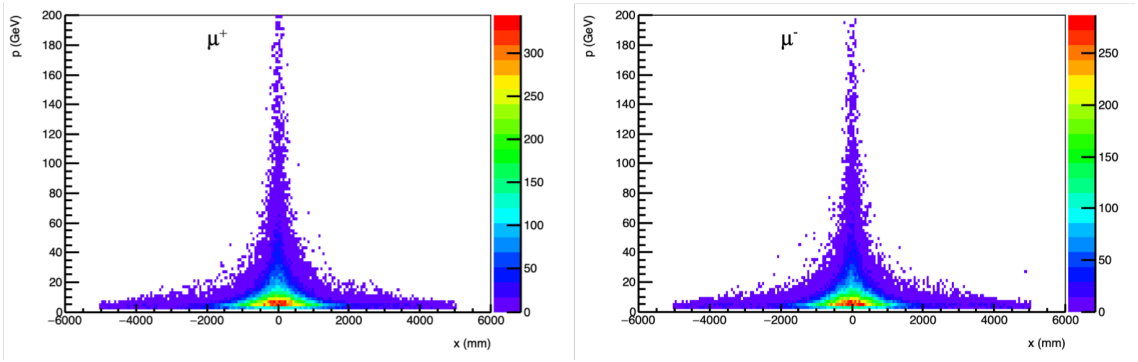

Figure 60. Muons at z=34.4 m in the plane momentum versus lateral displacement: muons with a lateral displacement of more than 100 cm have momentum below 20 GeV.

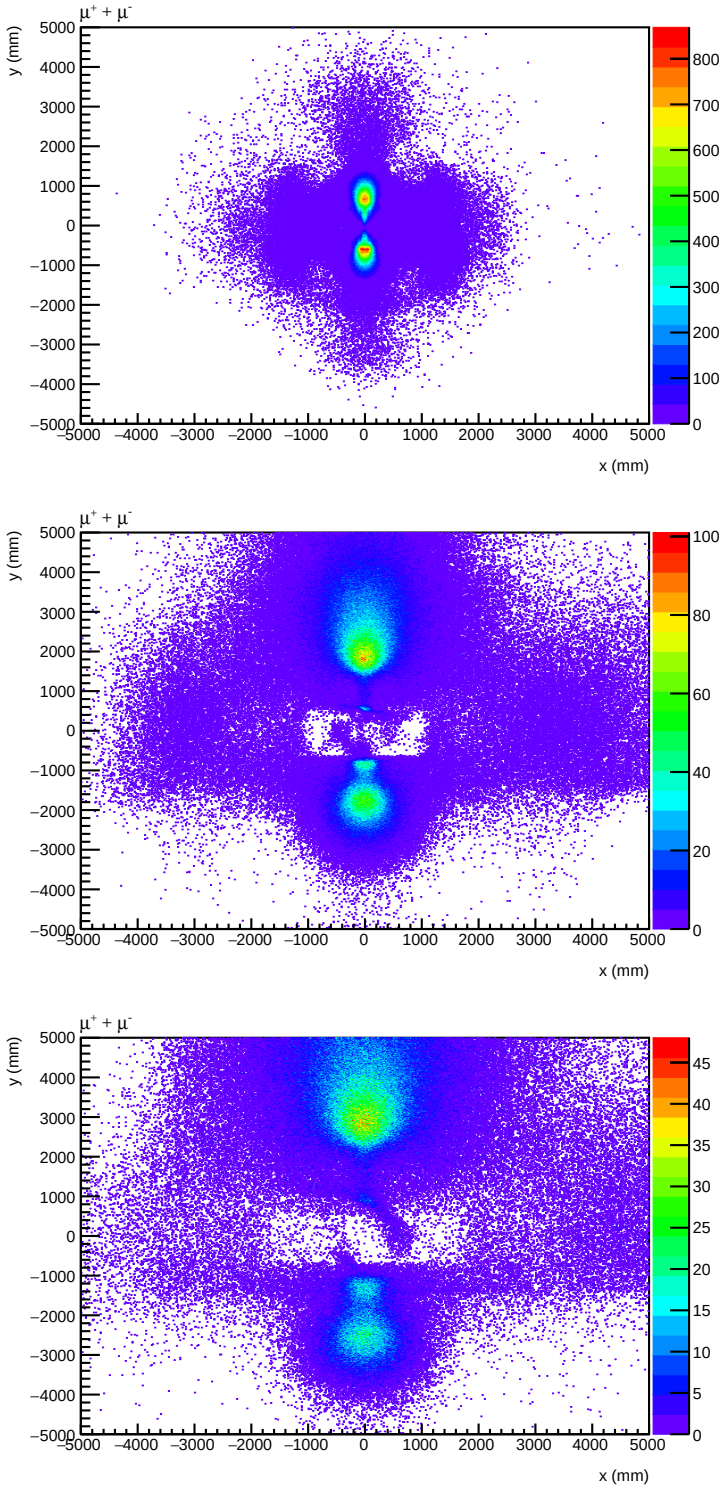

Figure 61. Evolution of the muon illumination emerging from TAXes. Top: illumination at the plane $z = 35$ m. Center: illumination at $z = 55.3$ m (first tracking station). Bottom: illumination at $z = 69.5$ m (position of the last muon station).

Background analysis in SHADOWS detector without MIB

The BDSIM output is handed over the SHADOWS full Monte Carlo where the particles emerging from the dump are let to interact with the SHADOWS detector material. The energy released in the active layers is then stored along with the position and the link with the GEANT4 particle that created the hit for further processing. The illumination of the Upstream Veto, the four STRAW chamber stations, and the four Muon stations is shown in Figure 62, 63, and 65, respectively. In the same Figures, the background composition is also shown along with its momentum and transverse momentum distributions. The sample used is 1.3×10^9 pot.

The analysis of the hit distributions and composition on the SHADOWS detectors without the impact of the MIB, can be summarised as follows:

1. The dominant background in the SHADOWS acceptance is the muon component being all the other components fully negligible (a separate discussion about neutrinos will be held in Section 6.6.4).

2. The residual muon component is made of low-p particles, well below 15 GeV.

3. The particle rate seen by the different sub-detectors decreases with the distance of the detector from the dump and is rather uniform for all the detectors apart the Upstream (or Muon) Veto that mirrors the illumination plot shown in Figure 59.

4. The rate seen by the first tracking chamber, without considering the MIB and taking into account the calibration factor between data and Monte Carlo as discussed in Section 6.6.2, is on average 100 MHz over the active area, but with a non-homogeneous distribution.

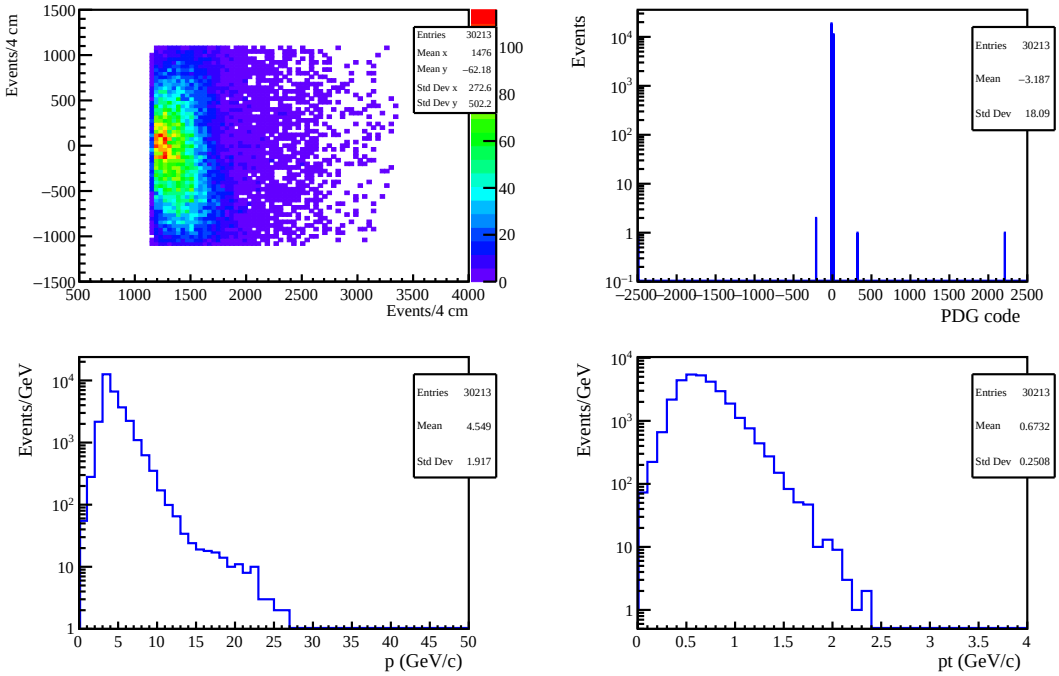

Figure 62. Upstream (or Muon) Veto background distributions corresponding to a sample of 1.3×10^9 pot: illumination (top right), GEANT4 particle code (top left), momentum distribution (bottom left) and transverse momentum distribution (bottom right). The MIB is not included.

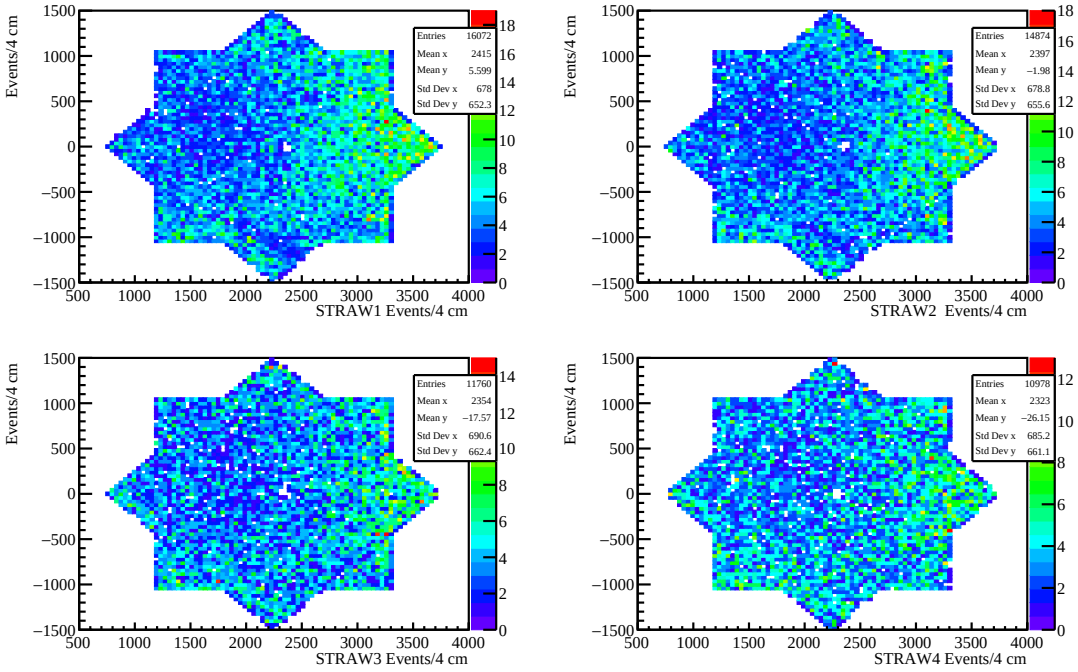

Figure 63. Illumination of the four tracking chambers corresponding to a sample of 1.3×10^9 pot. The MIB is not included.

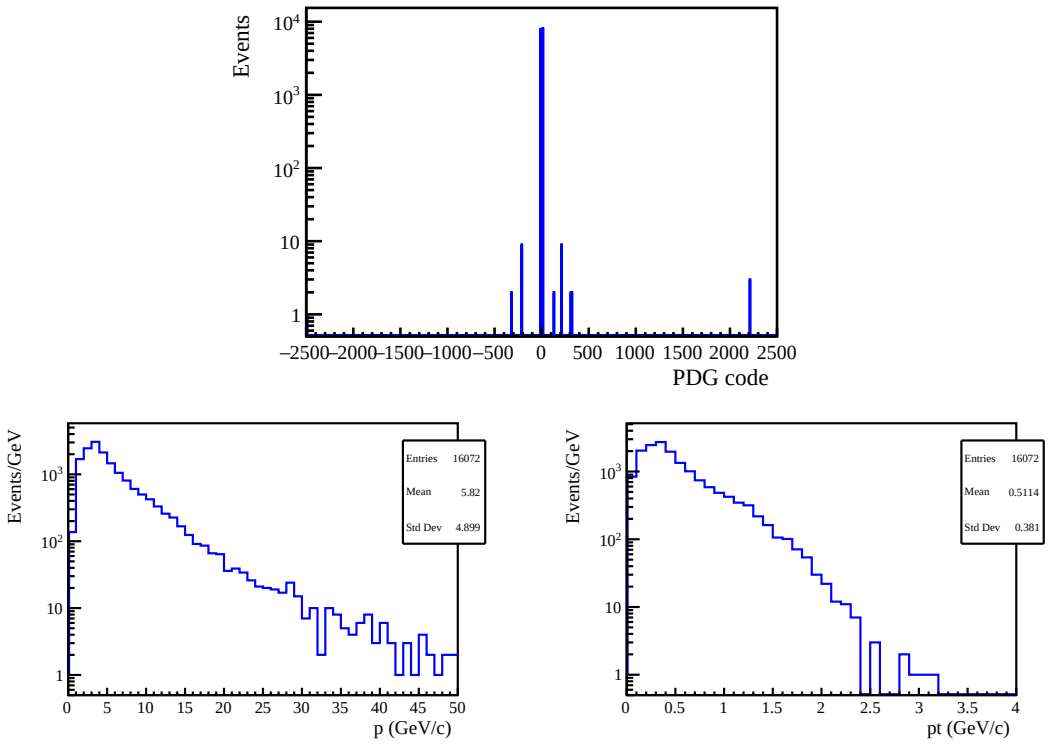

Figure 64. STRAW1 GEANT4 particle code population (top), momentum and transverse momentum distributions (bottom) of the background corresponding to a sample of 1.3×10^9 pot. The MIB is not included.

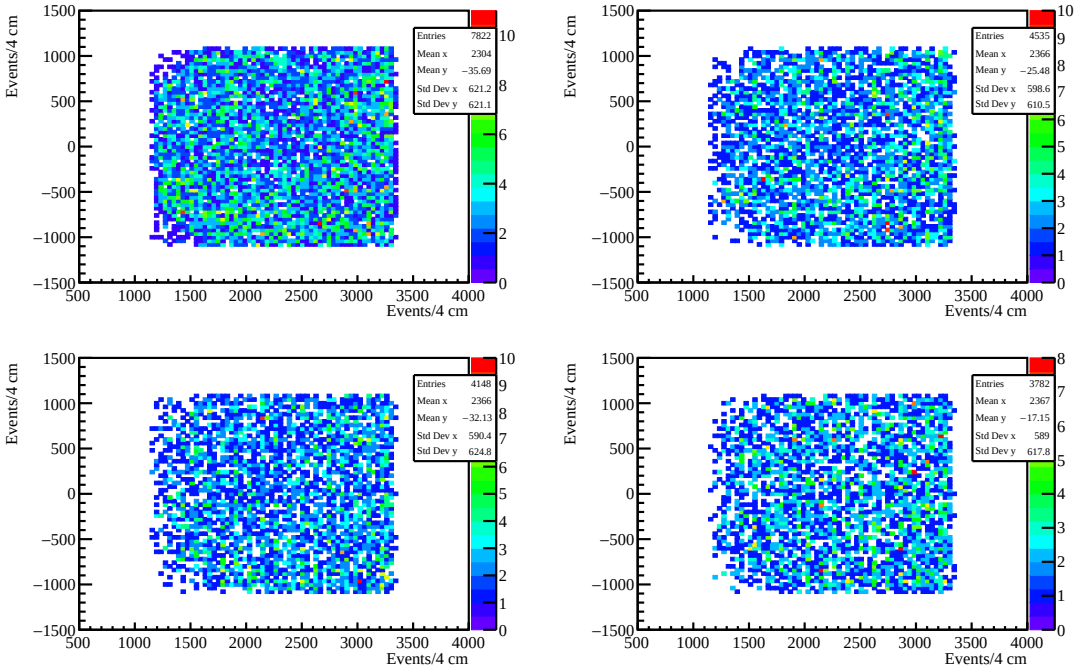

Figure 65. Illumination of the four muon stations corresponding to a sample of 1.3×10^9 pot. The MIB is not included.

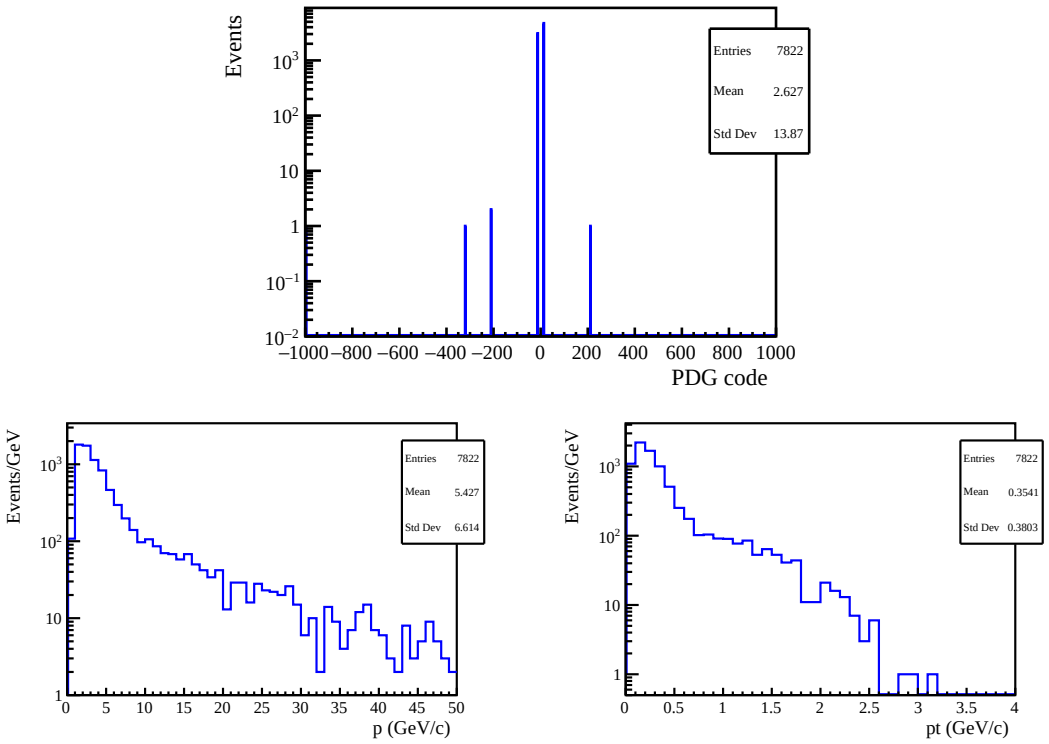

Figure 66. First muon station: GEANT4 particle code population (top), momentum and transverse momentum distributions (bottom) of the background corresponding to a sample of 1.3×10^9 pot. The MIB is not included.

Muon flux with the MIB

The MIB system has been extensively described in Section 3.4 and is not repeated here. However for reader's convenience we repeat the MIB layout in Figure 67.

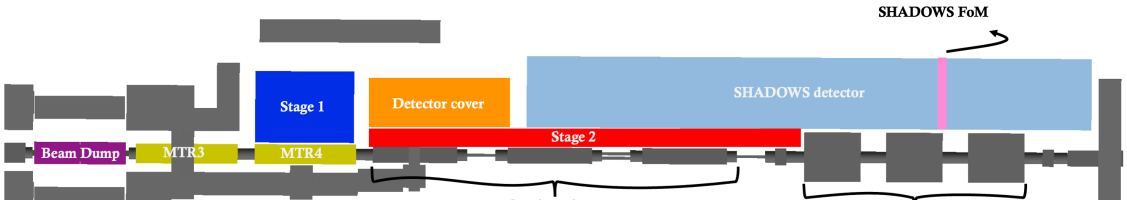

Figure 67. The optimised SHADOWS setup including the MIB system. The muons created in the beam dump (purple) are pushed off-axis by the MTR3 (B1) and MTR4 (B2) magnet (yellow) to reduce the muon background for HIKE in beam dump mode. The 3.5 m long Stage 1 magnet (blue) is placed right after MTR3, Stage 2 (red) is placed directly after Stage 1 to move the separated muons off-axis right away.

Figures 68 and 69 show the same evolution of the muon flux shown in Figure 61 in the presence of the MIB at different scoring planes along the beam direction, starting from the end of the dump (Figure 68, top plot) and ending at the level of the first muon station (Figure 69, bottom plot).

The flux evolution is separated by charge in order to better understand the behaviour of the sweeping system. The impact of the MIB system is dramatic. The impact of Stage 1 is evident in Figure 68. The muon flux that exits from the dump (Figure 68, top plot) is shaped by the first MTR-type dipole B1 of the achromat and enters in the Stage 1 (Figure 68, middle plot). The Stage 1 separates the two muon charges up and down (Figure 68, bottom plot) such that the second stage (Stage 2) becomes effective in pushing the two components outside the SHADOWS acceptance if they cross its magnetised area. The muon flux that instead crosses the iron block placed aside the Stage 2 (so called Detector Cover) is effectively absorbed and dies in the iron itself. The output of Stage 2 is shown in Figure 69 (top plot): the residual flux visible in output of the Stage 2 (red thin box) and absorbing iron (orange thick box) is made of low momentum particles with a large divergence that are dispersed before reaching the first SHADOWS tracking station (Figure 69, medium plot, red box) and even more the first muon station (Figure 69, bottom plot, red box). The flux is instead almost totally dispersed at the end of the SHADOWS detector, where the neutrino detector could be placed (see Section 8).

The momentum distribution of the residual muons at the level of the first SHADOWS tracking chamber as a function of the lateral displacement is shown in Figure 70: they are all very low$-p$ muons mostly populating the region of the detector closer to the cavern wall (as it is clear also from Figure 69, bottom plot). It is also clear from Figure 69, bottom plot, that the illumination is not the same for the positive and negative muon charge components, being the flux at this stage dominated by muons of positive charge.

Table 9 shows the overall muon reduction factor for the two charges together and for each charge separately: we see an overall reduction of the flux by a factor 120 bringing the overall muon rate in acceptance from 100 MHz to 0.8 MHz. The positive muons are reduced by a factor 110 and the negative ones by a factor 150. The overall rate drives the design of the detector rate capability: assuming that the 0.8 MHz are uniformly distributed over the active area of (250×250) cm^2, we have an average rate of about 10 Hz/cm^2. In reality we know that the illumination is not uniform, being the rate seen by the most illuminated regions of 20-30 Hz/cm^2.

Figures 71, 72, and 73 show in the top row the illumination of the Upstream Veto, the Timing detector and the first tracking chamber, respectively, with the MIB included corresponding. A sample of $\sim 10^{10}$ pot has been used to produce these plots. For comparison the same illumination without MIB (and corresponding to a sample 10 times less abundant, 10^9 pot) is shown in the same Figures. The bottom rows of the same Figures show the momentum distributions of the particles reaching a given sub-detectors, with and without the MIB included.

All these figures must be considered preliminary as we know that there are still margins of improvements, for example by magnetising also the detector cover adjacent to Stage 2. These (and other) improvements will be studied for the Proposal.

Table 9. Muon flux rate in SHADOWS acceptance without and with the MIB for the two muon charges together and for each charge separately.

	$\mu^+ + \mu^-$	μ^+	μ^-
rate before MIB	100 MHz	50 MHz	50 MHz
MIB reduction factor	~ 120	~ 110	~ 150
rate after MIB	0.8 MHz	0.5 MHz	0.3 MHz

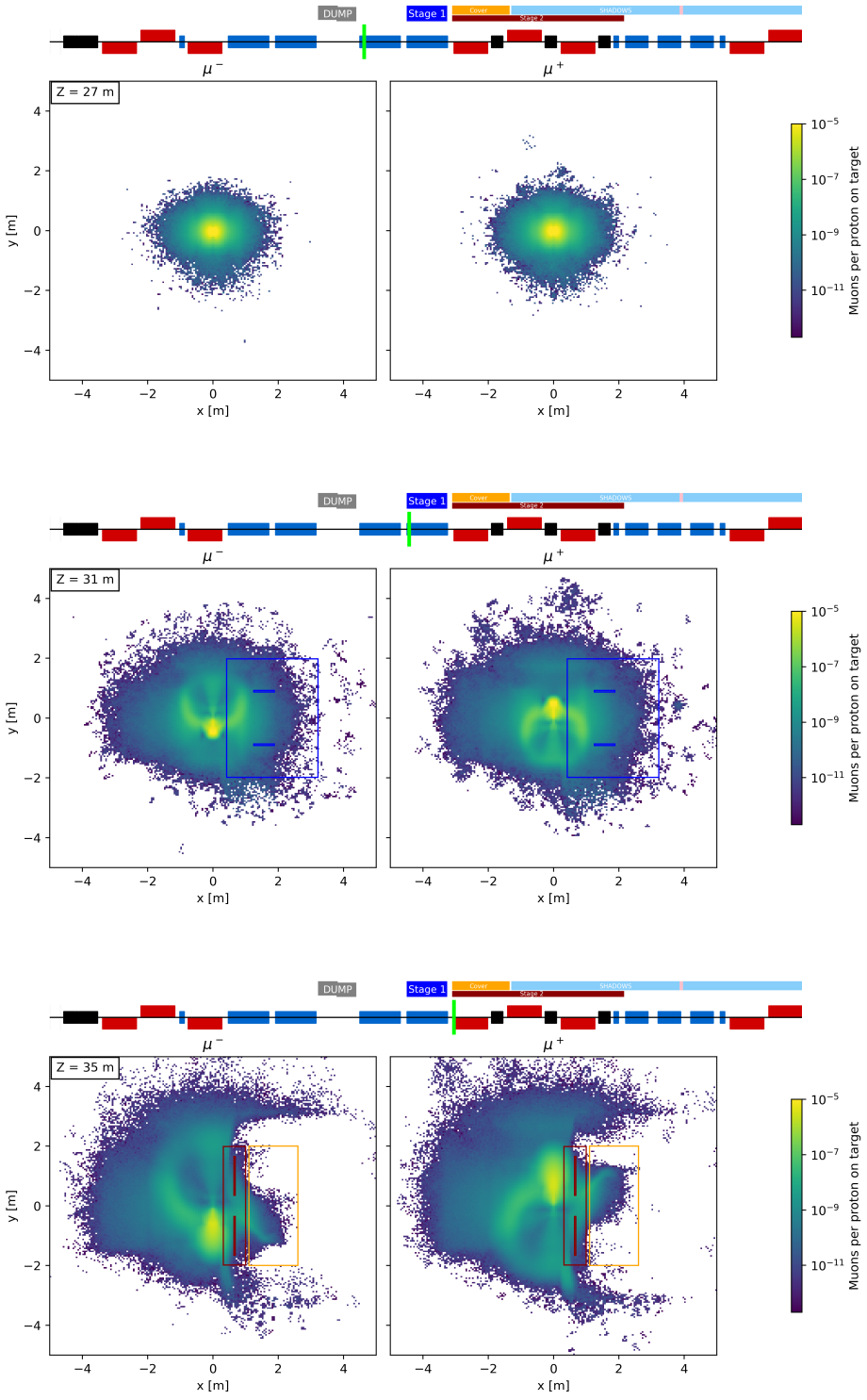

Figure 68. Evolution of the muon illumination from the dump exit to the end of the first Stage (Stage 1) of the MIB system. From top to bottom: illumination at the end of the dump; illumination before Stage1; illumination after Stage1. The scoring plane is defined by the position of the light green bar in the layout on top of each plot. See text for the detailed description of the muon flux evolution.

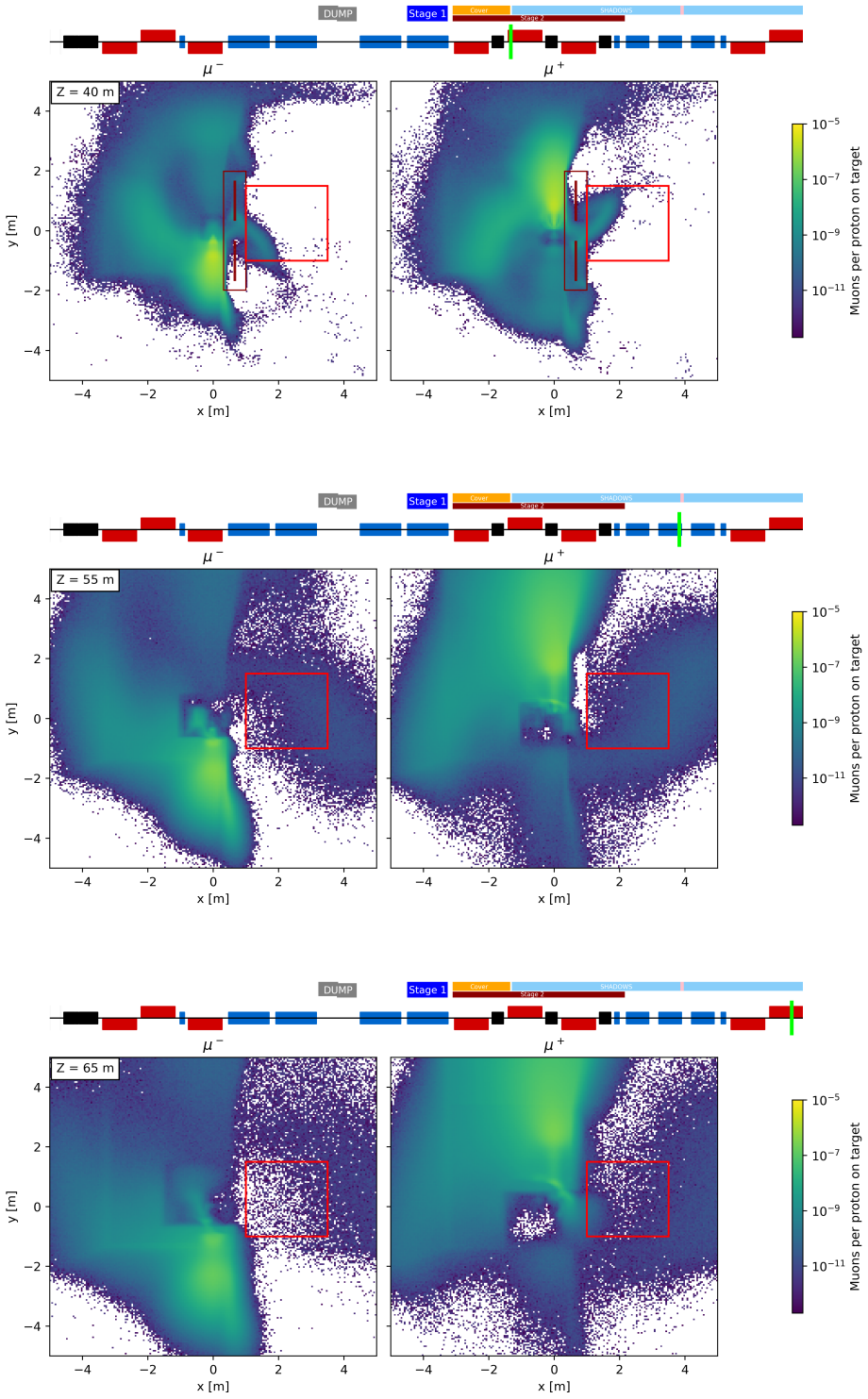

Figure 69. Evolution of the muon illumination from the dump exit to the end of the first Stage (Stage 1) of the MIB system. From top to bottom: illumination at the end of Stage2; illumination in front of the first tracking chamber; illumination at the first muon station. The scoring plane is defined by the position of the light green bar in the layout on top of each plot. The red square box is the SHADOWS acceptance. See text for detailed description of the muon flux evolution.

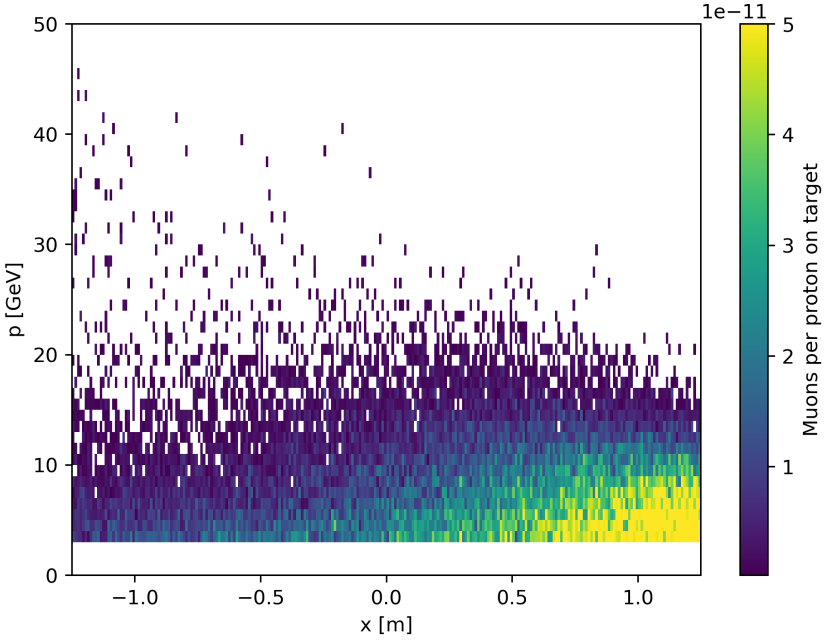

Figure 70. Momentum distribution of the residual muons at the level of the first SHADOWS tracking chamber as a function of the lateral displacement. The residual background is made of low momentum muons that populate mostly the region of the station closer to the cavern wall. The $x = 0$ m coordinate here corresponds to the detector centre.

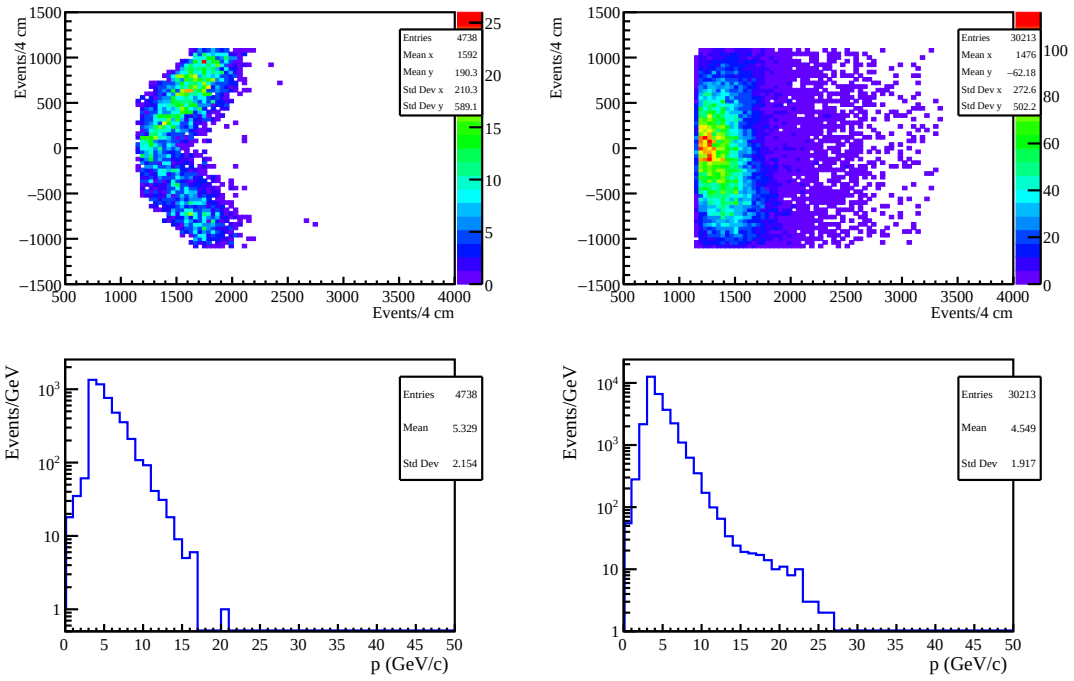

Figure 71. Illumination (top) and momentum distributions (bottom) of the Upstream Veto with (left) and without (right) the MIB. The illumination with the MIB correspond to about 10^{10} pot, the one without MIB to about 10^9 pot (hence: the entries of the left plots should be decreased by a factor 10 to be compared to the right plots).

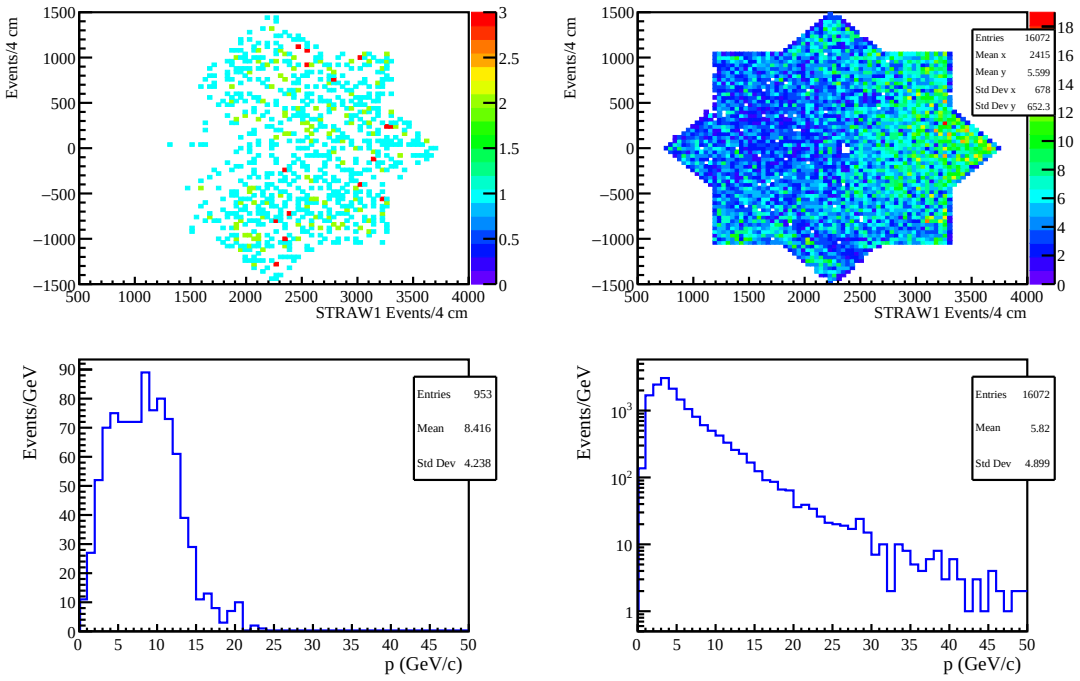

Figure 72. Illumination (top) and momentum distributions (bottom) of the first tracking chamber with (left) and without (right) the MIB. The illumination with the MIB correspond to about 10^{10} pot, the one without MIB to about 10^9 pot (hence: the entries of the left plots should be decreased by a factor 10 to be compared to the right plots).

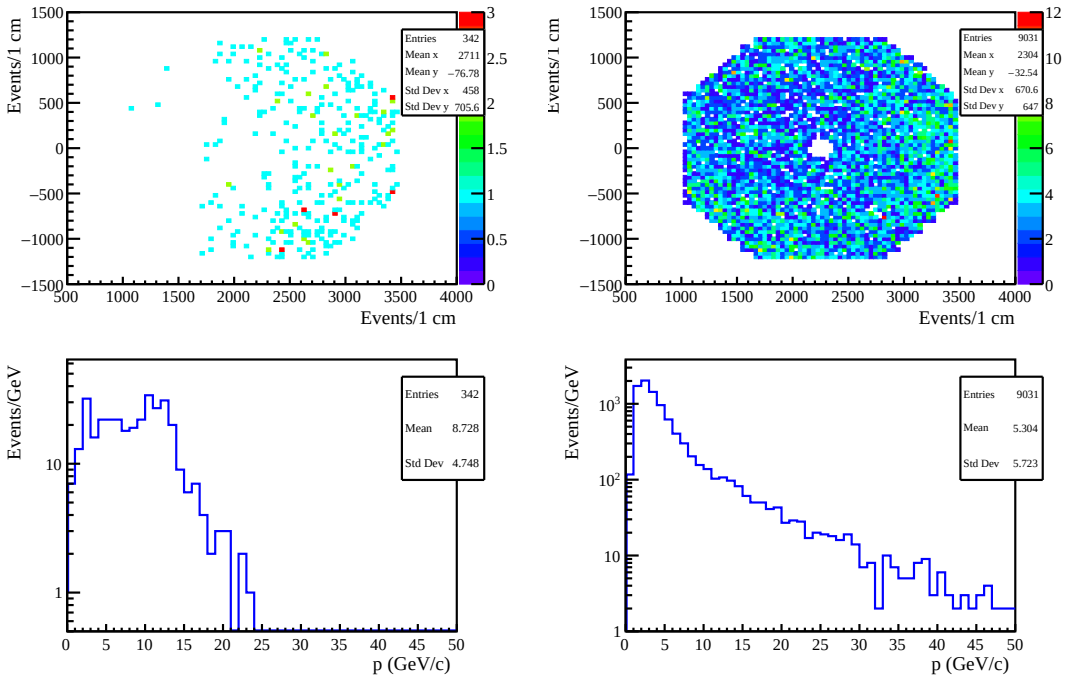

Figure 73. Illumination (top) and momentum distributions (bottom) of the Timing Detector with (left) and without (right) the MIB. The illumination with the MIB correspond to about 10^{10} pot, the one without MIB to about 10^9 pot (hence: the entries of the left plots should be decreased by a factor 10 to be compared to the right plots).

6.6.2 Validation with data of the beam-induced muon background

The results of the `BDSIM` Monte Carlo have been compared against the data collected by NA62 in October 2021, when the experiment was successfully operated in beam-dump mode for about 1 week at about 150% the nominal NA62 beam intensity. In this period NA62 collected about $1.5 \cdot 10^{17}$ pot with the magnet settings proposed by the CBWG [19].

Figure 74 shows a schematic layout of the NA62 experiment [31]. A very condensed description of the experiment is provided here below.

NA62 Detector

A differential Cherenkov counter (KTAG)tags incoming kaons with a 70 ps time resolution. Four silicon pixel stations (GTK) located before, between and after two pairs of dipole magnets (beam achromat), form a spectrometer to measure momentum, direction and time of beam particles with 0.15 GeV/c, 16 μrad and 100 ps resolutions. A magnetic spectrometer (STRAW, comprising two pairs of straw chambers on either side of a dipole magnet) measures the momentum-vector of the outgoing particle with a momentum resolution σ_p/p in the 0.3–0.4% range. A ring-imaging Cherenkov counter (RICH, filled with neon at atmospheric pressure) tags the decay particle with a precision better than 100 ps and provides particle identification.

Two scintillator hodoscopes (CHOD), (one made of a matrix of tiles read out by SiPMs and the other composed of two orthogonal planes of slabs, reused from the NA48 experiment) are used for triggering and timing purposes, providing a 99% efficient trigger and a time measurement with 200 ps resolution for charged particles. The third GTK station (GTK3) is immediately preceded by a final collimator to partly block particles produced in upstream decays, and marks the beginning of a 117 m-long vacuum tank. A scintillating tiles based hodoscope (ANTI-0) placed in front of the decay vessel, tags early decays of kaons and pions and beam-induced muon background emerging from TAX and beam line magnetic elements. The first 80 m of the tank define a fiducial volume (FV) in which 13% of the kaons decay.

Other sub-detectors are used as vetoes to suppress decays into photons or multiple charged particles (electrons, pions or muons) or as complementary particle-identifiers. Six stations of plastic scintillator bars (CHANTI) detect with 99% efficiency and 1 ns time resolution extra activity including inelastic interactions in GTK. Twelve stations of ring-shaped electromagnetic calorimeters (LAV1 to LAV12, made of lead-glass blocks) surround the vacuum tank and the detector to achieve hermetic acceptance for photons emitted in K^+ decays in the FV at polar angles between 10 and 50 mrad. A 27 radiation length thick quasi-homogeneous liquid krypton electromagnetic calorimeter (LKr) detects photons from K^+ decays emitted at angles between 1 and 10 mrad and complements the RICH for particle identification. The LKr energy, spatial and time resolutions in NA62 conditions are $\sigma_E/E = 1.4\%$ at an energy deposit of 25 GeV, 1 mm and between 0.5 and 1 ns, respectively, depending on the amount and type of energy release. Two hadronic iron/scintillator-strip sampling calorimeters (MUV1,2) and an array of scintillator tiles located behind 80 cm of iron (MUV3, with 400 ps time resolution) supplement the pion/muon identification

system. A lead/scintillator shashlik calorimeter (IRC) located in front of the LKr, covering an annular region between 65 and 135 mm from the Z axis, and a similar detector (SAC) placed on the Z axis at the downstream end of the apparatus ensure the detection of photons down to zero degrees in the forward direction. Additional counters (MUV0, HASC) installed at optimized locations provide hermetic coverage for charged particles produced in multi-track kaon decays.

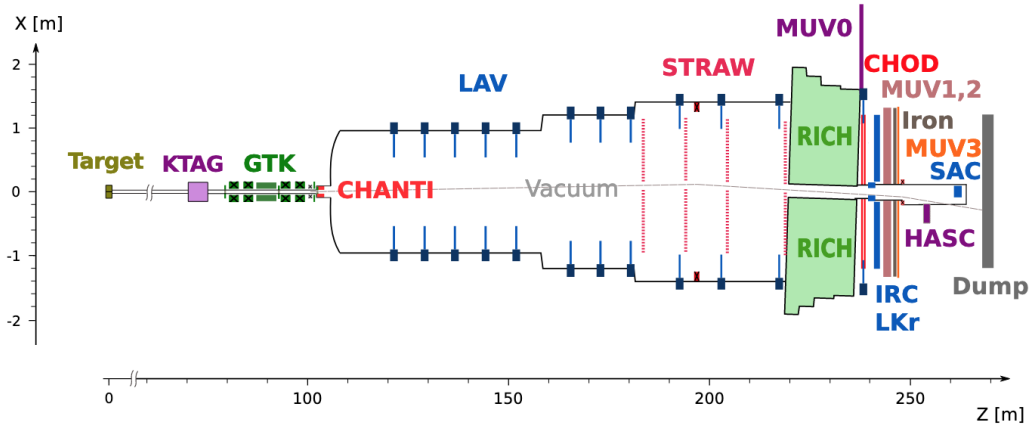

Figure 74. Schematic top view of the NA62 experiment.

Analysis of the data collected in dump mode

The data in dump were recorded by NA62 using the following trigger configurations: i) >=1 cluster in the LKr calorimeter with total energy above 1 GeV; ii) one hit in newCHOD detector (this line had a downscale factor of 20); iii) two hits in time in one of the two charged hodoscopes. Rescaled at the nominal NA62 intensity of 33×10^{11} protons-per-pulse (ppp) for a nominal spill duration of 4.8 sec, NA62 measured 1.8, 8, and 9 kHz for the three trigger lines, respectively. In addition to the normal triggered events, NA62 is able to store the raw information of the number of hits per spill hitting a given channel, the so called "End of Burst" (EoB) events. This information is quite useful in order to study possible biases introduced by the trigger lines on the recorded data.

Figure 75 shows in the upper plots the ANTI-0 illumination for a single burst (n.700) of the run (n. 11092), corresponding to $N_{\rm pot} = 62 \times 10^{11}$ pot: The left plot shows the illumination using the EoB events and the right plot the one using the events triggered by the downstream spectrometer. The EoB data are about 100 more abundant than the triggered data, as a consequence of the NA62 geometry: NA62 measures $\sim 4.5 \times 10^{-6}$ hits/pot with the EoB counters of the ANTI-0 at the beginning of the fiducial volume, and $\sim 5.6 \times 10^{-8}$ hits/pot for data triggered with the charged hodoscopes at the end of the decay volume, about 180 m downstream with respect to the ANTI-0 position. The same Figure shows in the bottom plot the ANTI-0 illumination obtained with simulated events corresponding to $\sim 10^9$ pot with $E_{\rm thr} = 3$ GeV.

The projections of the ANTI-0 illumination in the x and y dimensions are shown in Figure 76, where the three samples (data EoB, data triggered, and simulation) have been normalised to the same number of entries.

The agreement in shape between the three samples is within 20-30%, which is remarkable given the fact that at this stage we are considering only raw hits.

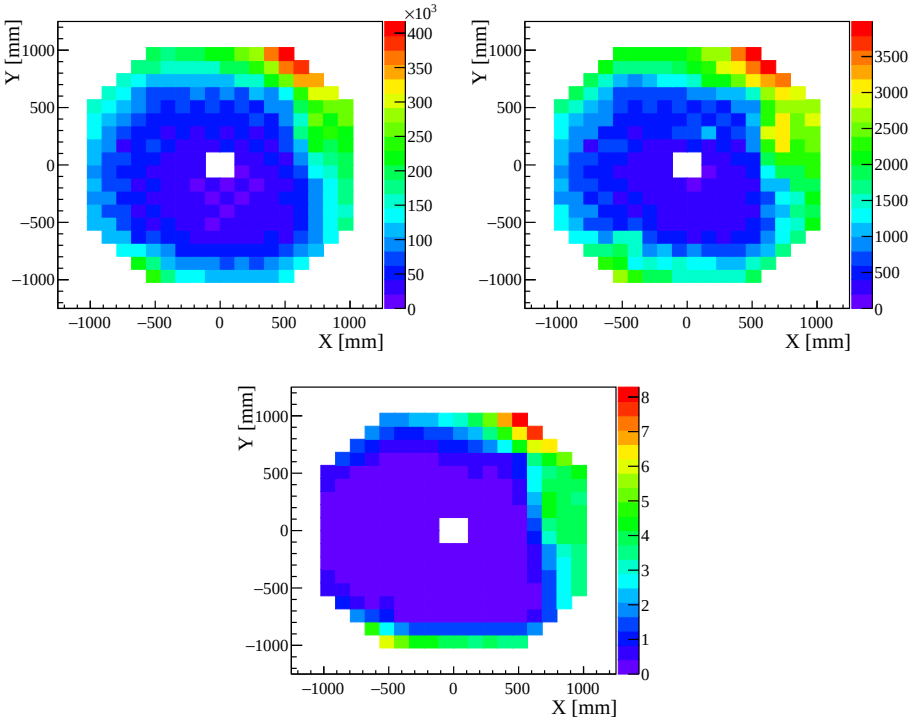

Figure 75. Anti-0 illumination for burst 700 of run 11092 for EoB data (upper left) and triggered events (upper right) and simulation (bottom).

A more thorough validation of the Monte Carlo simulation is obtained by comparing momentum ad transverse momentum distributions of reconstructed muon tracks in the NA62 spectrometer, both for data and simulation. To both samples a threshold of $p > 3$ GeV has been applied.

The momentum and transverse momentum distributions for data and MC are shown in Figure 77 where the distributions are normalised to the same number of entries. The agreement in terms of shape is relatively good. In terms of absolute rates we observe a difference of a factor of three between data and Monte Carlo: $\sim 3.5 \times 10^{-9}$ muons/pot in data against $\sim 1.2 \times 10^{-9}$ muons/pot in the simulation. This difference was already observed in other studies performed by the NA62 collaboration [62] and is taken into account when evaluating the rates in SHADOWS acceptance.

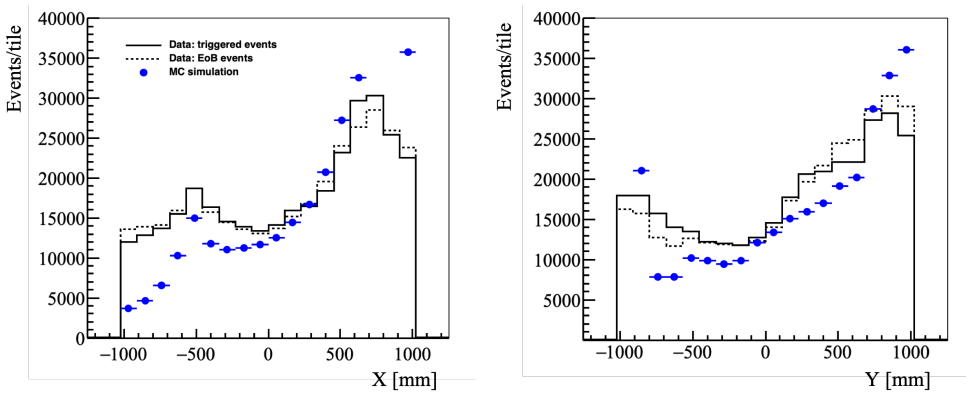

Figure 76. ANTI-0 hit illumination for a single spill of a run taken in dump mode in October 2021: $x-$ projection (left) and $y-$projection (right).

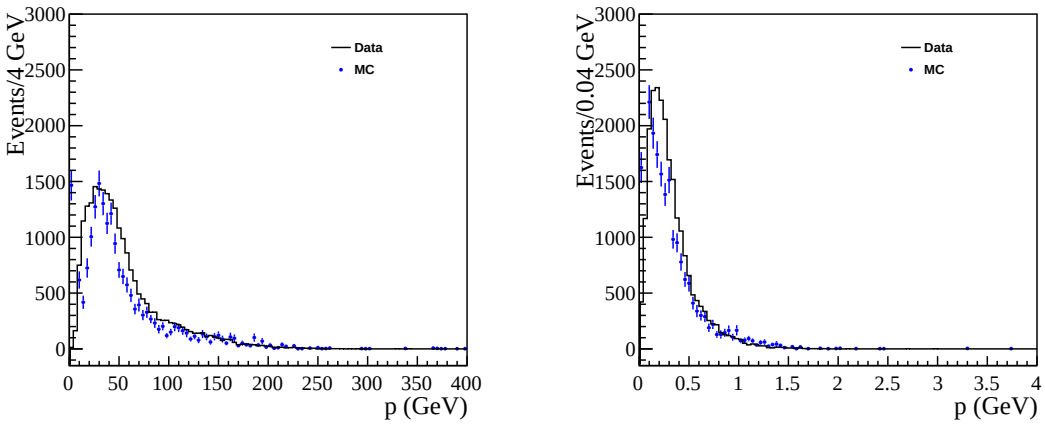

Figure 77. Momentum and transverse momentum distribution of reconstructed tracks with $p >$ 3 GeV in the NA62 acceptance for data (solid black line) and Monte Carlo (blue dots).

6.6.3 Analysis of the residual muon background

The new MIB design has a rejection factor of ~ 120 when integrated on both charges, that determines the residual flux in acceptance of 0.8 MHz of muons of both charges ($f_+ = 0.5$ MHz of μ^+ and $f_- = 0.3$ MHz of μ^-). Now let's see how we can reduce it. The computation of the combinatorial background is performed on a spill by spill basis and the outcome multiplied by $\sim 3 \cdot 10^6$ spills expected to be collected by SHADOWS in its full lifetime. For this computation the simulated sample of $\sim 10^{12}$ pot has been used (sample b).

1. **Timing detector:** This is the most efficient way of reducing combinatorial muon background. We require that the muon pairs with $f_+ \sim 0.5$ MHz and $f_- \sim 0.3$ MHz rate are in a time window of $\delta T = \pm 3\sigma_t$, where $\sigma_t \sim 100$ ps is the assumed time resolution of the timing layer, hence $\delta T = 600$ ps. The rate of accidentals in this case is:

   $$R_{\rm acc} = N_{\rm acc}/sec = \delta T \times f_+ \times f_- = 0.6 \cdot 10^{-9}{\rm s} \times 0.5 \cdot 10^{6}{\rm s}^{-1} \times 0.3 \cdot 10^{6}{\rm s}^{-1} \sim 100/{\rm s}$$

   Hence: $N_{\mu\mu}(\text{timing}) \sim$ *480 accidental pairs per 4.8 sec long spill.*

2. **Upstream Veto:** We plan to build a double layer of MicroMegas at the beginning of the decay volume. This detector can have an efficiency of 99.9 %. We assume conservatively to have an efficiency of 99.5 %. The probability of not-vetoing two muon tracks emerging from the dump is therefore $(1-\varepsilon)^2 = (0.5 \cdot 10^{-2})^2 = 2.5 \cdot 10^{-5}$.

   Hence: $N_{\mu\mu}(\text{timing, UV}) = 480 \times 2.5 \cdot 10^{-5} = 1.2 \cdot 10^{-2}$*/spill.*

3. **Vertex reconstruction in the FV:** Since the reconstruction package is still not available we compute the distance of closest approach (CDA) of two muons of opposite charge within the SHADOWS decay volume. The CDA distributions for a signal (ALP $\rightarrow \mu^+\mu^-$) and for the combinatorial muon background are shown in Figure 78 separately and together. The distribution of the CDA for all muon pairs of opposite charge with $p > 3$ GeV having the CDA in the SHADOWS decay volume is shown in Figure 78.

   Based on this distribution, the probability of having a CDA < 10 mm is:

   $$P(\text{CDA} < 10 \text{ mm}) = 2 \cdot 10^{-3}.$$

   Hence: $N_{\mu\mu}(\text{timing, UV, CDA}) = 1.2 \cdot 10^{-2}$*/spill* $\times 2 \cdot 10^{-3} \sim 2.4 \cdot 10^{-5}$*/spill.*

4. **Pointing:**
   Once formed a vertex the total momentum of the two muons, extrapolated backwards to the dump, should point to the impinging point of the proton beam. In fact the heavy quarks are produced in hard-scatterings in the first 1-2 interaction lengths in

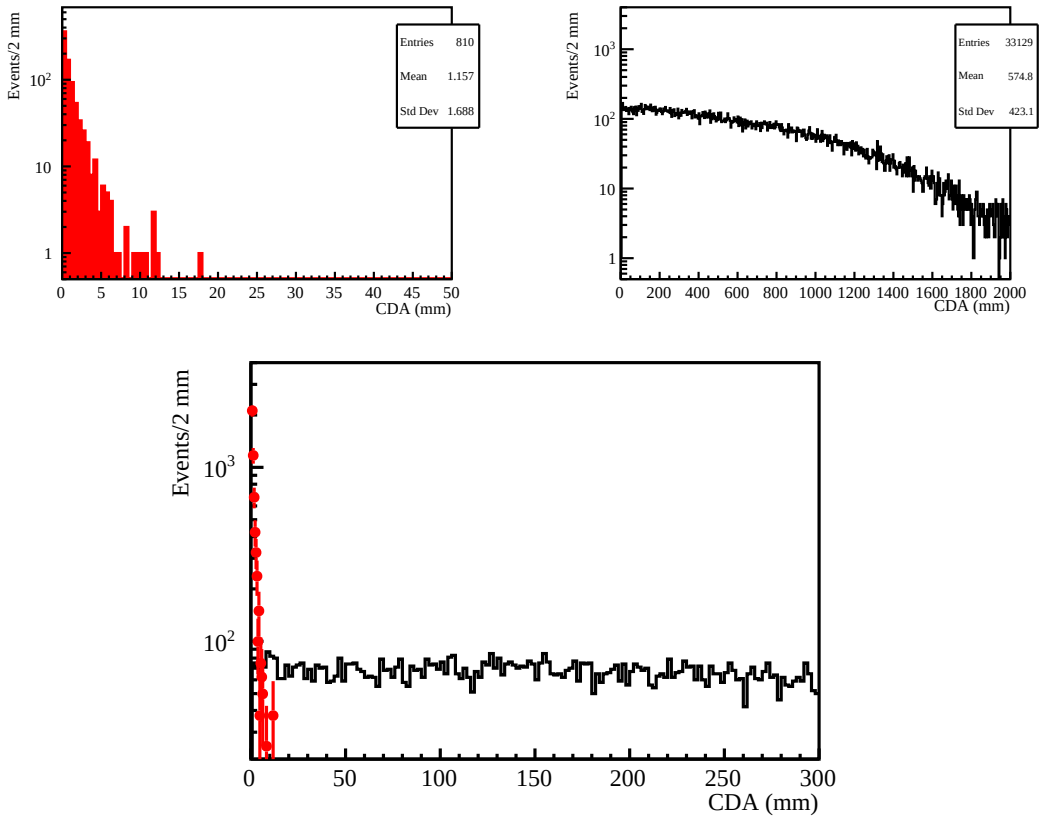

Figure 78. Distribution of the distance of closest approach (CDA) of two muon tracks of opposite charge for signal (ALP$\rightarrow \mu^+\mu^-$, top left) and combinatorial background (top, right) within the SHADOWS decay volume. The bottom plot show the two distributions superimposed.

the dump and a pointing requirement can be issued. The distribution of the impact parameter (IP) of the total momentum for signal (ALP $\rightarrow \mu^+\mu^-$) and combinatorial dimuon pairs with respect to the impinging point of the proton beam is shown in Figure 79, for signal (top, left), background (top,right) and together (bottom) respectively.

A requirement of having $IP < 3$ cm gives an efficiency of:

$$P(IP < 30 \text{ mm}) = 1 \cdot 10^{-2}$$

Hence: $N_{\mu\mu}(\text{timing}, \text{UV}, \text{CDA}, \text{IP}) = 2.4 \cdot 10^{-5}/spill \times 1 \cdot 10^{-2} = 2.4 \cdot 10^{-7}/spill.$

All the requirements applied above are highly efficient for signals decaying in 2-muon final states if the kinematic is closed, eg: if it is 2-body decay. HNLs can present a case where this is not true, the $\mu^+\mu^-\nu$ final state.

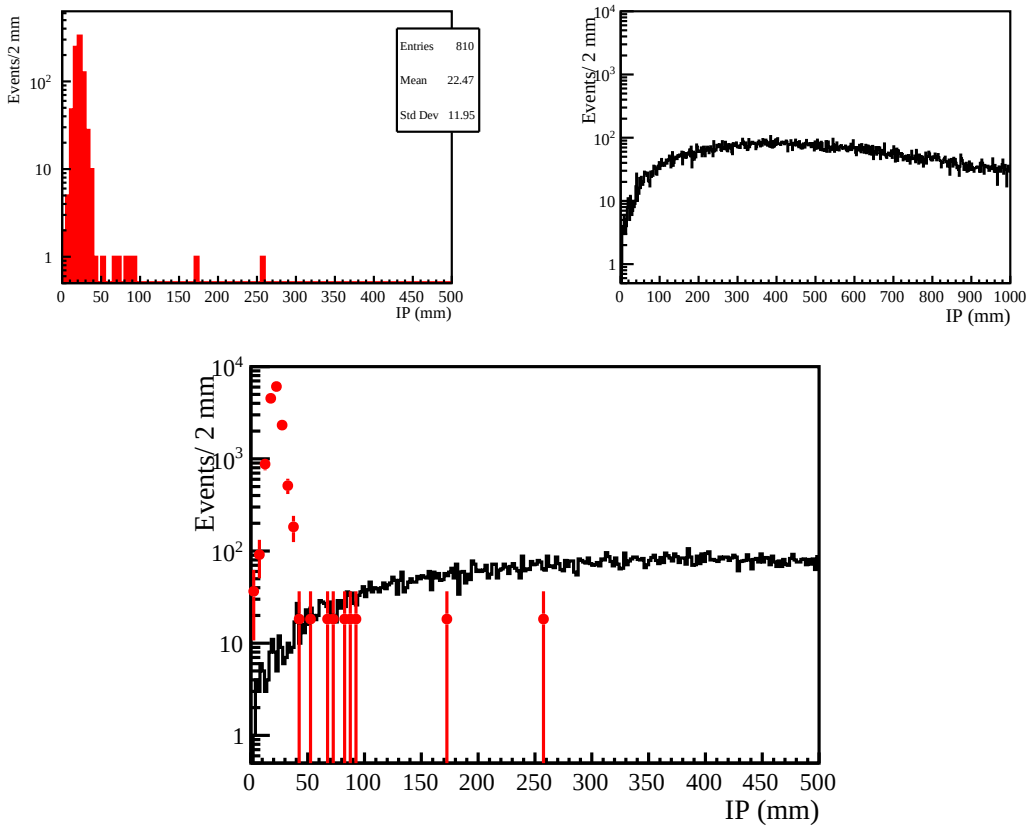

Figure 79. Distribution of the impact parameter (IP) with respect to the proton beam impining point on the dump of two muon tracks of opposite charge for signal (ALP$\rightarrow \mu^+\mu^-$, top left) and combinatorial background (top, right). The bottom plot show the two distributions superimposed.

In this case the pointing requirement should be relaxed. But this is the only possible case among tens of possible HNL final states. Moreover all the other benchmarks (ALPs, Dark Scalars, Asymmetric DM, etc.) do not have this problem.

Table 10 summarises the numbers found so far. *Given an average of* 2.4×10^{-7} *dimuon events/spill and* $3{\cdot}10^6$ *spills in all the SHADOWS lifetime, we have about 0.7 combinatorial di-muon background events in* $5 \cdot 10^{19}$ *pot.*

Table 10. Number of dimuon events per spill as a function of the requirement. This assumes to have initially 0.5 MHz of negative muons and 0.3 MHz of positive muons over 4.8-sec spill length hitting the SHADOWS acceptance.

$N_{\mu\mu}$/spill	requirement
480	timing (T)
$1.2 \cdot 10^{-2}$	UV
$2.4 \cdot 10^{-5}$	CDA<10 mm
$2.4 \cdot 10^{-7}$	IP<30 mm
$N_{\mu\mu}/5 \cdot 10^{19}$ pot	
0.7 events	T & UV & CDA & IP

Muon inelastic interactions with the dump, the MIB and the beamline material

The residual background due to the muon inelastic interactions with the dump, the MIB and the beamline material has been studied by using $\sim 10^9$ pot with the MIB included (sample a2). The effect of the MIB is to absorb the low-p pions and protons shown in Figure 58 (right) while absorbing most of the residual muon flux that crosses it (and therefore preventing it to make further inelastic interactions). This effect is shown in Figure 80 where the illumination of the non-muon background component (excluding neutrinos) in front of the decay vessel is shown without (left) and with (right) the MIB included. No event is observed out of a sample of 10^9 pot.

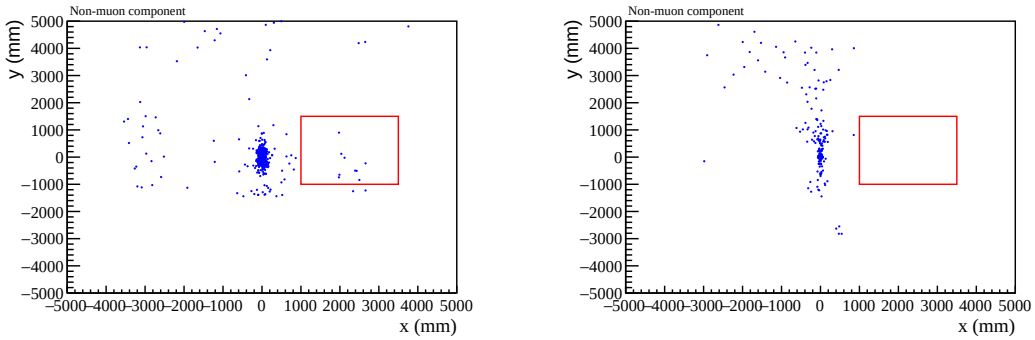

Figure 80. Illumination due to the non-muon background component (excluding neutrinos) in front of the decay vessel without (left) and with (right) the MIB.

6.6.4 Neutrino background

Neutrinos emerging from a proton beam dump can make inelastic interactions with the beam line and detector material and with the gas inside the decay volume. They are mostly produced by the decay of light mesons, pions and kaons, being those produced via charm decays account only a small fraction of the total yield. However, as in the case of the muon background, for an off-axis setup they are of a much less concern with respect to an on-axis one, because they are mostly produced in the forward direction and miss SHADOWS acceptance.

Neutrinos are produced using the same simulation package used for muons, the GEANT4-based `BDSIM` code. The results are based on a sample of about 10^8 pot, with a GEANT threshold of $E_{\rm thr} = 3$ GeV. The distribution of neutrinos in front of the first SHADOWS tracking chamber is shown in Figure 81 (top plot), along with their momentum distributions in the full solid angle (bottom, left) and in SHADOWS acceptance (bottom right). From simulation we have about 6.8×10^{10} ν's and $\overline{\nu}$'s per 2×10^{13} pot spill, fully dominated by muon neutrinos (the fractions are: 2.2 % ν_e, 1.8% $\overline{\nu}_e$, 58% ν_μ and 38% $\overline{\nu}_\mu$). Only 7% of the overall neutrino flux enters the SHADOWS decay volume, hence $\sim 5 \times 10^9 (\nu + \overline{\nu})$ per spill or 1.5×10^{16} $(\nu + \overline{\nu})$ per 3×10^6 spills expected in the SHADOWS lifetime.

The probability of inelastic interactions over 20 m of decay volume filled with air at atmospheric pressure for neutrinos with an average energy $E \sim 5$ GeV is $P_{\rm (inel.\ int.)} \sim 2 \times 10^{-15}$. Hence the number of inelastic interactions in the SHADOWS lifetime is about 30. A conservative vacuum level of 1 mbar inside the decay volume is more than enough to reduce this background well below 1 event threshold in the whole SHADOWS lifetime. This is without considering the rejection due to the kinematic cuts that likely will allow to further relax the requirements on the vacuum. A detailed study will be performed for the Proposal.

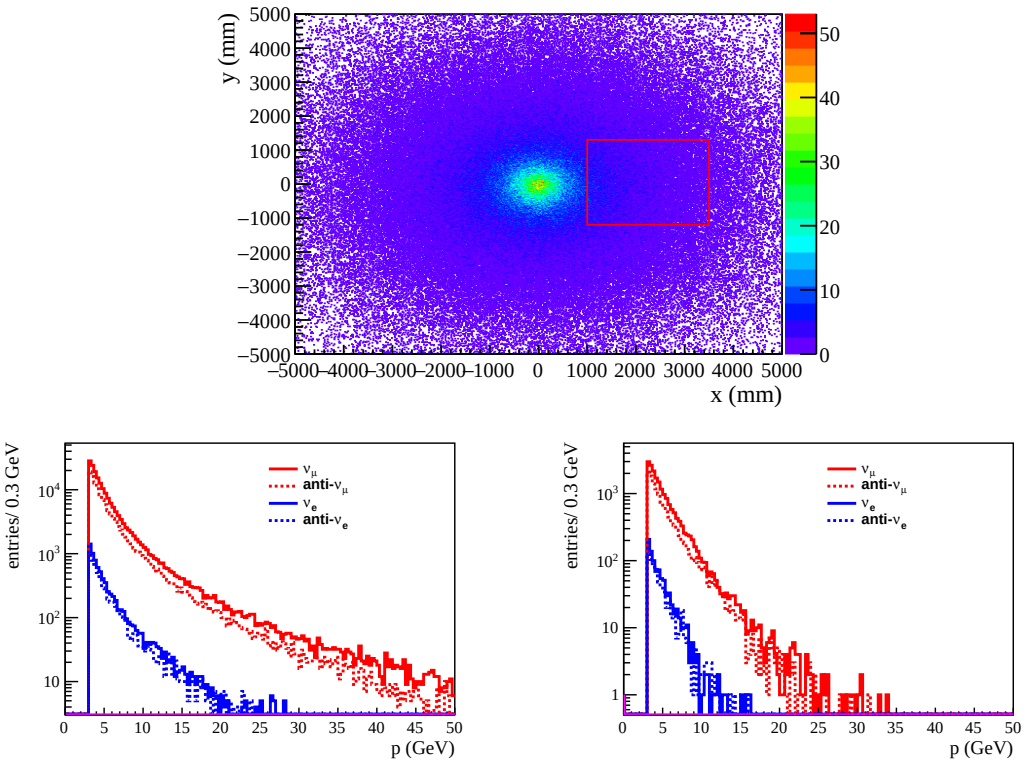

Figure 81. Top: Neutrino and anti-neutrino illumination at the level of the first SHADOWS tracking chamber. Bottom: momentum distributions in the whole solid angle (left) and in SHADOWS acceptance (right).

6.6.5 Summary of the background components

This Section summarises our current knowledge of the residual background in the SHADOWS acceptance.

- **Combinatorial dimuon background**
  The evaluation of the dimuon background in the SHADOWS acceptance has been done using the full Monte Carlo simulation of the beamline, MIB system, and the detector. In Section 6.6.3 we found that *the dimuon combinatorial background is at the level of* $\mathcal{O}(0.7)$ *events in the full experiment lifetime*, accordingly to our current understanding of the selection cuts required to reduce it and the current performance of the MIB system and the various sub-detectors.

- **Muon inelastic interactions**
  The background in acceptance arising from muon inelastic interactions with the beamline magnetic elements and MIB system evaluated with a sample of $1 \cdot 10^9$ *pot is zero within the current statistics.* A more abundant sample will be produced for the Proposal.

- **Neutrino inelastic interactions**
  The background arising from *inelastic interactions of neutrinos with the air in the decay volume is kept well below the 1 event threshold* in the whole SHADOWS lifetime by putting the decay volume in vacuum ($\sim$ 1 mbar pressure). The impact of the inelastic interactions of the neutrinos with the detector material is instead still to be evaluated, but it does not raise particular concern given the low rate of neutrinos expected in SHADOWS acceptance and the fact that the products of the interactions will be likely rejected by the requirements of having a vertex inside the decay volume and the total momentum pointing backward to the impinging point of the protons onto the dump.

What is still to be studied is the effect of muon and neutrino inelastic interactions with the decay vessel but we think that this background is not a big concern as it would not satisfy the requirement of pointing. A detailed evaluation will be done in the Proposal.

7 Physics Reach

7.1 Novelties with respect to the EoI

This Section presents the current understanding of the physics reach of the SHADOWS project for some of the benchmark channels proposed by the Physics Beyond Collider study group. The main novelties with respect to the Expression of Interest are:

1. *The implementation of the signal generation in the full Monte Carlo that allows the signal kinematic distributions obtained by toys to be validated with full MC.* This has been shown in Section 6.4, Figure 55. In general we find an excellent agreement and this proves the ability of the toys to reproduce the full MC as far as the signal distributions are concerned.

2. *The evaluation of the main background sources in the SHADOWS acceptance using the full Monte Carlo simulation of the beamline, the MIB system, and the detector.* We found that the dimuon combinatorial background is the dominant component and is currently at the level of 0.7 events for the whole SHADOWS dataset of $5 \cdot 10^{19}$ pot, after the selection requirements. The background coming from muon inelastic interactions with the detector material is at the moment zero given the current simulated dataset. Therefore there is no evidence of presence of K_S, K_L or Λ backgrounds in acceptance within the simulated background sample. The background arising from inelastic interactions of neutrinos in the decay volume is kept well below 1 event in the whole SHADOWS lifetime by putting the decay volume in vacuum ($\sim$ 1 mbar pressure). The impact of the inelastic interactions of the neutrinos with the detector material is instead still to be evaluated, but it does not raise particular concern given the low rate of neutrinos expected in SHADOWS acceptance.

3. *The evaluation of the sensitivity for ALPs with W and gluon couplings assuming the decay $ALP \to \gamma\gamma$*, that further enrich the set of sensitivity curves already shown in the EoI [12] related to light dark scalar, ALP with fermion couplings, and HNL with electron, muon, and tau couplings.

4. *A brand new proposal for a neutrino detector (NaNu)* to be placed behind the SHADOWS detector is outlined and the preliminary evaluation of the physics reach is provided.

7.2 SHADOWS sensitivity to the main benchmark channels

The sensitivity plots have been computed assuming 5×10^{19} pot. As in the EoI, the number of events of $FIP \to X^+X^-$ $(X = e, \mu, \pi, K)$ reconstructed in the SHADOWS detector is given by:

$$N_{\text{obs}} = N_{\text{pot}} \times P_{\text{FIP}} \times \sum_{X=ee,\mu\mu,\pi\pi,KK} BR(\text{FIP} \to f) \times \mathcal{A}(f) \times \varepsilon(f) \tag{7.1}$$

where N_{pot} is the number of protons on dump, P_{FIP} is the production cross-section of a given FIP with a given coupling, $\mathcal{A}(f)$ is the acceptance for a FIP of a given mass m_S and coupling parameter g decaying into a final state $f = X^+X^-$.

The acceptance is given by the product of the probability that the light scalar particle decays inside the fiducial volume and the probability $\mathcal{P}(X^+X^-)$ that the two charged tracks in the final state are "reconstructible" in the magnetic spectrometer. The efficiency $\varepsilon(f)$ is the product of the trigger, reconstruction and selection efficiencies for the final state. We consider $\varepsilon(f) = 1$ in the present study, knowing that for reasonable values of $\varepsilon(f)$ the results could change by a factor of two at most.

The position of the FIP decay vertex is required to be inside the decay volume. The decay products of the scalar are required to be within the acceptance of the magnet that has an aperture of 2.5×2.5 m^2. No reconstruction is applied, only kinematic information of the GEANT particle associated with a given hit.

The production cross-sections, the lifetime and branching ratio evaluation for light dark scalar, ALP with fermion couplings and HNLs with single flavor dominance are reported in EoI [12] and are not repeated here. The sensitivity plots for dark scalars (Figure 82), Heavy Neutral Leptons (HNLs) with electron (Figure 83), muon (Figure 84) and tau (Figure 85) couplings, and ALPs with fermion coupling (Figure 86) correspond to a sample of 5×10^{19} pot and the current SHADOWS dimensions and position in TCC8 tunnel.

The sensitivity plots for ALPs with W and gluon couplings, have been computed after the submission of the EoI and are detailed in the following Section.

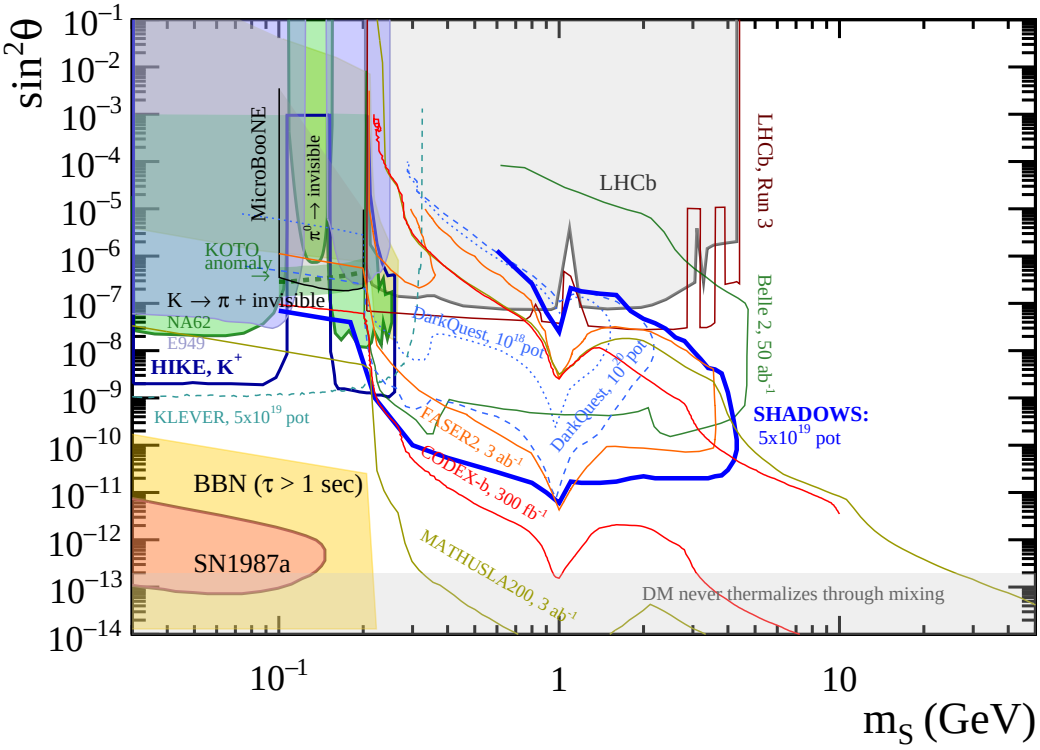

Figure 82. **Sensitivity to light dark scalar.** Shaded areas come from: reinterpretation [65] of results from CHARM experiment [66]; NA62 [67]; E949 [68, 69]; MicroBooNE [70] that excludes a light dark scalar as interpretation [71] of the KOTO anomaly; LHCb [72, 73] and Belle [74]. Coloured lines come from projections of existing/proposed experiments: NA62-dump [75] and DarkQuest [76], Belle 2 [77], FASER2 [78], CODEX-b [79], MATHUSLA [80], and KLEVER [7]. BBN and SN 1987A are from [81] and [82]. The SHiP sensitivity is not shown as it is being recomputed by the Collaboration for the forthcoming LoI.

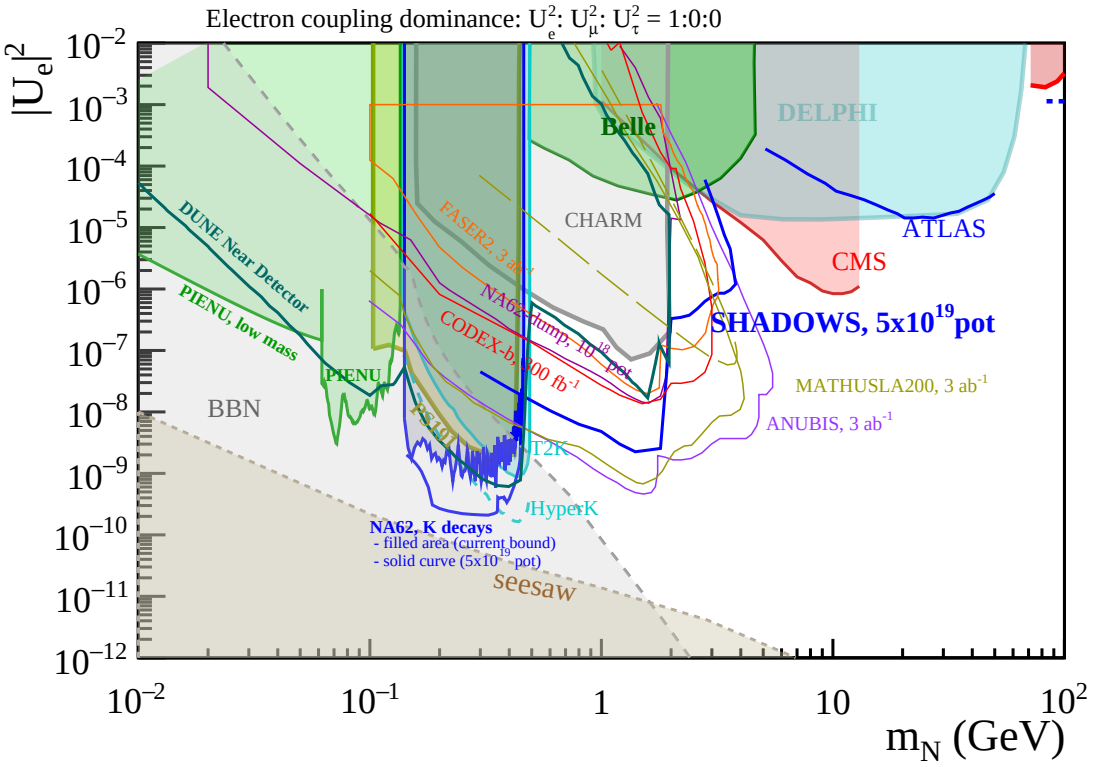

Figure 83. **Sensitivity to HNL with electron coupling.**Filled areas are existing bounds from: PS191 [83], CHARM [66], PIENU [84], NA62 (K_{eN}) [85], NA62 ($K_{\mu N}$) [86], T2K [87], Belle [88], DELPHI [89], ATLAS [90], and CMS [91]. Coloured curves are projections from: NA62-dump [7, 75], DarkQuest [76], Belle-II [92], FASER and FASER2 [78]; DUNE near detector [93], CODEX-b [79], and MATHUSLA200 [80]. The BBN bounds are from [94]. The seesaw bounds are computed under the hypothesis of two HNLs mixing with active neutrinos, and should be considered only indicative. The SHiP sensitivity is not shown as it is being recomputed by the Collaboration for the forthcoming LoI.

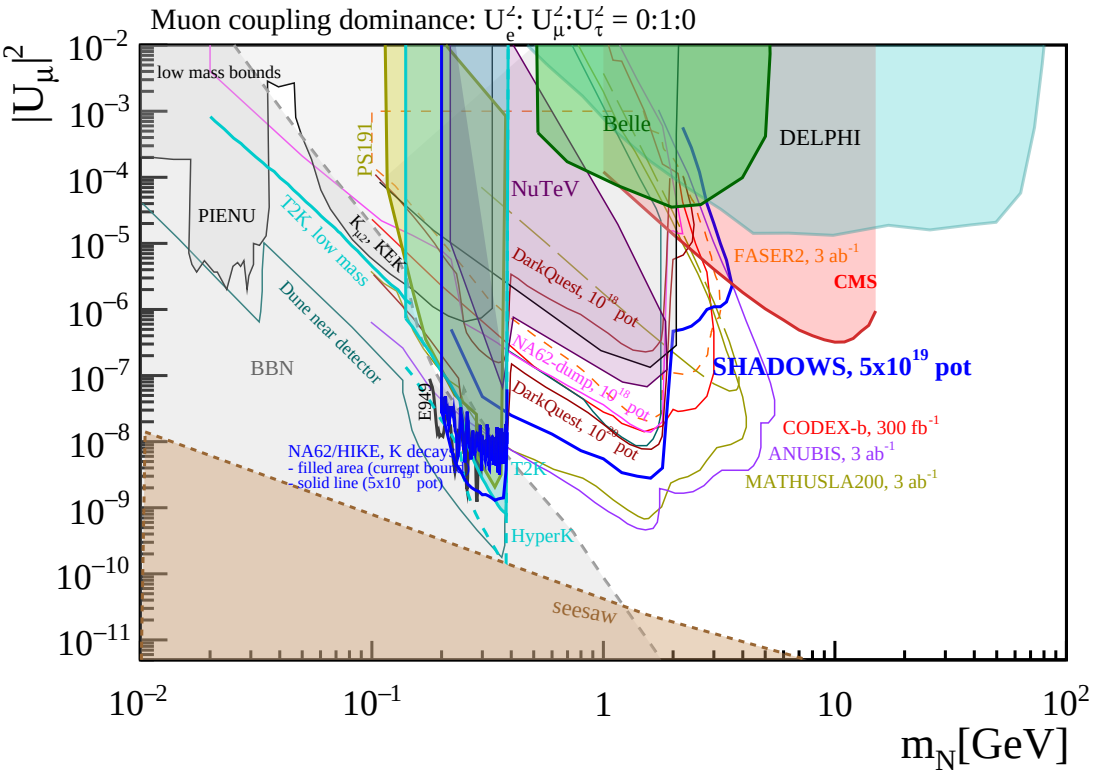

Figure 84. **Sensitivity to HNL with muon coupling.**Filled areas are existing bounds from: PS191 [83], CHARM [66], PIENU [84], NA62 (K_{eN}) [85], NA62 ($K_{\mu N}$) [86], T2K [87], Belle [88]; DELPHI [89], ATLAS [90] and CMS [91]. Coloured curves are projections from: NA62-dump [7, 75], DarkQuest [76], Belle-II [92], FASER and FASER2 [78]; DUNE near detector [93], CODEX-b [79], and MATHUSLA200 [80]. The BBN bounds are from [94]. The seesaw bounds are computed under the hypothesis of two HNLs mixing with active neutrinos, and should be considered only indicative. The SHiP sensitivity is not shown as it is being recomputed by the Collaboration for the forthcoming LoI

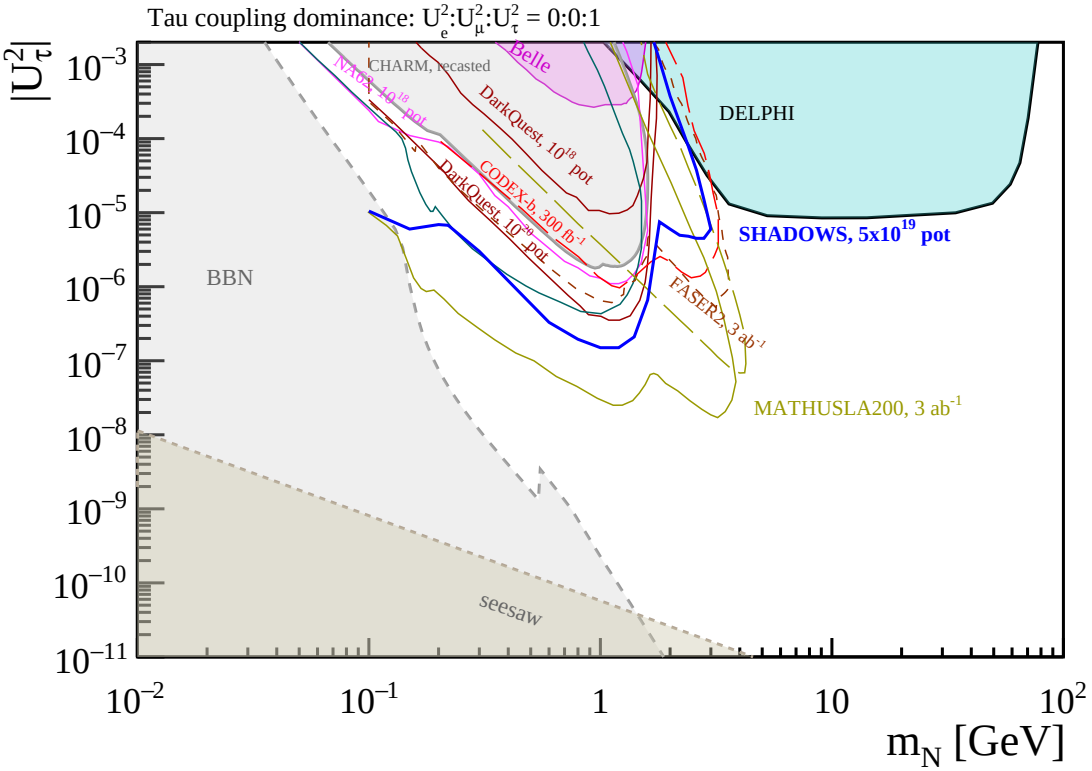

Figure 85. **Sensitivity to HNL with tau coupling.** Filled areas are existing bounds from: CHARM [66]; Belle [88]; DELPHI [89],; T2K [87] Coloured curves are projections from: NA62-dump [7, 75], DarkQuest [76], Belle-II [92], FASER and FASER2 [78]; CODEX-b [79], and MATHUSLA200 [80]. The BBN bounds are from [94]. The seesaw bounds are computed under the hypothesis of two HNLs mixing with active neutrinos, and should be considered only indicative.The SHiP sensitivity is not shown as it is being recomputed by the Collaboration for the forthcoming LoI.

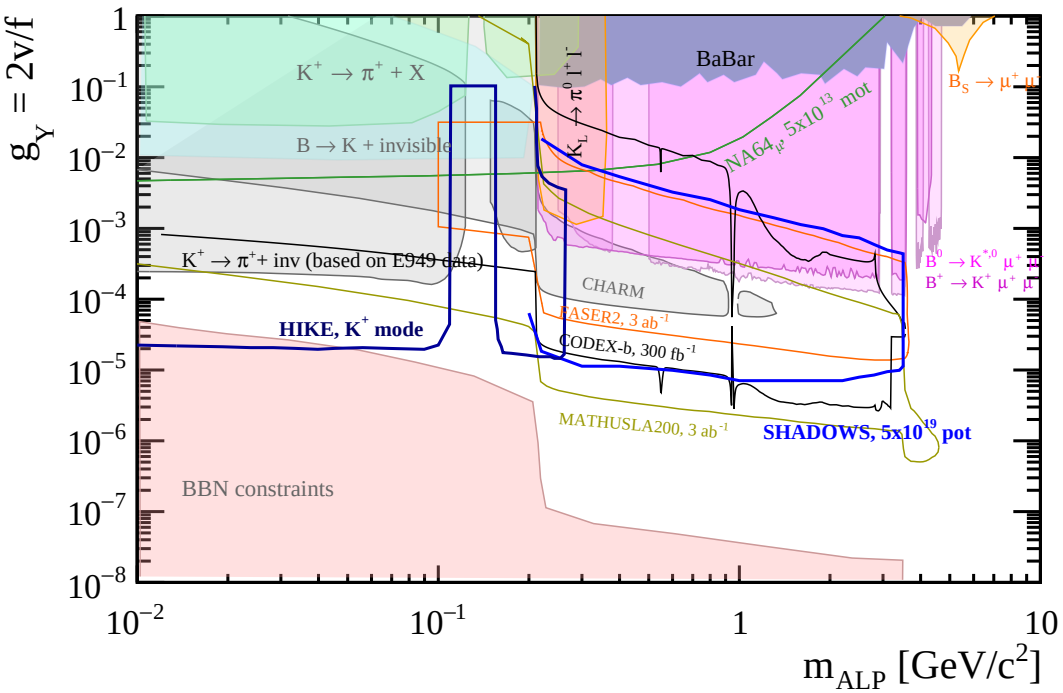

Figure 86. **Sensitivity to ALPs with fermion couplings.** Current bounds (filled areas) and prospects (solid lines) from FASER2 [78], CODEX-b [79], MATHUSLA [7], and REDTOP [7]. CHARM and LHCb filled areas have been adapted by F. Kahlhoefer, following Ref. [95]. E949 area has been computed by M. Papucci based on E949 data. All other exclusion regions have been properly recomputed by M. Papucci, following Ref. [96]. The SHiP sensitivity is not shown as it is being recomputed by the Collaboration for the forthcoming LoI.

Sensitivity for ALPs with gluon and W couplings

If the ALP interacts with the SM gauge bosons we have the following Lagrangian:

$$\mathcal{L}_a = g'^2 \frac{C_{BB}}{\Lambda} a B^{\mu\nu} \tilde{B}_{\mu\nu} + g^2 \frac{C_{WW}}{\Lambda} a W^{\mu\nu} \tilde{W}_{\mu\nu} + g_s^2 \frac{C_{gg}}{\Lambda} a G^{\mu\nu} \tilde{G}_{\mu\nu}. \tag{7.2}$$

Here g', g and g_s denote the hyper-charge, weak and strong gauge couplings respectively, $X^\mu = B^\mu, W^\mu, G^\mu$ denote the corresponding gauge fields, X denotes the field strength tensor and $\tilde{X}$ denotes its dual. We consider four different benchmark scenarios:

$$\begin{array}{lll} (i) & B \text{ dominance:} & C_{BB} \neq 0;\ C_{WW} = C_{gg} = 0 \\ (ii) & W \text{ dominance:} & C_{WW} \neq 0;\ C_{BB} = C_{gg} = 0 \\ (iii) & \text{Gluon dominance:} & C_{gg} \neq 0;\ C_{BB} = C_{WW} = 0 \\ (iv) & \text{Co-dominance} & C_{BB} = C_{WW} = C_{gg} \neq 0 \end{array}$$

The first three scenarios are chosen to highlight the different production channels. In particular, the first scenario is similar to the frequently studied case of photon dominance, except that it includes additional interactions between ALPs and Z bosons, which are however of no relevance for fixed-target experiments. The second scenario additionally predicts FCNC processes involving ALPs, effectively enhancing the ALP production. The third scenario features ALP-meson mixing and decays of ALPs into hadronic final states. Finally, the fourth scenario, first proposed in Ref. [97] and explored further in Ref. [98], investigates the potential interplay between the different couplings. Figure 87 and 88 show the SHADOWS sensitivity for ALP with W coupling (scenario ii) and with gluon coupling (scenario iv), for 5×10^{19} pot and a di-photon final state. In the same plot the bounds obtained by recasting data from NuCal and CHARM and sensitivity projections for HIKE, DUNE Near Detectors (ND) and DarkQuest are also shown, as computed in Ref. [99]. Table 11 show the numbers assumed while computing the sensitivity for NuCal, CHARM, HIKE, DUNE ND, and DarkQuest.

Table 11. Relevant parameters considered in the computation of sensitivity for ALP with W and gluon couplings for CHARM, NuCal, DUNE ND, and DarkQuest, as in Ref. [99].

Experiment	Status	E_{beam} [GeV]	N_{pot} [10^{18}]	Target	L_{DV} [m]	z_{DV} [m]
CHARM	completed	400	2.4	Cu	35	480
NuCal	completed	70.	1.7.	Fe	23	64
DUNE ND	proposed	120	1100	C	10	575
DarkQuest	proposed	120	1.44	Fe	13.5	5

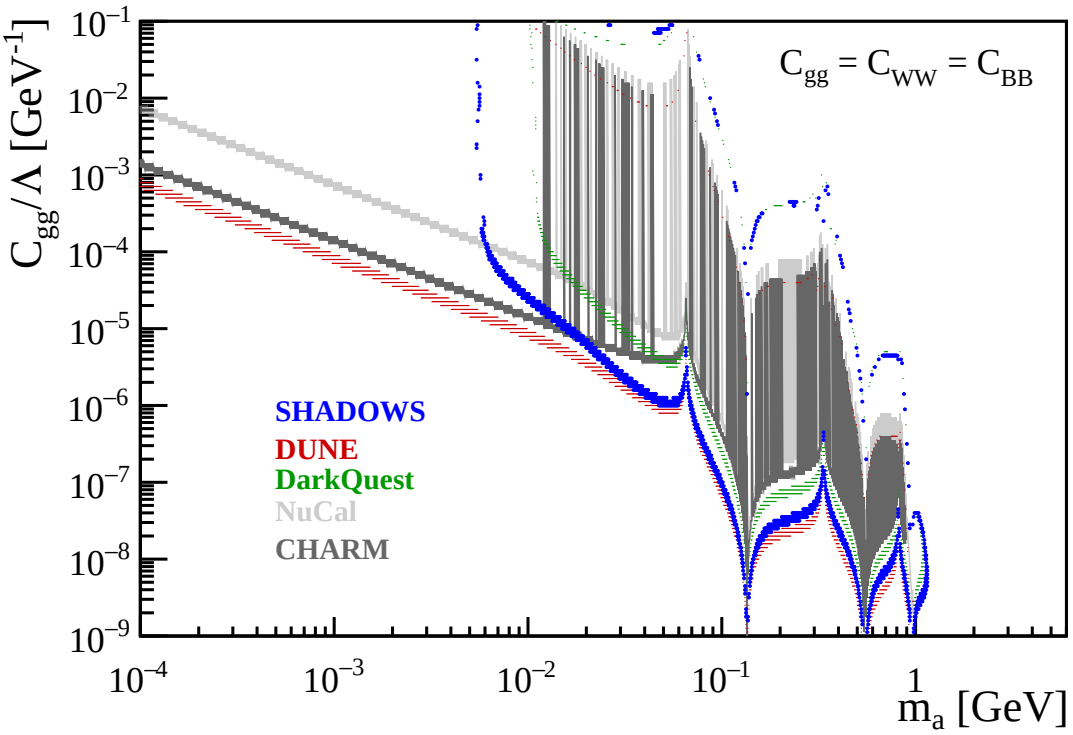

Figure 87. **Sensitivity to ALPs with gluon coupling.** The sensitivity for SHADOWS has been computed for $5 \cdot 10^{19}$ pot assuming the current dimensions and position in the TCC8 tunnel. The sensitivity for the other experiments is taken from Ref. [99]. The SHiP and HIKE sensitivities are not shown as they are being computed by the Collaborations for the forthcoming LoIs.

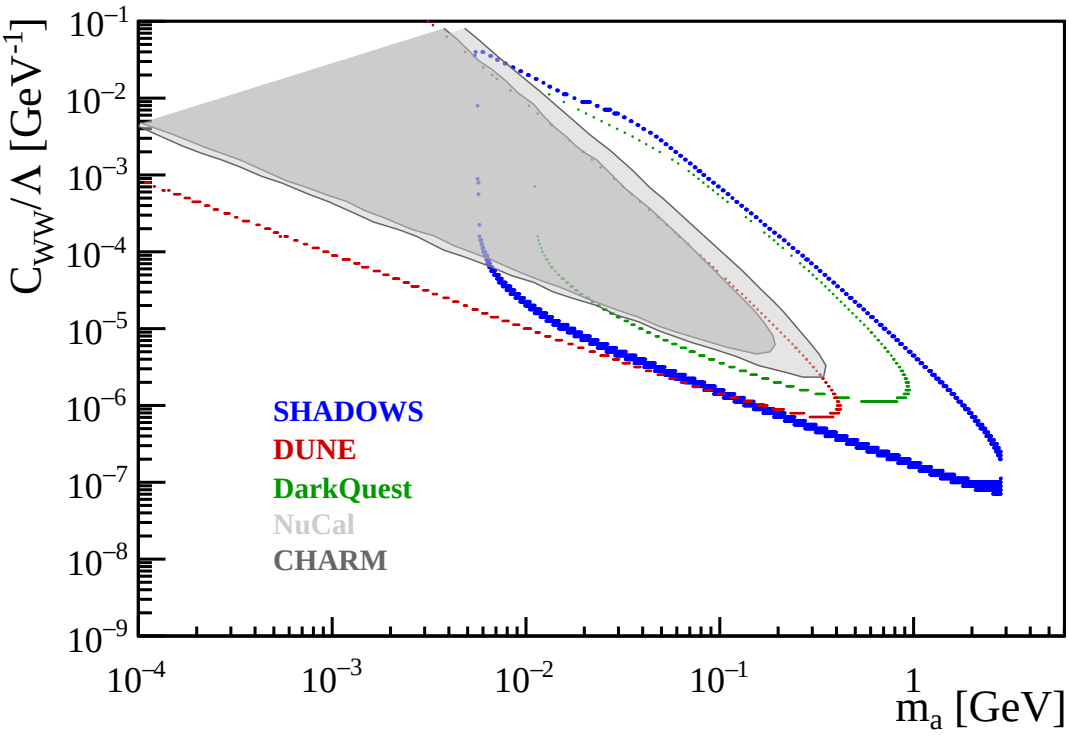

Figure 88. **Sensitivity to ALPs with W coupling.** The sensitivity for SHADOWS has been computed for $5 \cdot 10^{19}$ pot assuming the current dimensions and position in the TCC8 tunnel. The sensitivity for the other experiments is taken from Ref. [99]. The SHiP and HIKE sensitivities are not shown as they are being computed by the Collaborations for the forthcoming LoIs.

7.3 Complementarity and synergy with HIKE/K$^+$

SHADOWS and HIKE[11] in its first phase (K^+) can cover fully complementary regions in mass for most of the considered benchmarks. We assume here that both projects will collect about 5×10^{19} pot running about four years in dump and about four years in K^+ mode between LS3 and LS5. The capability of SHADOWS to cover the mass region between the K and the B masses, is complemented by HIKE unprecedented sensitivity below the K mass down to almost zero[12]. This complementarity is very visible for scalars (Figure 82), HNLs with electron and muon couplings (Figure 83 and 84), and ALPs with fermion couplings (Figure 86). The HIKE sensitivity below the Kaon mass is the best achievable by any existing or currently proposed project. Since the theory cannot indicate which mass region for FIPs should be preferred this is a strong point of the combined SHADOWS + HIKE system: together they can cover a range from almost 0 up to the B mass by improving the current bounds by one to three orders of magnitude, depending on the model and scenario. The improvement of the HIKE sensitivity will continue during its second and third phase with the K_L beam. As a side-note it is worth mentioning that the impact of the MIB system on the muon background for HIKE in beam dump mode was studied and no increase in the muon background level was found within the HIKE acceptance.

7.4 Timeliness/competitiveness with other worldwide projects

The timeliness of the SHADOWS (and HIKE) physics programme for the search for feebly-interacting particles can be understood when compared to other ongoing or proposed projects worldwide. Table 12 contains the list of running experiments and proposed projects that have sensitivity to the benchmarks channels considered in this document. Among the approved experiments, only DarkQuest and Belle II have sensitivity above the Kaon mass, where they can compete with SHADOWS.

[11] The HIKE project is detailed in the forthcoming LoI that will be submitted concurrently to the SHADOWS LoI to the SPSC.

[12] The limitation to go to zero arises by HIKE mass resolution that is tens of MeV for masses of 10 MeV.

Table 12. Worldwide competitors for SHADOWS.

experiment	status	dataset assumed in sensitivity	timescale to collect the dataset
CODEX-b	proposed	300 fb^{-1}, pp at 14 TeV	2038++
MATHUSLA	proposed	3 ab^{-1}, pp at 14 TeV	2038++
ANUBIS	proposed	3 ab^{-1}, pp at 14 TeV	2038++
DarkQuest (phase 1)	approved	10^{18} pot, 120 GeV protons	2022-2023
DarkQuest (phase 2)	proposed	10^{20} pot, 120 GeV protons	not decided
Belle 2	running	$e^+e^- at Y(4S)$, 50 ab^{-1}	2031++
T2K-ND280	running	30 GeV p	
MicroBooNE	running	8 GeV p, 10^{21} pot	
DUNE-ND	approved	120 GeV p, 10^{22} pot	2040++

8 Neutrino detector: preliminary study

Within the SM, the neutrino sector is still the least understood and key questions, e.g. on the origin of the neutrino masses, are still not answered. Several new neutrino experiments are currently in preparation or just have started to take data. A particular interesting development are new experiments at colliders, e.g. FASER [78] and SND@LHC [100], which aim for neutrino cross-section measurements in a new energy regime. Of particular interest are tau neutrinos, since the study of their properties are limited to nine ν_τ events observed at DONUT [101] and ten ν_τ candidate events at Opera [102]. The existence of anti-tau neutrinos has so far never been experimentally confirmed, making this the last missing particle within the SM. In fact, a huge number of tau- and anti-tau neutrinos could be produced in beam-dump experiments, where energies are high enough to produce $D_s^\pm$ mesons, which subsequently decay via $D_s \to \tau\nu_\tau$ with a branching fraction of about 5% [103]. Originally, the SHiP collaboration suggested a dedicated neutrino detector to study such tau-neutrino events, with a convincing physics case [104–106]. We propose a cost-efficient alternative neutrino detector, NaNu (North Area NeUtrino detector) [107], which can be realized after the main detector-system of SHADOWS and before the HIKE experiment. In the following sections, we discuss a preliminary NaNu@SHADOWS detector concept, followed by an estimate on the neutrino fluxes, the identification of neutrino signatures as well as the physics reach and a cost estimate.

Figure 89. Picture of the magnet proposed to be use for the NaNu detector.

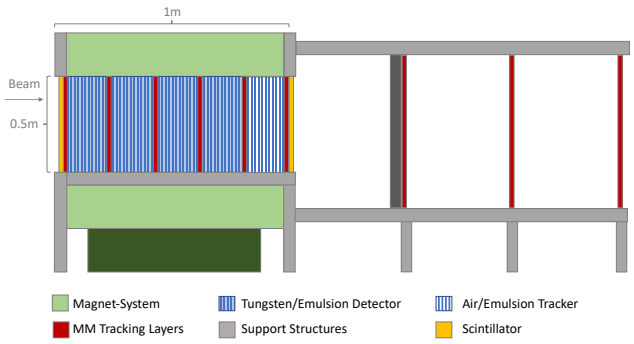

Figure 90. Side-view of the NaNu experiment with its major components: emulsion detector, magnet and tracking stations.

8.1 Detector Concept

The NaNu detector concept aims for a cost-efficient design using existing components and well established technologies. A schematic drawing of the NaNu detector is shown in Figure 90, showing its four major components, namely the magnetic system, the emulsion target, the active trigger system as well as the muon spectrometer. We suggest reusing an existing dipole magnet at CERN as shown in Figure 89 with gap dimensions of $50 \times 100 \times 100$ cm^3 and a magnetic field strength of 1.4 T generated by a current of 2500 A. The transverse plane of the NaNu detector, facing the interaction point has therefore a size of

50×100 cm^2. The emulsion target is designed with transverse size of 40×50 cm^2 and a depth of 80 cm, hence leaving 20 cm space downstream of the magnetic field.

The emulsion detector concept follows largely the current design of the FASERν Experiment [108]. It consists of silver bromide crystals with diameters of 200 nm dispersed in gelatin media interleaved with a repeated structure of absorber plates in which the actual charged current neutrino interactions occur. Emulsion detectors have a spatial resolution between 50 to 100 nm and can be interpreted as detectors with a huge density of active channels, i.e. 10^{14} per cm^3. They are therefore perfectly suited for the study of short-lived particles with unique decay vertex structures. We propose to adopt the emulsion detector design of the successfully running FASERν experiment, i.e. use emulsion films composed of two layers with a 70 μm thickness which are separated by a 200 μm thick plastic base. The emulsion films are interleaved by 1 mm tungsten plates due to their short radiation length. In total 560 tungsten plates with a total weight of the ≈ 2.2 t are foreseen. Given the significant multiple scattering effects within the tungsten plates, we foresee to place 40 emulsion tracking layers in the remaining 20 cm within the magnetic field, allowing for momentum measurements with higher precision. Those layers will be stabilized by thin aluminium plates, that are separated by 4 mm air gaps.

Since emulsion detectors cannot record timing information, all charged particles leave tracks and lead to significant pile-up. The emulsion detector is therefore complemented by six micromegas based tracking detectors with two-dimensional readout as well as a two-gap design, originally proposed in [109]. A prototype of this detector is shown in Figure 91. The thickness of these active detectors is about 15 mm and yields a spatial resolution of $\approx 100 - 150$ μm in two spatial dimensions with 3200 readout channels for each detector. The two-gap design allows in addition the reconstruction of complete tracklets with angular resolution of 0.02 rad.

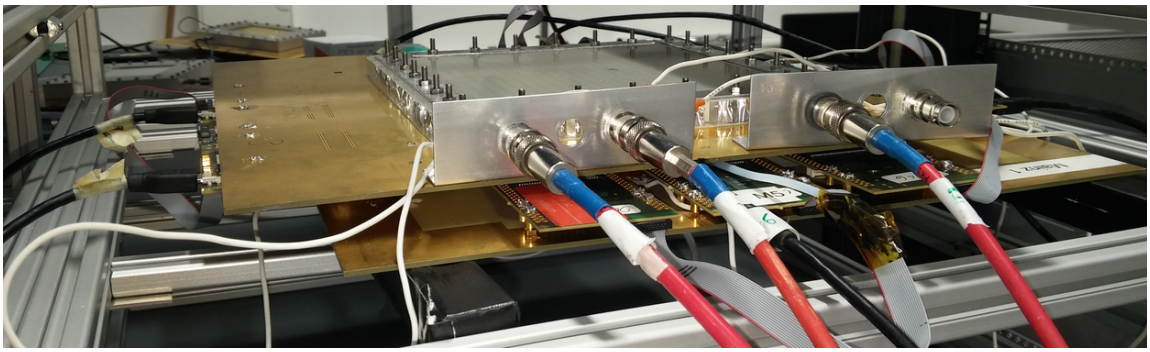

Figure 91. Picture of a micromegas with two-gap design and two-dimensional readout.

The emulsion detector and magnet system is followed by a muon spectrometer consisting of three layers of the same micromegas-based technology as previously described but with larger dimensions of 120×70 cm^2 with 6080 readout channels per detector layer. The three layers are separated by 50 cm each, while the first layer is shielded in addition with a 20 cm iron layer to suppress hadronic particles. The active trigger system of NaNu

makes use of plastic scintillators, which are located in the front as well as in the back of the emulsion layers, where they can be also used to veto muon signatures. In addition, the self-triggering capabilities of micromegas detectors can be used to record events which only leave signatures within the emulsion target.

The location of the NaNu Experiment is foreseen 50 m after the beam dump, i.e. behind the SHADOWS experiment. The distance to the beam axis is chosen to minimize the expected muon background. Muons for the SHADOWS experiment are shielded by dedicated magnetized iron blocks. The expected muon background for 4×10^{19} proton on target in the transverse plane to the beam line is shown in Figure 92. The neutrino flux and the neutrino energies increase when moving towards the beam-line, however, also the muon-flux increases significantly. It is typically assumed that the reconstruction algorithms of emulsion detectors can handle $\approx 10^6$ tracks per cm^2. The position of NaNu in the transverse plane was therefore optimized to be closest as possible to the beam-line, but the number of 10^6 muons per cm^2 per year operation is not exceeded. This implies an optimal location of NaNu in the transverse plane with the coordinates $x_1 = 1$m to $x_2 = 1.5$m and $y_1 = 1.0$m and $y_2 = 1.4$m.

8.2 Neutrino Fluxes

Tau-neutrinos passing through the NaNu detector stem primarily from mesonic decays of $D_s \to \tau\nu_\tau$, together with a high rate of ν_μ and ν_e neutrinos, which appear as decay products of charmed hadrons and soft pions and kaons. Our estimate of neutrino fluxes is based in studies of Pythia8 [110] and the Genie program [111] and then cross-checked with the published studies of the Scattering and Neutrino Detector (SND) of the SHIP experiment [104, 104, 105]. The SND detector is assumed to be placed about 35 m after the interaction point, directly following the beamline. Its neutrino interaction target has a transverse size of 0.8×0.8 m^2, a depth of ≈ 1 m and consists of passive absorber material interleaved with 19 emulsion and 19 tracking planes.

Since the production processes of neutrinos is the same for SND as for NaNu, the kinematic distributions of the produced neutrinos is equivalent for both experimental setups. However, the differences of the expected number of neutrino interactions are due to the different location, the different size as well as the different assumed number of protons on target.

In four years of operation, we assume to have collected data corresponding to 5×10^{19} POT, i.e. a factor of 4 less compared to SND assumptions. The amount of passive absorber material also is significantly smaller for NaNu with a volume of 0.11 m^3 and a weight of 2.2 t, yielding a further reduction by a factor of 3.3. Most important, however, is the difference in the actual location. Pythia8 [110] was used to estimate the kinematic distributions of all neutrino flavours after the initial proton-proton interactions. The angular distributions for electron, muon, and tau neutrinos is shown in Figure 93. In addition, the neutrino energy dependence on the neutrino interaction cross-sections have to be considered. In fact, the average neutrino energy reduces by up to 30 GeV, depending on the neutrino flavour, when placing the NaNu Detector with a distance of 1.5 to 2.0 m to the beam axis,

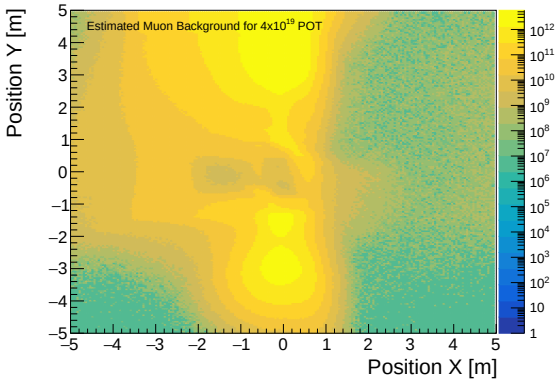

Figure 92. Estimated muon background in the transverse plane to the beam axis at a distance of 50m after the beam dump for// 4×10^{19} protons on target.

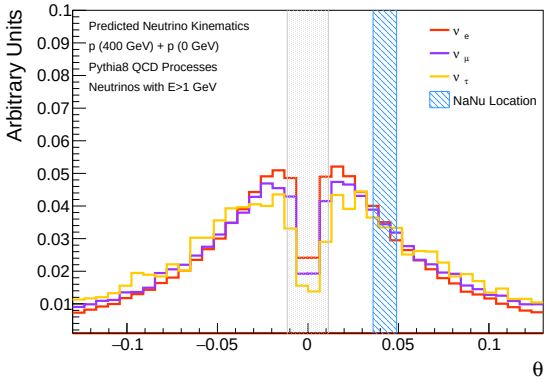

Figure 93. Normalized angular distributions of neutrinos with E¿1 GeV produced in 400 GeV proton beam collisions on a fixed proton target using PYTHIA8. The location of NaNu is indicated as blue shaded area.

Flavor	$< E >$	Interactions (4×10^{19} POT)
ν_e	≈16 GeV	16.6×10^3
ν_μ	≈20 GeV	60.8×10^3
ν_τ	≈27 GeV	0.6×10^3
$\bar{\nu}_e$	≈13 GeV	3.9×10^3
$\bar{\nu}_\mu$	≈16 GeV	13.5×10^3
$\bar{\nu}_\tau$	≈32 GeV	0.4×10^3

Table 13. Expected energy range of neutrinos and number of neutrino interactions within the NaNu detector.

implying significant lower cross-section in comparison to more high energetic neutrinos. The expected neutrino interactions in the NaNu detector due to its position is expected to be therefore reduced by a factor of 0.1 for electron neutrinos, and by a factor of 0.2 for muon and tau neutrinos. The final estimates of expected neutrino interactions per flavor are summarized in Table 13.

8.3 Detector Simulation and Neutrino Identification

The NaNu detector concept has been implemented in GEANT4 [56] while the primary neutrino interactions with the passive detector material have been simulated via the GENIE program. It should be noted that the theoretical uncertainties on the actual neutrino fluxes as well as the hadronization model are typically larger than the experimental uncertainties involved in the following studies.

Neutrino interactions of all flavours require at least two tracks with an energy of 1 GeV associated to a common vertex with an impact parameter smaller than 10 μm, one stemming from the lepton, the other(s) from the recoil of the nucleus. Tracks with

larger impact parameters are treated as seed candidates for a secondary vertex. Secondary vertices can be defined via kinks on their corresponding tracks w.r.t. to the primary tracks as well as a by displacement of more than 20 μm to the primary vertex. Primary and secondary decay vertices are searched for in all emulsion layers of NaNu except those close to the downstream tracking layers with a 1 cm margin. This reduces the acceptance of the NaNu detector by approximately 5%.

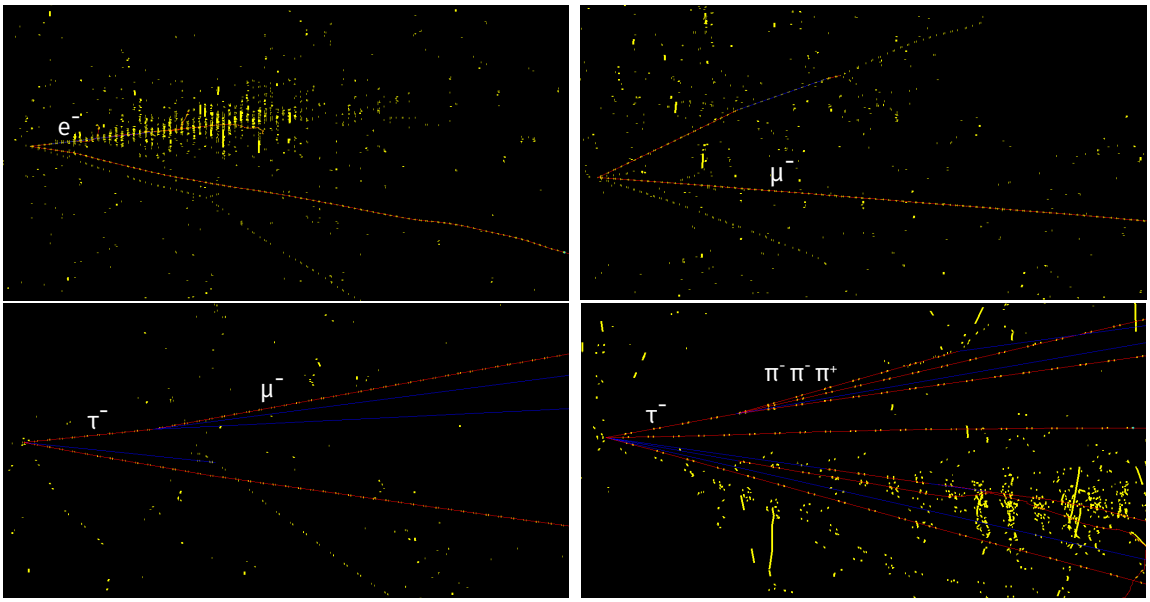

Figure 94. Event Displays of the primary and secondary particle trajectories of electron neutrino (upper left) and muon neutrino (upper right) interactions with the NaNu Detector. Two example of tau neutrino interactions are shown in the lower row in the muonic decay channel (left) and the $\tau \to \pi^+\pi^-\pi^-$ decay channel (right). The charged (neutral) particles are indicated by red (blue) lines. Only particles with momenta larger than 1 GeV are shown.

Electron neutrino interactions are identified by the characteristic electromagnetic showers of the electron as shown in Figure 94. A 90% detection efficiency is assumed, in line with studies of similar neutrino experiments. Given the short electron tracks, no charge measurement is possible. In total, we expect about 18000 reconstructed electron neutrino events in the NaNu detector.

Muon neutrino interactions (Figure 94) can be identified by a primary vertex in the emulsion layer with one long track leaving the vertex. The curvature of the track in the magnetic field allows for a momentum measurement, using a combination of tracklets in the emulsion layers, the tracking layers as well as the muon spectrometer. The main sensitivity on the momentum comes from the measurements in the emulsion tracking layers in the last 20 cm of the magnetic field as well as from the muon spectrometer, since muons are subject to significant multiple scattering in the upstream passive detector layers. The expected momentum resolution for muon tracks in the NaNu detector has been estimated using a full GEANT4 simulation and is shown for 5 and 10 GeV muons in Figure 95. The resulting charge identification is correct in more than 98% of all recorded muon neutrino

events. Assuming an 80% identification efficiency of the muons in the active tracking layers, we expect 40000 and 10000 reconstructed muon neutrino and anti-muon neutrino events, respectively. In fact, muon neutrino interactions could – in principle – be reconstructed using the active micromegas-based tracking detectors in standalone mode, if the primary muon neutrino interaction happens close the tracking layer and thus leaving a distinct signature of the recoil tracks of the nucleus. Detailed studies on this aspect are still ongoing.

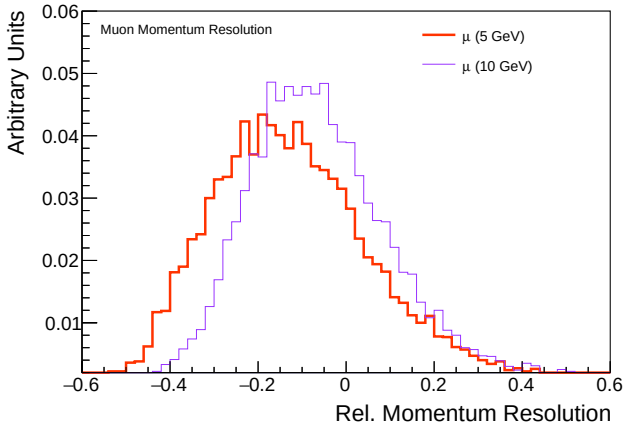

Figure 95. Relative momentum resolution for muons with an energy of 5 and 10 GeV.

The event topology of tau neutrino interactions depends on the subsequent decay of the tau lepton and, hence, the presence of a secondary vertex. The secondary vertex is expected to be reconstructed with an efficiency of $\approx 60\%$. The electron and muon decays channels of the tau yield a kink between the original tau track and the subsequent electron or muon tracks. The decay leptons can be identified as described above. The hadronic tau decays are identified by their short-lived decays and distinguished by the number of charged hadrons in the final state, i.e. into one or three charged pions. The three-pion decay has a unique topology, while the one-pion decay has a similar vertex structure as the muonic decay, however with a shorter track-length of 12.5 cm. This allows also for a momentum measurement using the tracking information within the magnetic field, where a significant better momentum resolution is achieved for tau-decays that happen close to end of the passive emulsion detector layers. While studies on the momentum resolution for pions are still ongoing, preliminary results show that a correct charge identification is possible in more than 50% for all $\tau \to h$ decays, with a false charge identification rate of 10%. The total number of reconstructed ν_τ and $\bar{\nu}_\tau$ interactions at NaNu is nearly 500 events, detailed in Table 14 together with the efficiency losses at various stages of the identification. So far, only the charge identification in the muon and single-hadron decay topologies have been studied. Neglecting a possible charge identification in the electron and three hadron final state, we expect to identify 100 ν_τ and 60 $\bar{\nu}_\tau$ interactions at NaNu for 5×10^{19} POT.

The main background in the tau lepton identification is due to the charm hadron production in ν_μ interactions via charged current interactions in the passive detector material.

The subsequent decay topology of those hadrons has a similar decay topology as the tau decays when the primary lepton is not correctly identified. Hence the performance of the muon identification system is crucial for the background rejection. Given a larger reduction of the ν_μ interaction rate compared to SND@SHIP, we expect also a similar or even smaller background contribution in the ν_τ identifications.

	$\tau \to e$	$\tau \to \mu$	$\tau \to h(\pi^\pm)$	$\tau \to 3h(3\pi^\pm)$	$\bar{\tau} \to e$	$\bar{\tau} \to \mu$	$\bar{\tau} \to h(\pi^\pm)$	$\bar{\tau} \to 3h(3\pi^\pm)$
BR	0.17	0.18	0.46	0.12	0.17	0.18	0.46	0.12
Geometrical	0.9	0.9	0.9	0.9	0.9	0.9	0.9	0.9
Decay search	0.6	0.6	0.6	0.6	0.6	0.6	0.6	0.6
PID	1.0	0.8	0.9	0.9	1.0	0.8	0.9	0.9
Total Events	50	50	150	40	30	30	100	30

Table 14. Overview of various tau decay channels including their branching ratio (BR) together with the efficiencies of various selection and identification criteria. The last row indicated the expected number of reconstructed ν_τ events within NaNu.

8.4 Expected Physics Reach

The number of identified ν_τ and $\bar{\nu}_\tau$ interactions in NaNu exceeds the previous statistics by nearly two orders of magnitude, allowing for a $\bar{\nu}_\tau$ observation during the first year of data taking already. Beyond the first experimental observation of anti-tau neutrinos, neutrino interaction cross-sections of all flavours in the energy regime between 5 and 50 GeV can be measured with statistical and experimental uncertainties below 10%. The NaNu datasets provide therefore a unique opportunity to test lepton universality in neutrino interactions. All cross-section measurements are typically limited by the uncertainties on the initial neutrino flux. However, those uncertainties are of similar size in all neutrino collider experiments.

As mentioned in the previous section, the $\bar{\nu}_\mu$ interactions in the passive detector material lead to significant charm hadron production, allowing to probe the strange quark content of the nucleon. Assuming a similar charm reconstruction efficiencies as SND@SHiP, we expect $\approx 2 \times 10^3$ identified charm hadrons in NaNu, adding significantly to the exciting data-sets, potentially allowing to constrain further the parton distribution functions of protons.

Similarly to the determination of the upper limit for the magnetic moment of the tau neutrino by the DONUT Collaboration [101, 112], a study on the ν_τ magnetic moment can be performed at NaNu. Assuming similar systematic uncertainties but significantly improved statistics, it is expected to lower the upper limit by a factor of two to $2 \times 10^{-7} \mu_B$. The potential impact of the NaNu datasets on the study of the F_4 and F_5 structure functions has still to be studied.

8.5 Estimated Costs

The existing dipole magnet (MNP 22/B) is the baseline choice for the magnet-system of the NaNu experiment. While it should be fully functional, it was not in active use in the past years and certain repair and refurbishing costs might arise. Those are estimated

to not exceed 100 k€. The weight of the emulsion detector system requires a dedicated support frame, which allows an easy access for replacing the emulsion layers. Based on the support frame costs of the FASER experiment, 30 k€ should be sufficient to build the support frame.

The costs of the emulsion detector, including gel and film as well as additional infrastructure such as chemicals and tooling are estimated based on the costs of the FASERν experiment [108] and scaled to the larger emulsion detector volume. The costs of the tungsten plates, which will be used as absorber material, is conservatively estimated using current market prices. The corresponding costs are summarized in Table 15.

The micromegas-based tracking chambers can be produced by the CERN workshops with a preliminary cost estimate of 100 k€ in total. The readout system will be based on the VMM-2 chipset [49], yielding overall costs of 280 k€. Additional costs for the veto plastic scintillators, the gas-system, the high-voltage supply as well as the basic computing infrastructure amount to 100 k€, resulting in overall estimated costs of the NaNu experiment of 1960 k€.

Support Structure	30 k€
Magnet Refurbishment	100 k€
Emulsion Detector (Gel + Film)	600 k€
Emulsion Film Production Costs	100 k€
Infrastructure (chemicals, tools, racks)	50 k€
Tungsten Plates (2400 kg)	600 k€
Small Micromegas Tracking Stations (6x)	60 k€
Large Micromegas Tracking Stations (3x)	40 k€
Micromegas Readout System (VMM chip)	280 k€
Veto Plastic Scintillators	20 k€
Gas-System	30 k€
High-Voltage Supply	20 k€
Computing	30 k€
Total	**1,960 k€**

Table 15. Overview of the expected costs for the NaNu Experiment. The costs for the emulsion detector as well as the production costs cover one year of running, allowing for a first observation of anti-tau neutrino events.

8.6 Summary

We proposed a cost effective experiment to study neutrino interactions at the SPS collider in an energy range of 20 to 60 GeV with a focus of tau neutrinos. The NaNu Experiment can be realized in the North Area of CERN between the future SHADOWS and HIKE Experiments and is based on well established technologies. The first experimental distinction of tau and anti-tau neutrinos can be already achieved with the first year of data taking. Furthermore, new upper bounds on the anomalous magnetic moment of tau neutrino are expected as well as precise neutrino cross-section measurements of all flavors. This study

should mainly serve as a proof of concept and more detailed studies on the physics reach as well as the final detector concept are necessary. Most performance estimates have to be treated as preliminary. However, it becomes evident, that tau neutrino physics can be successfully conducted also off-beam axis in parallel to the operation of the SHADOWS experiment. More investments on the additional (and dedicated) muon shielding would allow to bring the NaNu detector closer to the beam-line might even allow to increase the expected signal yields by a factor of 2-5. It should be noted that the envisioned energy range is complementary to the neutrino program of FASER-2 and even a common development of baseline technology could be envisioned.

9 Schedule and preliminary cost estimate

The schedule of the SHADOWS proposal (and NaNu detector) is shown is Figure 96. Following a possible positive outcome of the CERN Research Board for the increase of the beam intensity in ECN3/TCC8, we plan to submit the Proposal to the SPSC in fall 2023. In case of approval we envisage to prepare a Technical Design Report (TDR) by mid-end of 2024. This would allow a timely start of the construction immediately after to cope with current schedule of the CERN accelerator complex that foresees a long shutdown (LS3) in 2026-2027 for the North Area during which we plan to install the detector. The first pilot run could be performed in 2028.

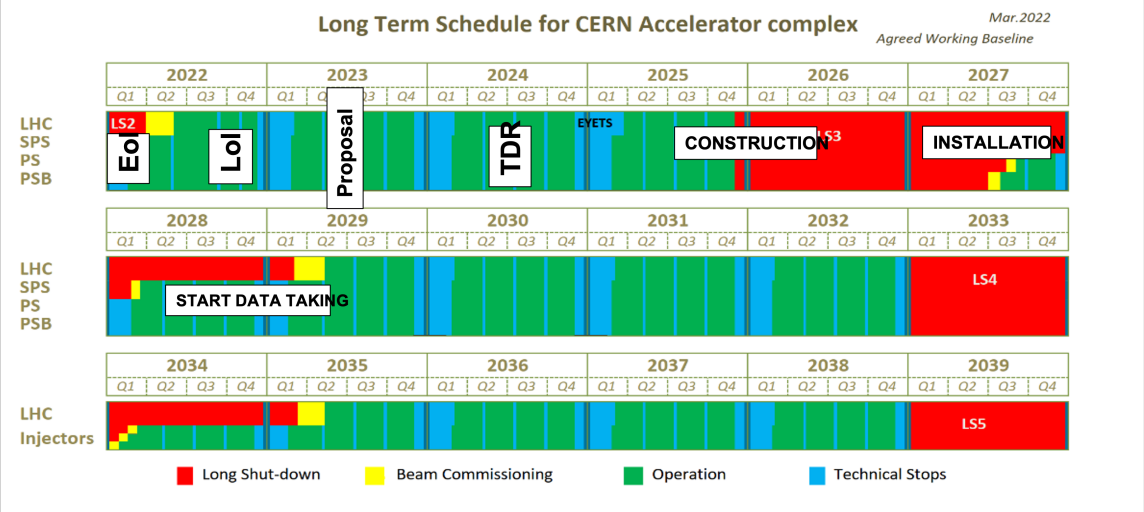

Figure 96. Tentative SHADOWS schedule.

The overall cost of the experiment will be driven by the choice of the detector technologies that are currently under scrutiny. Still a preliminary cost estimate can be given, based on the current knowledge of several technology options. This is shown in Table 16. Here we assume the (conservative) case in which we have to build all the detectors as new. Clearly the cost will decrease if we can use part of existing detectors. Still there is an caveat to be taken into account: the prices are based on our knowledge of the market before the war in Ukraine. We are aware that the prices are increasing but to date it is impossible for us to foresee by how much. A more refined estimate will be provided in the Proposal.

The two critical items we see in this list are the dipole magnet of the tracking system (whose cost has been estimated on the basis of the NA62 dipole magnet and should be updated for the new design) and the decay vessel. Both items should be provided by CERN as Host Institution while the rest of the cost could be shared among the other Collaborating Institutions.

The cost of the neutrino detector (NaNu) described in details in the previous section, is repeated in Table 16 for reader's convenience.

Table 16. Preliminary cost estimate of SHADOWS sub-detectors. The cost of the NaNu experiment is reported in the last row. The cost is based on prices evaluated before the war in Ukraine. A more refined cost estimate will be provided in the Proposal.

Sub-detectors	Possible Technology	very preliminary) cost
Upstream Veto	Micromegas	0.3 M€
Decay Vessel	in vacuum	1 M€
Dipole Magnet	warm	4-5 M€
Tracker	SciFi	4 M€
Timing Layer	small scintillating tiles	0.1-0.2 M€
ECAL	Shashlik	2-3 M€
Muon	scintillating tiles	0.4-0.5 M€
TDAQ & offline	NA62-based	o(1-2) M€
Total SHADOWS		**12.4-15.5 M€**
Total NaNu		**1.960 €**

10 Conclusions and Outlook

The physics of the feebly-interacting particles (also dubbed dark sector) has exploded in the past few years with a wealth of experimental proposals presented in all the main laboratories in the world (FNAL, SLAC, JLAB, KEK, LNF, DESY, and PSI) and a lively theoretical and phenomenological activity. SHADOWS (and HIKE) could play a major role in the coming years becoming a hot spot for FIP physics in the worldwide landscape. The upgrade in intensity of the P42 beamline would allow CERN to have a world-class facility with several experiments running in parallel in the same area covering a broad spectrum of physics topics (flavour, neutrino physics, and searches for new feebly-interacting phenomena) with a set of small-medium size experiments, and therefore allowing a high degree of diversity which is crucial, we think, for the future of particle physics.

References

[1] G. Lanfranchi, M. Pospelov and P. Schuster, *The Search for Feebly-Interacting Particles*, 2011.02157.

[2] J. L. Feng et al., *Planning the Future of U.S. Particle Physics (Snowmass 2013): Chapter 4: Cosmic Frontier*, in *Community Summer Study 2013: Snowmass on the Mississippi*, 1, 2014, 1401.6085.

[3] J. L. Hewett et al., *Planning the Future of U.S. Particle Physics (Snowmass 2013): Chapter 2: Intensity Frontier*, in *Community Summer Study 2013: Snowmass on the Mississippi*, 1, 2014, 1401.6077.

[4] J. Alexander et al., *Dark Sectors 2016 Workshop: Community Report*, 8, 2016, 1608.08632.

[5] M. Battaglieri et al., *US Cosmic Visions: New Ideas in Dark Matter 2017: Community Report*, in *U.S. Cosmic Visions: New Ideas in Dark Matter*, 7, 2017, 1707.04591.

[6] J. Alimena et al., *Searching for long-lived particles beyond the Standard Model at the Large Hadron Collider*, *J. Phys. G* **47** (2020) 090501, [1903.04497].

[7] J. Beacham et al., *Physics Beyond Colliders at CERN: Beyond the Standard Model Working Group Report*, *J. Phys. G* **47** (2020) 010501, [1901.09966].

[8] C. A. Argüelles et al., *New opportunities at the next-generation neutrino experiments I: BSM neutrino physics and dark matter*, *Rept. Prog. Phys.* **83** (2020) 124201, [1907.08311].

[9] R. K. Ellis et al., *Physics Briefing Book: Input for the European Strategy for Particle Physics Update 2020*, 1910.11775.

[10] P. Agrawal et al., *Feebly-Interacting Particles:FIPs 2020 Workshop Report*, 2102.12143.

[11] U. B. et al., *European Strategy for Particle Physics Update 2020: Recommendations*, in *https://cds.cern.ch/record/2721370/files/CERN-ESU-015-2020%20Update%20European%20Strategy.pdf*.

[12] W. Baldini et al., *SHADOWS (Search for Hidden And Dark Objects With the SPS)*, 2110.08025.

[13] M. Brugger et al., *Mandate of the PBC ECN3 Task Force*, tech. rep., CERN, Geneva, 2022.

[14] Y. Kadi (et al.), *Strategy for the Consolidation and Upgrade of the North Experimental Area*, tech. rep., CERN, Geneva, 2018.

[15] Y. Kadi (et al.), *Addendum to the NA Consolidation Study Report*, tech. rep., CERN, Geneva, 2019.

[16] Y. Kadi (et al.), *The North Area Consolidation Project Roadmap*, tech. rep., CERN, Geneva, 2021.

[17] e. a. L. Gatignon, *Report from the Conventional Beams Working Group to the Physics Beyond Collider Study and the European Strategy for Particle Physics*, tech. rep., CERN, Geneva, December, 2018.

[18] A. Charalambous et al., *User Requirements for a High Intensity Beam Facility at TCC8/ECN3*, tech. rep., CERN, Geneva, 2022.

[19] E. Montbarbon et al., *Studies of the Conventional Beams Working Group within the Physics Beyond Colliders framework at CERN*, *Nucl. Instrum. Meth. B* **464** (2020) 1–4.

[20] L. Gatignon (et al.), *Report from the Conventional Beams Wrorking Group to the Physics Beyond Colliders Study and to the European Strategy for Particle Physics*, tech. rep., CERN, Geneva, December, 2018.

[21] D. Meeker, S. Hang, R. Cornelius, S. Engstrom, P. Krc, V. Petoukhov et al., *Finite element method magnetics*, .

[22] L. Nevay, S. Boogert, J. Snuverink, A. Abramov, L. Deacon, H. Garcia-Morales et al., *Bdsim: An accelerator tracking code with particle–matter interactions*, *Computer Physics Communications* **252** (2020) 107200.

[23] S. Agostinelli, J. Allison, K. Amako, J. Apostolakis, H. Araujo, P. Arce et al., *Geant4—a simulation toolkit*, *Nuclear Instruments and Methods in Physics Research Section A: Accelerators, Spectrometers, Detectors and Associated Equipment* **506** (2003) 250–303.

[24] G. D'Alessandro, *Studies for current and future high intensity experiments at the CERN P42 and K12 beam lines*, Ph.D. thesis, Royal Holloway, University of London, 2022.

[25] F. W. Stummer, *Studies and Optimization for Future Beam Dump Experiments in the K12 and P42 Beams at CERN*. Jun, 2021.

[26] T. Kawamoto et al., *New Small Wheel Technical Design Report*, .

[27] T. Alexopoulos et al., *Development of large size Micromegas detector for the upgrade of the ATLAS muon system*, *Nucl. Instrum. Meth. A* **617** (2010) 161–165.

[28] M. Alviggi et al., *Construction and test of a small-pad resistive Micromegas prototype*, *JINST* **13** (2018) P11019.

[29] M. Iodice, M. Alviggi, M. T. Camerlingo, V. Canale, M. D. Pietra, C. D. Donato et al., *Small-Pad Resistive Micromegas: rate capability for different spark protection resistive schemes*, *JINST* **15** (2020) C09043.

[30] T. Alexopoulos et al., *Performance studies of resistive-strip bulk micromegas detectors in view of the ATLAS New Small Wheel upgrade*, *Nucl. Instrum. Meth. A* **937** (2019) 125–140.

[31] NA62 collaboration, E. Cortina Gil et al., *The Beam and detector of the NA62 experiment at CERN*, *JINST* **12** (2017) P05025, [1703.08501].

[32] NA62 collaboration, N. Collaboration, *NA62: Technical Design Document*, Tech. Rep. NA62-10-07, CERN, Geneva, Dec, 2010.

[33] L. collaboration, *LHCb Tracker Upgrade Technical Design Report*, tech. rep., CERN, Geneva, February, 2014.

[34]

[35] H. Kolanoski and N. Wermes, *Particle Detectors*. Oxford University Press, 6, 2020.

[36] NA62 collaboration, E. Temur, *NA62 Straw Tracker*, in *Instrumentation for Colliding Beam Physics 2017 (INSTR 2017)*, DOI.

[37] SHiP collaboration, C. Betancourt, A. Dätwyler, N. Serra, B. Storaci, A. Blondel, A. Korzenev et al., *A timing detector for the SHiP experiment*, *Nucl. Instrum. Meth. A* **924** (2019) 369–372.

[38] G. S. Atoian et al., *Lead scintillator electromagnetic calorimeter with wavelength shifting fiber readout*, *Nucl. Instrum. Meth. A* **320** (1992) 144–154.

[39] PHENIX collaboration, L. Aphecetche et al., *PHENIX calorimeter*, *Nucl. Instrum. Meth.*

A **499** (2003) 521–536.

[40] E. P. Hartouni et al., *HERA-B: An experiment to study CP violation in the B system using an internal target at the HERA proton ring. Design report*, .

[41] LHCb collaboration, *LHCb calorimeters: Technical design report*, .

[42] E865 collaboration, R. Appel et al., *A large acceptance, high-resolution detector for rare K+ decay experiments*, *Nucl. Instrum. Meth. A* **479** (2002) 349–406.

[43] G. S. Atoian et al., *An Improved Shashlyk Calorimeter*, *Nucl. Instrum. Meth. A* **584** (2008) 291–303, [0709.4514].

[44] G. S. Atoian, V. V. Issakov, O. V. Karavichev, T. L. Karavicheva, A. A. Poblaguev and M. E. Zeller, *Development of Shashlyk calorimeter for KOPIO*, *Nucl. Instrum. Meth. A* **531** (2004) 467–480, [physics/0310047].

[45] T. Awes et al., *High Energy Beam Test of the PHENIX Lead-Scintillator EM Calorimeter*, nucl-ex/0202009.

[46] CMS collaboration, C. Collaboration, *The Electromagnetic calorimeter project: Technical Design Report*, Tech. Rep. CMS-TDR-4, CERN, Geneva, Oct, 1997.

[47] P. Chau, *Optimierung von hochauflösenden Sampling-Kalorimetern mit szintillatorbasierter SiPM-Auslese*, Ph.D. thesis, Mainz U., 2022. 10.25358/openscience-7043.

[48] SHiP collaboration, W. M. Bonivento, *Studies for the electro-magnetic calorimeter SplitCal for the SHiP experiment at CERN with shower direction reconstruction capability*, *JINST* **13** (2018) C02041.

[49] ATLAS Muon collaboration, G. Iakovidis, *VMM - An ASIC for micropattern detectors*, *EPJ Web Conf.* **174** (2018) 07001.

[50] CALICE collaboration, F. Sefkow and F. Simon, *A highly granular SiPM-on-tile calorimeter prototype*, *J. Phys. Conf. Ser.* **1162** (2019) 012012, [1808.09281].

[51] CMS collaboration, *The Phase-2 Upgrade of the CMS Endcap Calorimeter*, .

[52] CALICE collaboration, N. Tsuji, L. Liu, T. Torimaru, T. Mori and W. Ootani, *Study on Granularity Optimization for ILD Hadron Calorimeter*, *JPS Conf. Proc.* **27** (2019) 012015.

[53] Z. Yuan, K. Briggl, H. Chen, Y. Munwes, H.-C. Schultz-Coulon and W. Shen, *KLauS: A Low-power SiPM Readout ASIC for Highly Granular Calorimeters*, in *2019 IEEE Nuclear Science Symposium (NSS) and Medical Imaging Conference (MIC)*, pp. 1–4, 2019, DOI.

[54] A. Balla et al., *Performance of scintillating tiles with direct silicon-photomultiplier (SiPM) readout for application to large area detectors*, 2109.08454.

[55] L. J. Nevay et al., *BDSIM: An accelerator tracking code with particle–matter interactions*, *Comput. Phys. Commun.* **252** (2020) 107200, [1808.10745].

[56] GEANT4 collaboration, S. Agostinelli et al., *GEANT4–a simulation toolkit*, *Nucl. Instrum. Meth. A* **506** (2003) 250–303.

[57] J. Allison et al., *Geant4 developments and applications*, *IEEE Trans. Nucl. Sci.* **53** (2006) 270.

[58] J. Allison et al., *Recent developments in Geant4*, *Nucl. Instrum. Meth. A* **835** (2016) 186–225.

[59] C. Lourenco and H. K. Wohri, *Heavy flavour hadro-production from fixed-target to collider*

energies, *Phys. Rept.* **433** (2006) 127–180, [hep-ph/0609101].

[60] SHiP collaboration, H. Dijkstra and T. Ruf, *Heavy Flavour Cascade Production in a Beam Dump,*, tech. rep., CERN, Geneva.

[61] E791 collaboration, E. M. Aitala et al., *Total forward and differential cross-sections of neutral D mesons produced in 500-GeV/c pi- nucleon interactions*, *Phys. Lett. B* **462** (1999) 225–236, [hep-ex/9906034].

[62] S. Ghinescu, B. Döbrich, E. Minucci and T. Spadaro, *A biased MC for muon production for beam-dump experiments*, *Eur. Phys. J. C* **81** (2021) 767, [2106.01932].

[63] D. Banerjee et al., *The North Experimental Area at the Cern Super Proton Synchrotron*, tech. rep., CERN, Geneva, July, 2021.

[64] M. Rosenthal et al., *Single-muon rate reduction for beam dump operation of the K12 beam line at CERN*, *Int. J. Mod. Phys. A* **34** (2019) 1942026.

[65] M. W. Winkler, *Decay and detection of a light scalar boson mixing with the Higgs boson*, *Phys. Rev. D* **99** (2019) 015018, [1809.01876].

[66] CHARM collaboration, F. Bergsma et al., *Search for Axion Like Particle Production in 400-{GeV} Proton - Copper Interactions*, *Phys. Lett. B* **157** (1985) 458–462.

[67] NA62 collaboration, E. Cortina Gil et al., *Search for a feebly interacting particle X in the decay $K^+ \to \pi^+ X$*, 2011.11329.

[68] E949 collaboration, A. Artamonov et al., *New measurement of the $K^+ \to \pi^+ \nu\bar{\nu}$ branching ratio*, *Phys. Rev. Lett.* **101** (2008) 191802, [0808.2459].

[69] P. B. Dev, R. N. Mohapatra and Y. Zhang, *Constraints on long-lived light scalars with flavor-changing couplings and the KOTO anomaly*, *Phys. Rev. D* **101** (2020) 075014, [1911.12334].

[70]

[71] D. Egana-Ugrinovic, S. Homiller and P. Meade, *Light Scalars and the Koto Anomaly*, *Phys. Rev. Lett.* **124** (2020) 191801, [1911.10203].

[72] LHCb collaboration, R. Aaij et al., *Search for long-lived scalar particles in $B^+ \to K^+ \chi(\mu^+\mu^-)$ decays*, *Phys. Rev. D* **95** (2017) 071101, [1612.07818].

[73] LHCb collaboration, R. Aaij et al., *Search for hidden-sector bosons in $B^0 \to K^{*0}\mu^+\mu^-$ decays*, *Phys. Rev. Lett.* **115** (2015) 161802, [1508.04094].

[74] Belle collaboration, J.-T. Wei et al., *Measurement of the Differential Branching Fraction and Forward-Backword Asymmetry for $B \to K^{(*)}\ell^+\ell^-$*, *Phys. Rev. Lett.* **103** (2009) 171801, [0904.0770].

[75] "Addendum i to p326 continuation of the physics programme of the na62 experiment."

[76] B. Batell, J. A. Evans, S. Gori and M. Rai, *Dark Scalars and Heavy Neutral Leptons at DarkQuest*, 2008.08108.

[77] A. Filimonova, R. Schäfer and S. Westhoff, *Probing dark sectors with long-lived particles at BELLE II*, *Phys. Rev. D* **101** (2020) 095006, [1911.03490].

[78] FASER collaboration, A. Ariga et al., *FASER's physics reach for long-lived particles*, *Phys. Rev. D* **99** (2019) 095011, [1811.12522].

[79] G. Aielli et al., *Expression of interest for the CODEX-b detector*, *Eur. Phys. J. C* **80**

(2020) 1177, [1911.00481].

[80] MATHUSLA collaboration, C. Alpigiani et al., *An Update to the Letter of Intent for MATHUSLA: Search for Long-Lived Particles at the HL-LHC*, 2009.01693.

[81] A. Fradette and M. Pospelov, *BBN for the LHC: constraints on lifetimes of the Higgs portal scalars*, *Phys. Rev.* **D96** (2017) 075033, [1706.01920].

[82] P. S. B. Dev, R. N. Mohapatra and Y. Zhang, *Revisiting supernova constraints on a light CP-even scalar*, *JCAP* **08** (2020) 003, [2005.00490].

[83] G. Bernardi et al., *FURTHER LIMITS ON HEAVY NEUTRINO COUPLINGS*, *Phys. Lett. B* **203** (1988) 332–334.

[84] PIENU collaboration, A. Aguilar-Arevalo et al., *Improved search for heavy neutrinos in the decay $\pi \to e\nu$*, *Phys. Rev. D* **97** (2018) 072012, [1712.03275].

[85] NA62 collaboration, E. Cortina Gil et al., *Search for heavy neutral lepton production in K^+ decays to positrons*, *Phys. Lett. B* **807** (2020) 135599, [2005.09575].

[86] NA62 collaboration, E. Cortina Gil et al., *Search for K^+ decays to a muon and invisible particles*, 2101.12304.

[87] T2K collaboration, K. Abe et al., *Search for heavy neutrinos with the T2K near detector ND280*, *Phys. Rev. D* **100** (2019) 052006, [1902.07598].

[88] Belle collaboration, D. Liventsev et al., *Search for heavy neutrinos at Belle*, *Phys. Rev. D* **87** (2013) 071102, [1301.1105].

[89] DELPHI collaboration, P. Abreu et al., *Search for neutral heavy leptons produced in Z decays*, *Z. Phys. C* **74** (1997) 57–71.

[90] ATLAS collaboration, *Search for heavy neutral leptons in decays of W bosons produced in 13 TeV pp collisions using prompt and displaced signatures with the ATLAS detector*, *JHEP* **10** (2019) 265, [1905.09787].

[91] CMS collaboration, *Search for heavy neutral leptons in events with three charged leptons in proton-proton collisions at $\sqrt{s} = 13$ TeV*, *Phys. Rev. Lett.* **120** (2018) 221801, [1802.02965].

[92] C. Dib, J. Helo, M. Nayak, N. Neill, A. Soffer and J. Zamora-Saa, *Searching for a sterile neutrino that mixes predominantly with ν_τ at B factories*, *Phys. Rev. D* **101** (2020) 093003, [1908.09719].

[93] P. Ballett, T. Boschi and S. Pascoli, *Heavy Neutral Leptons from low-scale seesaws at the DUNE Near Detector*, *JHEP* **03** (2020) 111, [1905.00284].

[94] N. Sabti, A. Magalich and A. Filimonova, *An Extended Analysis of Heavy Neutral Leptons during Big Bang Nucleosynthesis*, *JCAP* **11** (2020) 056, [2006.07387].

[95] B. Döbrich, F. Ertas, F. Kahlhoefer and T. Spadaro, *Model-independent bounds on light pseudoscalars from rare B-meson decays*, *Phys. Lett. B* **790** (2019) 537–544, [1810.11336].

[96] M. J. Dolan, F. Kahlhoefer, C. McCabe and K. Schmidt-Hoberg, *A taste of dark matter: Flavour constraints on pseudoscalar mediators*, *JHEP* **03** (2015) 171, [1412.5174].

[97] F. Ertas and F. Kahlhoefer, *On the interplay between astrophysical and laboratory probes of MeV-scale axion-like particles*, *JHEP* **07** (2020) 050, [2004.01193].

[98] K. J. Kelly, S. Kumar and Z. Liu, *Heavy axion opportunities at the DUNE near detector*, *Phys. Rev. D* **103** (2021) 095002, [2011.05995].

[99] J. Jerhot, B. Döbrich, F. Ertas, F. Kahlhoefer and T. Spadaro, *ALPINIST: Axion-Like Particles In Numerous Interactions Simulated and Tabulated*, *JHEP* **07** (2022) 094, [2201.05170].

[100] SND@LHC collaboration, C. Ahdida et al., *SND@LHC - Scattering and Neutrino Detector at the LHC*, tech. rep., CERN, Geneva, 2021.

[101] DONUT collaboration, K. Kodama et al., *Observation of tau neutrino interactions*, *Phys. Lett. B* **504** (2001) 218–224, [hep-ex/0012035].

[102] OPERA collaboration, N. Agafonova et al., *Observation of a first ν_τ candidate in the OPERA experiment in the CNGS beam*, *Phys. Lett. B* **691** (2010) 138–145, [1006.1623].

[103] Particle Data Group collaboration, R. L. Workman and Others, *Review of Particle Physics*, *PTEP* **2022** (2022) 083C01.

[104] S. Alekhin et al., *A facility to Search for Hidden Particles at the CERN SPS: the SHiP physics case*, *Rept. Prog. Phys.* **79** (2016) 124201, [1504.04855].

[105] SHiP collaboration, C. Ahdida et al., *SHiP Experiment - Progress Report*, tech. rep., CERN, Geneva, 2019.

[106] W. Bai and M. H. Reno, *Prompt neutrinos and intrinsic charm at SHiP*, *JHEP* **02** (2019) 077, [1807.02746].

[107] F. Neuhaus, M. Schott and R. Wanke, *NaNu: Proposal for a Neutrino Experiment at the SPS Collider located at the North Area of CERN*, 2210.15532.

[108] FASER collaboration, H. Abreu et al., *Detecting and Studying High-Energy Collider Neutrinos with FASER at the LHC*, *Eur. Phys. J. C* **80** (2020) 61, [1908.02310].

[109] B. Brickwedde, A. Düdder, M. Schott and E. Yildirim, *Design, Construction and Performance Tests of a Prototype MicroMegas Chamber with Two Readout Planes in a Common Gas Volume*, *Nucl. Instrum. Meth. A* **864** (2017) 1–6, [1610.09539].

[110] C. Bierlich et al., *A comprehensive guide to the physics and usage of PYTHIA 8.3*, 2203.11601.

[111] C. Andreopoulos et al., *The GENIE Neutrino Monte Carlo Generator*, *Nucl. Instrum. Meth. A* **614** (2010) 87–104, [0905.2517].

[112] DONUT collaboration, R. Schwienhorst et al., *A New upper limit for the tau - neutrino magnetic moment*, *Phys. Lett. B* **513** (2001) 23–29, [hep-ex/0102026].